Decoupling DNA Twist and Stretch: Development and Application of a Magneto-Optical Tweezers Fluorescence Microscope

Sébastien Guilbaud

Doctor of Philosophy

University of York

Physics

January 2022

I Abstract

DNA is a complex biopolymer, support for the genetic information of most living organisms on Earth. Beyond this passive role of information carrier, its physical properties such as its topology or elasticity are now known to be critical to the function of living systems. The development of highly precise quantitative methods to probe these properties one molecule at a time can offer an invaluable insight into the complex multidimensional response of DNA to various physicochemical stimuli, shedding light on their causes and consequences.

This works presents the development of a unique device to carry out those measurement, unique in the combination of robust techniques proven to be highly relevant during the last three decades of experimental single-molecule biophysics. We show an ability to observe DNA molecules by detecting fluorescent molecules bound to it, directly detecting structures such as DNA braids for the first time for long periods of up to a minute. The ability to decouple DNA torque and tension in this configuration is also achieved, showing that the fusion of those three technologies (magnetic tweezing, optical trapping and fluorescence imaging) can be achieved without significant drawbacks.

II Table of Contents

I Abstract 2
II Table of Contents 3
IV Lists of Figures and Tables 5
IV.1 List of figures 5
IV.2 List of Tables 7
V Acknowledgements 8
VI Author's Declaration 9
VII Introduction 10
VII.1 DNA 10
VII.1.i The Central Dogma of Molecular Biology 10
VII.1.ii Biochemical Properties 11
VII.1.iii DNA Supercoiling 14
VII.2 Quantitative Polymer Models of DNA 15
VII.2.i A Discrete Model: The Freely-jointed Chain 16
VII.2.ii Going continuous: the Worm-like Chain Model 18
VII.2.iii Modeling of DNA Supercoiling 24
VII.2.iv Molecular Dynamics simulations 26
VII.3 Single-Molecule Techniques to study DNA 27
VII.3.i Single-molecule vs. Ensemble Average Techniques 28
VII.3.ii Single-molecule Fluorescence Microscopy 29
VII.3.iii Single-molecule DNA Tension Transduction 37
VII.3.iv Single-molecule Torque Production 42
VII.3.v Best of both worlds: Magneto-Optical Tweezers 43
VIII Experimental Techniques 45
VIII.1 General Experimental Considerations and Data Acquisition 45
VIII.1.i General Experiment Configuration 45
VIII.1.ii Tethering Experiment Protocol 46
VIII.2 Optical Trapping 49
VIII.1.i Fundamentals 49
VIII.1.ii Construction of an Optical Trap 51
VIII.1.iii Measuring Forces with an Optical Trap 53
VIII.3 Magnetic Tweezing 60
VIII.2.i Fundamentals 60

VIII.2.ii Characterization and Control of MT-induced Stage Drift 63
VIII.2.iii MT Performance and Influence of the OT on Bead Rotation 64
VIII.4 DNA Tether Synthesis 67
VIII.5 Fluorescence microscopy and choice of DNA-binding dye 69
VIII.5.i Fluorescence microscopy 70
VIII.5.ii Choice of dye 70
IX. Technical Development 72
IX.1 Microscope Design 73
IX.1.i Hardware 73
IX.1.ii Labview Control Software 77
IX.2 Surface and Bead Chemistry 78
IX.2.i Surface Chemistry 79
IX.2.ii Bead-protein Conjugation Chemistry 81
IX.4 Microfluidics 83
IX.4.i Flow cell designs 83
IX.4.ii Optical trapping under flow 85
X. Pulling on & Twisting single DNA molecules 87
X.1 Influence of DNA Intercalators on the Mechanical Properties of DNA 87
X.2 Twisting DNA 91
X.2.i Supercoiling one DNA Tether 91
X.2.ii Possible explanations and mitigation attempts 93
XI Discussion 96
XI.1 Results Discussion 96
XI.2 Comments on the setup performance and shortcomings 97
XI.3 Possible technical improvements 98
XI.3.i Solution 1: Replacing the anchor beads 98
XI.3.ii Solution 2: Complete setup redesign 99
XI.4 Future work 103
XI.4 Conclusion 104
XII Appendix 105
XII.1 Protocols 105
XII.1.i Protein functionalization of carboxylated beads 105
XII.1.ii Glass coverslip cleaning and silanization 105
XII.2 Code 106
XII.2.i Force-extension processing and analysis code (Matlab) 106
XIII Bibliography 110

IV Lists of Figures and Tables

IV.1 List of figures

Figure 1: Schematic of the Central Dogma of Molecular Biology. 11
Figure 2: Chemical structure of double-stranded DNA. 12
Figure 3: Cartoon modelling replication in a bacterial chromosome. 14
Figure 4: Representation of a polymer using the Freely-Jointed Chain model 16
Figure 5: Representation of a polymer using the Worm-Like-Chain model. 18
Figure 6: Simulated force-extension curves of several nucleic acid polymers at 298 K 22
Figure 7: Extension-force behaviour of a 48.5 kbp DNA molecule from λ-bacteriophage at increasing concentration of fluorescent intercalator YO-PRO. 23
Figure 8: Extension of a XX kbp DNA tether as a function of positive and negative supercoiling, at a constant force indicated. 25
Figure 9: Equation from the so-called Marko model, quantifying the free energy of a buckled supercoiled DNA. 25
Figure 10: Graphical representation of the OxDNA model, approximating the DNA backbone as a single atom, and nucleic bases as another. 27
Figure 11: Cartoon of a DNA hairpin. 28
Figure 12: General Jablonski diagram of the various processes involved during a radiative excitation-deexcitation cycle. 30
Figure 13: Fluorescence excitation decay recorded during a TCSPC experiment. 31
Figure 14: Graphs of the Excitation and emission spectra of two fluorescent dyes: SYBR Gold and Alexa Fluor 647. 32
Figure 15: Comparison of the same human cell imaged through normal confocal microscopy (left) and STED super-resolution microscopy on the right.. 35
Figure 16: Simplified diagram of a basic fluorescence microscope. 36
Figure 17:Cartoon of TIRF illumination. 37
Figure 18: Fluorescence images of an overstretched DNA dumbbell, in two colour channels, then combined. . 38
Figure 19: Fluorescence microscopy images of a DNA curtains assay 40
Figure 20: Cartoon of the magneto-optical tweezers experiment configuration. 46
Figure 21: Example of a QPD signal-bead displacement fitted to produce a calibration curve. 47
Figure 22: Schematic of the Optical Tweezers layout. 49
Figure 23: Force diagram of the optical trap-induced forces experienced by a bead at several points relative to the trap centre. 50
Figure 24: Image of the back-reflexion of the optical trap on the sample coverslip. 52
Figure 25: Example graph of the signal from an immobile 2 µm trapped bead in Fourier space 56
Figure 26: Graph of the normalized detected signal from the QPD when scanning the optical trap across a surface immobilized 1 µm bead, with the system calibrated for proper BFP detection. 57
Figure 27: Optical schematic of the QPD force spectroscopy system. 58
Figure 28: Graphs of the data used to calibrate the QPD response for every bead. 59
Figure 29: Model of an ideal Helmholtz coil. 61
Figure 30: Modelization of the spatial distribution of the magnetic field produced by each Helmoltz coil pair from two angles. 62
Figure 31: 2-dimensional chart of the position of a surface-immobilised anchor bead when the magnetic tweezers are turned on, for 25 minutes. 63
Figure 32: Graph of the measured temperature of the Helmholtz coils over time 64
Figure 33: QPD signal of a spinning bead at 2Hz. 65

Figure 34: Graph in Fourier space of the signal resulting from the same bead spinning 66
Figure 35: Graph in Fourier space of the signal from the same spinning bead, at 20 Hz in red and 50 Hz in blue. 67
Figure 36: Chemical structures of Biotin on the left and Digoxigenin on the right 68
Figure 37: Map of some of the restriction sites present on the lamb template, with the two relevant ones underlined in green. 68
Figure 38: Gel electrophoresis image of the result of a handle production test run. 69
Figure 39: Molecular structure of SYBR Gold, as determined by Lipfert et. al. [115]. 71
Figure 40: Comparison of the assay performance before and after this project.. 72
Figure 41:F To-scale schematic of the final microscope optical layout. 73
Figure 42: Optical schematics of the beam delivery setups, before (a) and after (b) modification.. 74
Figure 43: Schematic of the Imaging part of the optical setup. 75
Figure 44: a) Graph of the measured deflection of the fluorescence excitation beam as a function of the TIRF lens micrometer mount position. b) Box plots of the relative background-corrected integrated intensities of 80 nm fluorescent beads attached on the sample surface, in epifluorescence and TIRF illumination modes. 77
Figure 45: Front panel of the Labview program controlling the microscope. 78
Figure 46: Silanization reaction 80
Figure 47: Pictures taken from the sample surface, 10 frames after illumination. 80
Figure 48: Contact angle measurement of the surface of the same coverslip, untreated, cleaned then silanized. 81
Figure 49: Integrated intensity measured from a surface attached anchor bead over time, in presence of 1 µM SYBR Gold and PBS, with a total laser power of 150 µW. 82
Figure 50: Chemical reactions leading to Bead-Protein covalent coupling 82
Figure 51: Equally scaled images and line profiles of Micromod (dark on top) and Spherotech (bright on the bottom) anchor beads 83
Figure 52: Schematic of the sample's immediate surroundings, view from the front. Sample holder not shown. 84
Figure 53: Picture of the assembled flow cell, with the outlet tube disconnected. 85
Figure 54: Line graph of the observed displacement of a 3 µm trapped bead with increasing flow rates 86
Figure 55: Example graphs of two force-extension curves of DNA in PBS. 87
Figure 56: Example of fitted force-extension data obtained on DNA tethers in presence of 1 µM of SYBR Gold without any fluorescent excitation. 89
Figure 57: The impact of SYBR Gold binding on DNA's tensile properties. 90
Figure 58: On the left, two fluorescence images of the tether under maximum, then minimal extension. On the right, corresponding fitted force-extension data. 91
Figure 59: Pictures showing a braided "double" tether, where the DNA molecules have been spun around each other, appearing as one brighter tether. 92
Figure 60: Picture of a possible DNA plectoneme 93
Figure 61: Fluorescence image of a braided "double tether" 94
Figure 62: Reaction schematic of the one-pot production of a Lambda DNA tether. 97
Figure 63: Cartoon of a possible DNA curtains-like assay. 99
Figure 64: Cartoon of a possible further development of the microfluidic system. 101
Figure 65: a) Image of a HT-TPM sample (darkfield illumination) elaborated during a previous project. Each bright dot is a 300 nm AntiDig-functionnalized polystyrene bead tethered to the surface by a single DNA molecule. Up to 1000 valid complexes can be tracked simultaneously, limited only by the camera field of view. b) Cartoon of a HT-TPM assay, showing the Neutravidin micropatterning in orange. This allows a precise control over the density of tethered beads, ensuring that they are far enough from each other to avoid interfering. This technology can be applied to magnetic tweezers-type equipment to increase their throughput significantly. c) a type of experiment achievable by applying Magnetic tweezing to HTTPM. The DNA tether can be supercoiled by the two pairs of coils parallel to the sample, and possible plectonemic DNA ligands binding could be detected. 103

IV.2 List of Tables

Table 1: Parameters of different isoforms of double-stranded DNA 13

V Acknowledgements

I would like to first thank my supervisors, Agnes and Mark for their constant support and positive encouragement during those four years, in the hard times as well as the good times. They provided me with an exceptional environment to grow as a scientist as well as a person that I will always be thankful for. “Caring” is I think the right word for my perception of the way that I was and am still being consistently treated at York, a model for many to follow.

This work would have never been possible without the help provided by the postdocs and lecturers within the Physics of Life group, especially Jack S, Jack Z, Sam, Alex and Steve who essentially taught me all of what I know in terms of microscope design and construction. Jamie was also the most patient teacher in the dark arts of molecular biology and was of invaluable help in this project. Those seasoned researchers who were one day in my shoes were incredibly kind and supportive especially during the hardest times and kept me productive and engaged with my work until the end. I hope to one day be as helpful to others as you were to me.

I am still utterly surprised by the absolute lack of any negative interaction with anybody at the University, as it seems that by some incredibly unlikely chance, every single one of them is a great human who has been a pleasure to get to know. I am grateful for the many friends I have made during those incredible four years, enjoying together many shared interests and hobbies. George, Victor, Nettie, Matteo, Matt, Elliot, Emma, Lara, Sarah, thanks for being hilarious people, I hope that you always stay weird, as working without your antics would have frankly been boring. I am glad that I will be able to remain near you for the foreseeable future.

Finally, I would like to dedicate this work to my partner Monica, who has been my rock during those trying times, I cannot imagine ever being able to do this without you. You kept me grounded and were ever supportive while making sure that I would always take care of myself.

My thanks to all of you.

VI Author's Declaration

I declare that this thesis is a presentation of original work and I am the sole author, except for the specific collaborations detailed below. This work has not previously been submitted for a degree at this or any other university. All sources are acknowledged as references.

- Part of the optical design was elaborated with the help of Dr. J. Shepherd and Dr. S. Yoshua.

- The design and construction of the Magnetic Tweezers was done by Dr. Zhou

- The design and synthesis of the DNA tether was done under the direction of Dr. Howard.

- The glass cleaning procedure was adapted from Dr Colas's work.

VII Introduction

This chapter will introduce the scientific context around which the project revolves. First, basic concepts of DNA biochemistry and molecular biology will be introduced, then DNA and its supercoiling will be described using polymer physics models. Finally, an overview will be made of several microscopy techniques to image and manipulate single molecules of DNA.

VII.1 DNA

VII.1.i The Central Dogma of Molecular Biology

DNA, short for Deoxyribonucleic acid, is a bio-polymer (a biomolecule composed of numerous connected monomeric sub-units) responsible for the transmission of genetic information in the living realm. This information is mostly encoded in the linear sequence of monomers called nucleotides and can be transcribed into a different linear sequence of amino-acids called a protein. This progressive conversion of genetic information starts at the DNA that is transcribed into a single-stranded RNA molecule by RNA polymerases, spliced by small nuclear riboproteins (snRPs) to become a messenger RNA (mRNA). mRNAs will then be translated into a protein after splicing by a highly conserved[1] RNA-based enzyme (ribozyme) called a ribosome. This pathway is what's behind the Central Dogma of Molecular Biology. The produced proteins provide a crucial and wide array of abilities to the cell, such as catalytic activity, structure, transport, signal transduction, DNA repair, and many more. Often perceived by the general public as the blueprint to a cell or organism, DNA is thus really the blueprint to some of the tools and structures available to a cell, some of which will always be expressed, and others only for specific roles or in response to environmental stimuli.

Cellular organisms called eukaryotes possess a dedicated intracellular compartment, the nucleus, that allows for the physical segregation of the DNA. In prokaryotic organisms, which do not possess a nucleus, the DNA is located within a region called the nucleoid. It is to be noted that the vast majority of prokaryotes store their genetic information within circular DNA molecules, which as a consequence do not possess free ends. While there is no physical barrier that separates it from the rest of the cell's cytosol, mechanisms still exist to dynamically organize it, depending on a variety of possible environmental conditions and other stimuli.

Those mechanisms exist thanks to the numerous interactions between DNA and certain proteins. We can distinguish two larger groups of DNA-interacting proteins:

- Proteins that bind to DNA in a stable fashion, locally altering its topology. An example commonly found in eukaryotes would be histone proteins[2], that act as a large spool for DNA to wrap around several times[3], forming chromatin fibres. Prokaryotes do not rely on histone-like proteins nearly as much and possess a wide array of more simple proteins called Nucleoid-Associated Proteins (NAPs) such as HU, H-NS or IHF, that allow for the organisation of bacterial DNA.

- Proteins that transiently bind to DNA and catalyse its isomerisation into a product with a different topology. Those enzymes are called topoisomerases and rely on a single or double strand break of the DNA molecule, a rotation then a resection into the same original molecule, but with a different amount of helical twists[4]. To relieve the stress added by this reaction, DNA will wrap around itself and form superstructures called plectonemes[5], the study of which will be central to the work described in this document. Some proteins will also transiently bind to effect local chemical changes on the DNA molecule, such as breaking[6] or forming chemical bonds or add new moieties to a specific nucleotide[7].

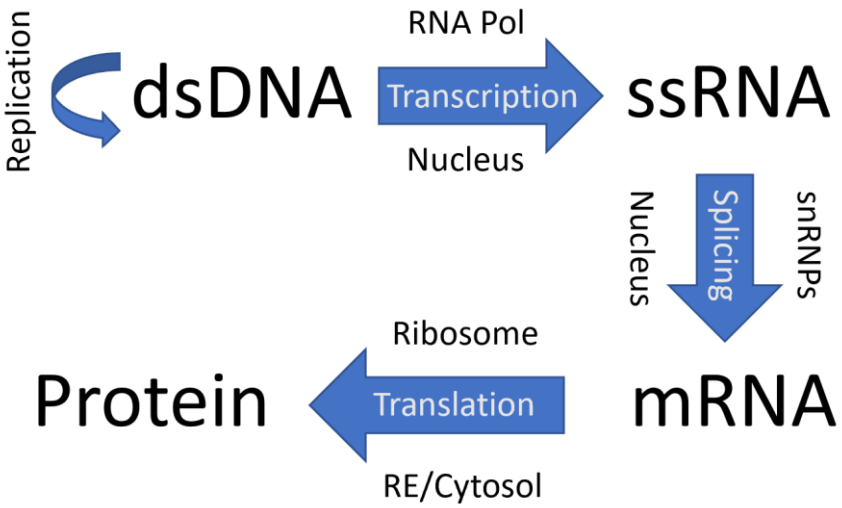

Figure 1: Schematic of the Central Dogma of Molecular Biology. The enzymatic agent class responsible for each process is mentioned above the process arrow, the location (in eukaryotes) is mentioned under it. In prokaryotes, all of those processes occur within the cell cytosol.

VII.1.ii Biochemical Properties

A single strand of DNA is a linear polymer of nucleotides, each nucleotide is formed of a phosphate coupled to a deoxyribose molecule attached to one of four possible nucleobases (Adenine, Thymine, Guanine, Cytosine). A nucleotide is bound to its two neighbours either through its Phosphate or through its ribose. This allows

for the polarization of a single DNA strand, one end being called 3'(phosphate), the other 5'(ribose), a sequence being traditionally read form its 5' to its 3' end. DNA is in this case said to be in its primary form. It should be noted that each phosphate moiety is found in physiological conditions to be negatively charged, and since the amount of DNA in a living cell can amount to up to hundreds of millions of base pairs[8], DNA is a considerably charged anion. Those negative charges repel each other, but this interactions can get screened by counter-ions, which results in a complex relationship between mechanical properties and chemical environment[9].

From its primary structure, a more complex secondary configuration can arise and give form to the famous DNA double helix, or dsDNA. In this state, two complementary single strands of DNA will wrap around each other in a process called hybridization (its opposite being called denaturation, or melting), into a form of DNA called B-DNA. This process is highly energetically favourable at biologically relevant temperatures and gets progressively unfavourable as the temperature rises (*ie* melting is promoted). This stabilising interaction relies entirely on non-covalent molecular interactions, and is thus highly sensitive to local ionic conditions[10]. Those interactions arise from two sources: the stacking of the pi orbitals localized around the nucleotides' aromatic rings, and the lateral hydrogen bonding between either Adenine and Thymine or Guanine and Cytosine. More complex modes of base-base hydrogen bonding modes called non-canonical base-pairing exist such as Hoogsteen pairs[11], and can involve more than two base pairings, but they do not typically arise in the context of DNA hybridization/melting in a stable fashion.

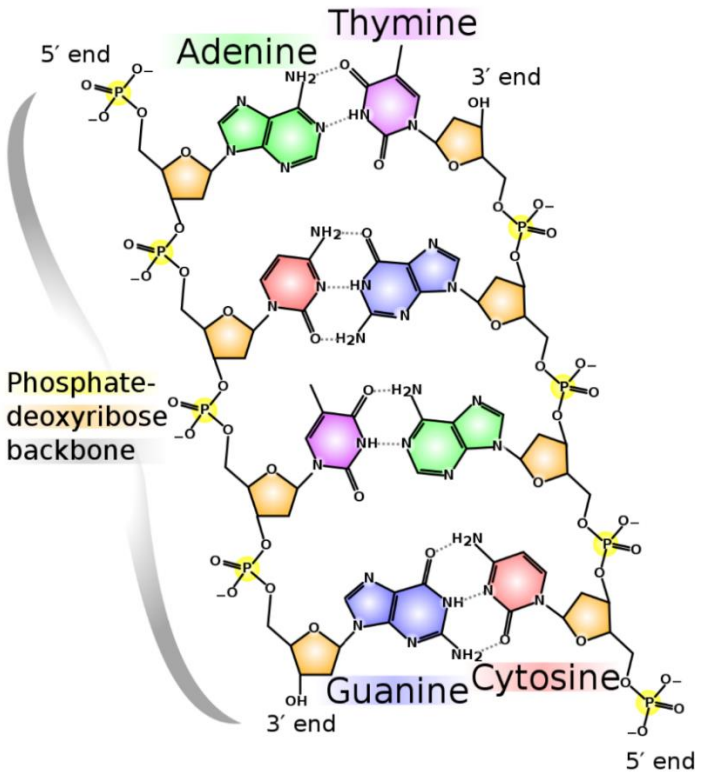

Figure 2: Chemical structure of double-stranded DNA. Covalent bonds are in solid lines, Hydrogen bonds in dashed lines. From Wikipedia.org, diagram by Madeleine Price Ball.

The double helix parameters reported below are only valid for dsDNA in normal physical, (temperature, tension, etc…), and chemical (pH, ionic strength, etc…) conditions. As DNA experiences perturbations, it can adopt vastly different forms, of which a few have been proven to be biologically compatible (A, B and Z-DNA). A-DNA is similar to B-DNA, but presents a higher helicity (less base pairs per turn) and loses the parallel stacking of the nucleic base pairs. This forms typically occurs when hydration levels are at their lowest[12], in desiccated bacteria for example as a global effect, or locally as a consequence of the binding of certain DNA-processing proteins[13]. Z-DNA is a more distinct isoform[14]. Indeed, it present a left-handed helicity, and minor and major grooves are much more alike than in any other form. Instead of a base pair, its monomeric unit is a pair of base pairs (2 bp)[15]. This isoform has been linked to transcription rate[16] and negative supercoiling[17] and has been suspected to play a role in various genetic diseases[18], which underlines the fact that genetic information is not solely encoded in the sequence of DNA.

Isoform	A-DNA	B-DNA	Z-DNA
Chirality	Right	Right	Left
Width (nm)	2.3	2	1.8
Helical pitch (nm/bp)	0.28	0.34	0.46
Base pairs per turn	11	10.5	12

Table 1: Parameters of different isoforms of double-stranded DNA

More DNA isoforms have been discovered, especially under considerable mechanical stress. Two examples would be P-DNA and L-DNA. P-DNA, named in honour of Linus Pauling's hypothesized structure of DNA, presents a radically different secondary structure compared to the previously mentioned ones. Indeed, when under significant tension and torque, the Hydrogen bonds between nucleic bases break down, and the molecule is flipped inside out, with its bases on the outside and its phosphate backbones are interwoven[19]. This form interestingly arises only in discrete local regions of a mechanically perturbed dsDNA molecule, with other regions preserving their B-form. There is currently no direct evidence of a biological role of P-DNA, but this peculiar behaviour might suggest that it contributes to increasing DNA stability by concentrating mechanical stress in regions where it would have less of an impact. The L-DNA isoform arises after a significant underwinding of the B-DNA double helix at moderate tension. It results in a melted isoform of DNA and is left-handed[20]. None of those two isoforms has been detected in vivo, but the extreme forces expressed by some DNA-processing molecular motors suggests that their occurrence in living systems is theoretically possible[21,22]. Those isoforms appearing under a range of significant physical constraints (torque and tension), it is difficult to give accurate values for parameters such as width, or helical pitch.

VII.1.iii DNA Supercoiling

DNA supercoiling occurs when there is a deviation from the canonical helicity value of 10.5 base pairs per turn. But in prokaryotes DNA is actually natively found in a negatively supercoiled state and can locally take a wide distribution of supercoiling states. This globally underwound configuration allows for an easier local denaturation by helicases that allows for the assembly of the replisome, the group of enzymes responsible for the copy of DNA during cell division. Additionally, the progression of this replisome will necessarily introduce positive supercoils ahead, and negative supercoils behind[23]. This will eventually introduce too much torsional stress on the template DNA and must be relaxed to continue replication[24]. In order to relax this stress, the DNA polymerase could in theory rotate around its DNA template, but its large size as well as the crowded intracellular environment impedes this[25]. Topoisomerase are then the only effective way to relieve unwanted DNA supercoiling.

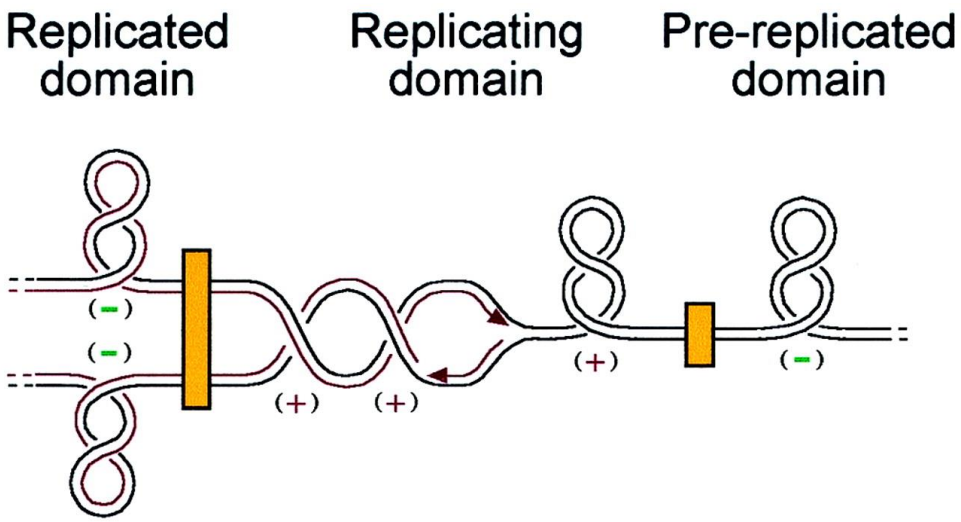

Figure 3: Cartoon modelling replicatio. Parent strands are drawn in black, replicated strand in red. The yellow rectangles symbolize so-called domain barriers, that isolate any topological change occurring in-between them from propagating further. On either side of them, the chromosome is kept in a generally undercoiled state. The replication fork occurs in between the barriers, increasing the supercoiling ahead of its progression, and producing braided pre-catenanes downstream of it. From Postow L et al., Topological challenges to DNA replication: conformations at the fork. PNAS 2001.

We previously described topoisomerases as a group of enzymes that change the number of helical turns in a DNA molecule by cutting, rotating then resecting it. Let us call this number Tw. In a relaxed unconstrained configuration,

$$T_{w0} = \frac{length\ in\ bp}{10.5\ bp/turn} \quad (1)$$

If we were to forcibly add or remove helical turns, the DNA molecule would relax this excess torsional stress by coiling around itself, forming structures called writhes, which is described by the parameter Wr. If the double strand forms two entire turns around itself, Wr=2 for example. We can then introduce a third descriptor called the Linking Number Lk, that connects the two previous in such a way:

$$L_K = T_W + W_R \quad (2)$$

Without breaking any DNA strand, it is physically impossible to change Lk, but Tw and Wr can still explore a range of values, positive and negative. The following expression will thus inform us on the amount of turns added or removed:

$$\Delta L_K = L_K - T_{W0} \quad (3)$$

The value of ΔL_K thus describes if a DNA molecule is positively or negatively supercoiled, and the parameter sigma, equivalent to a supercoiling density, is:

$$\sigma = \frac{\Delta L_K}{T_{W0}} \quad (4)$$

This parameter describes how much the level of supercoiling of a given DNA molecule differs from the expected value for a canonical un-constrained molecule. As a reference, the supercoiling density expected in a living bacteria is -0.05, meaning 5% underwound globally[26].

Supercoiling DNA does not only occur during replication. It also occurs during transcription, where the DNA is read and a mRNA molecule is produced. Supercoiling can also be used as a long range signalling mechanism, allowing for the modulation of the expression of certain genes[27] as well as of the binding of DNA-processing enzymes[28]. If controlled, a stable and predictable location of plectoneme formation allows cells to organize their genome[29]. Several environmental factors can also influence their formation: pH[30,31], ionic composition[32], tension[33] as well as sequence[34]. While the general behaviour of average supercoiled DNA is fairly well known[35,36], we are still missing a proper physical model that would generally predict the impact of DNA sequence on its local features under the entire range of possible supercoiled states.

VII.2 Quantitative Polymer Models of DNA

Long linear polymeric molecules such as DNA possess a remarkably large number of degrees of freedom. Accurately modeling their dynamics using atomistic models would thus

be incredibly costly, that is why the field of polymer physics typically uses tools and approaches from statistical physics. We will attempt to briefly describe a few simple popular models of DNA.

VII.2.i A Discrete Model: The Freely-jointed Chain

Let us model a linear molecule of dsDNA as a chain of N independently oriented links of fixed length a called Kuhn length, each link being free to rotate around its own axis only, as a model of a freely rotating molecular bond. The contour length L of the polymer is defined as the total end to end distance of the polymer if every link pointed in the same direction.

$$L=N.a \tag{5}$$

We can model each of the N links by a vector $\vec{t_i}$, where:

$$\vec{t_i} = \vec{r_i} - \overrightarrow{r_{i-1}} \tag{6}$$

Where $\vec{r_i}$ vectors are the position vector of every monomer. The end-to-end distance of the polymer is called $\vec{R}$.

$$\vec{R} = \overrightarrow{r_N} - \overrightarrow{r_0} = \sum_{i=1}^{N} \vec{t_i} \tag{7}$$

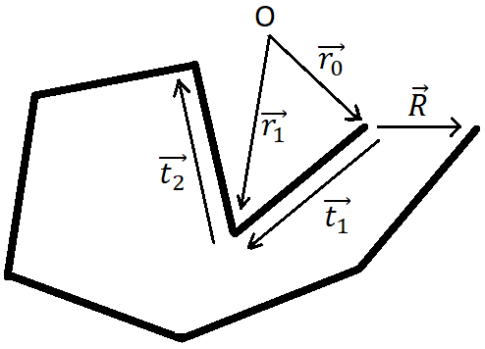

Figure 4: Representation of a polymer using the Freely-Jointed Chain model

A consequence of the lack of correlation between every link is that the average end-to-end distance $\langle \vec{R} \rangle$ is equal to $\vec{0}$, since

$$\langle \vec{R} \rangle = \sum_{i=1}^{N} \langle \vec{t_i} \rangle = \sum_{i=1}^{N} \vec{0}$$

(8)

The average end-to-end distance being always nil is not a useful quantity to use in this type of consideration, we will then introduce the mean squared end-to-end distance $\langle \vec{R}^2 \rangle$:

$$\langle \vec{R}^2 \rangle = \sum_{i=1}^{N} \sum_{j=1}^{N} \langle \vec{t_i} . \vec{t_j} \rangle = a^2 \sum_{i=1}^{N} \sum_{i=1}^{N} \langle cos\theta_{i,j} \rangle$$

(9)

The orientation of the segments being random, the average angle between two is nil. Thus,

$$\langle \vec{R}^2 \rangle = Na^2$$

(10)

The root mean square (RMS) end-to-end distance then equals:

$$\sqrt{\langle \vec{R}^2 \rangle} = \sqrt{N}a$$

(11)

Let us define the barycentre position vector $\overrightarrow{r_G}$ such that

$$\overrightarrow{r_G} = \frac{1}{(N+1)} \sum_{m=0}^{N} \overrightarrow{r_m}$$

(12)

We can introduce a new quantity called radius of gyration, that is related to the average distance of the monomers to the centre of mass of the coil. This parameter can be accessed through various experimental means such as Static Light Scattering and X-ray Diffraction techniques, and is equal to:

$$R_G^2 = \frac{1}{(N+1)} \sum_{i=0}^{N} \langle (\overrightarrow{r_i} - \overrightarrow{r_G})^2 \rangle$$

(13)

By developing this formula further, we can show that

$$R_g \approx \sqrt{\frac{N}{6}}\, l = \frac{\langle \vec{R}^2 \rangle}{6}$$

(14)

While the FJC model is useful to introduce useful concepts of polymer physics and functions reasonably well at low force regimes, it suffers from its simplistic approach. Indeed, DNA is able to bend, and thus modelling it using freely rotating joints might be misleading. We will then introduce a slightly more complex continuous model called the Worm-like-chain model.

VII.2.ii Going continuous: the Worm-like Chain Model

Instead of trying to model a polymer as a discrete sum of parts we can model it as a continuous bendable but not twistable rod of contour length L, with a bending stiffness κ. Let us look at two points on the polymer t and t', respectively located at s and s' along the polymer contour length. The average correlation between the tangent vectors $\vec{t}$ and $\vec{t'}$ agrees to the following:

$$\overrightarrow{t_{(s)}} = \frac{d\overrightarrow{r_{(s)}}}{ds}$$

(15)

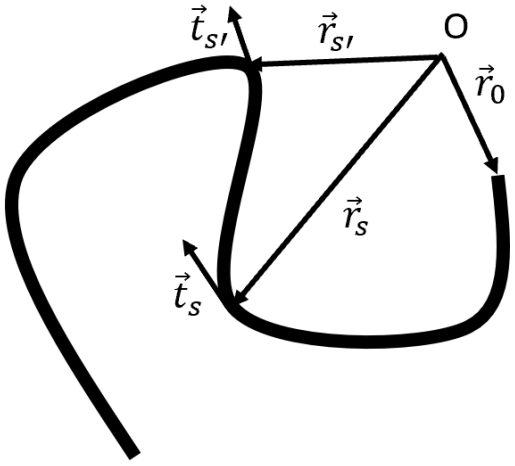

Figure 5: Representation of a polymer using the Worm-Like-Chain model.

The following section will attempt to show where from a parameter called persistence length Lp can be derived, which describes the ability of a linear polymer to be bent by thermal fluctuation. By modelling the polymer as a bending rod-like object, we can compute the work W needed to bend it by an angle θ as:

$$W(\theta) = \frac{\kappa\theta^2}{2s}$$

(16)

The probability of thermal fluctuation bending this polymer by θ can then be shown to be

$$P(\theta) = \frac{1}{Z}\int_0^{2\pi} d\varphi \sin(\theta) e^{\frac{-W(\theta)}{k_B T}}$$

(17)

With Z a normalization factor and φ the rotation angle around $\overrightarrow{t(0)}$. This leads to the following relationship:

$$\left\langle \overrightarrow{t(s)} \cdot \overrightarrow{t(s')} \right\rangle = \langle cos\,\theta \rangle = e^{\frac{-(s'-s)}{Lp}}$$

(18)

Where θ is the angle between $\overrightarrow{t(s)}$ and $\overrightarrow{t(s')}$, and Lp the persistence length of this polymer. Lp is indeed the characteristic length scale along which the correlation between two section of a polymer decays, which is correlated to its. Lp can be expressed as a function of the bending stiffness κ in the following way:

$$Lp = \frac{\kappa}{k_B \mathrm{T}}$$

(19)

It can thus be said that a section of a polymer the length of which is small compared to its persistence length (50 nm or 150 bp for dsDNA) can practically be considered straight while immersed in water at room temperature. From this, we can access the mean square end to end distance $\langle \vec{R}^2 \rangle$ since

$$\vec{R} = \int_0^L \overrightarrow{t_{(S)}}\, ds$$

(20)

$$\langle \vec{R}^2 \rangle = \int_0^L ds \int_0^L < \overrightarrow{t_{(s)}} \cdot \overrightarrow{t_{(s')}} > ds'$$

(21)

$$\left\langle \vec{R}^2 \right\rangle = \int_0^L ds \int_0^L e^{\frac{-(s'-s)}{Lp}} ds'$$

(22)

$$\left\langle \vec{R}^2 \right\rangle = 2L.Lp.[1 - \frac{Lp}{L}\left(1 - e^{-\frac{L}{Lp}}\right)]$$

(23)

When L>>Lp, we get

$$\left\langle \overrightarrow{R^2} \right\rangle \approx 2LL_P$$

(24)

Which is consistent with the FJC model result at low forces, where a Kuhn length a is equal to 2*Lp. The radius of gyration Rg can be obtained from the previous formula linking in to the RMS end-to-end such as:

$$R_g = \sqrt{\frac{\left\langle \vec{R}^2 \right\rangle}{6}} = \sqrt{\frac{LLp}{3}}$$

(25)

As a practical example: let's assume the *Escherichia coli* genome to be linear instead of circular. It contains 4.6Mbp. Using a standard Lp value of 50 nm, we find a radius of gyration of more than 5µm. This is considerably larger than a typical 2 by 0.5 µm *E.coli* bacteria. In reality, the nucleoid occupies roughly half of the cell volume[37] (0.2 μm^3), which shows the degree of compaction and organization that bacterial DNA typically undergoes.

Finally, the use of the WLC model can be convenient for analysing single-molecule experiments during which a piece of dsDNA is progressively stretched, and its response measured. There is currently no derived analytical solution, but reasonably accurate approximations of the behaviour of DNA have been published from interpolation of numerical approximations[38,39] , such as the following:

$$F = \frac{k_B T}{L_P}\left(\frac{1}{4}\left(1 - \frac{x}{L}\right)^{-2} - \frac{1}{4} + \frac{x}{L} - 0{,}8\left(\frac{x}{L}\right)^{2.15}\right)$$

(26)

Where k_B is the Boltzmann constant, F is the force, L is the contour length and x the extension. This formula can be adapted depending on the desired accuracy, the force regime (high, low) and has thus become a staple of single-molecule force

transduction experiments on linear polymers. At low extension (x << L) and low force (f < 5 pN), the terms with powers -2 and 2.15 become negligible and the equation approaches a classical Hookean behaviour:

$$F = -kx \tag{27}$$

With $k = \frac{k_B T}{L L_P}$ being the apparent spring constant of DNA. It is important to note the position of the $k_B T$ factor here, because of which a somewhat unintuitive behaviour arises. Indeed, the higher the temperature, the higher the force necessary to lengthen a WLC polymer. In other words, the higher the temperature, the more compact of a coil DNA will try to make. This is at the origin of the term "entropic spring" used to describe DNA's coiling behaviour. This is due to the fact that while the entropy of the polymer itself would be lowered by coiling, which would be counter to the Second Law of Thermodynamics, the overall entropy of the system, which includes all water molecules around it will be maximized. This fact underlines the importance of the aqueous solvent when describing statistical mechanics of a polymer and supports the idea that mechanical studies of DNA should be carried out in a medium that resembles its native environment as much as possible in order to be relevant to biological systems. To witness this fact, one can suspend a weight using an elastic band, heat up the band using a blowdryer and verify that the tension increases, raising the height of the weight. Also, by measuring the temperature of another elastic band, one can verify that after a rapid extension, the temperature of the band will suddenly increase, and decrease during a sudden relaxation.

Moreover, one should be careful to not solely equate persistence length and flexibility but should rather see it as its resistance to extension, or tendency to coil. As we've seen above, the spring constant of DNA is inversely proportional to its persistence length. This means that a ssDNA molecule, which typically exhibits persistence lengths around 1-2 nm[40], will require a considerably higher force to uncoil than a dsDNA molecule with a 40 to 50 nm persistence length.

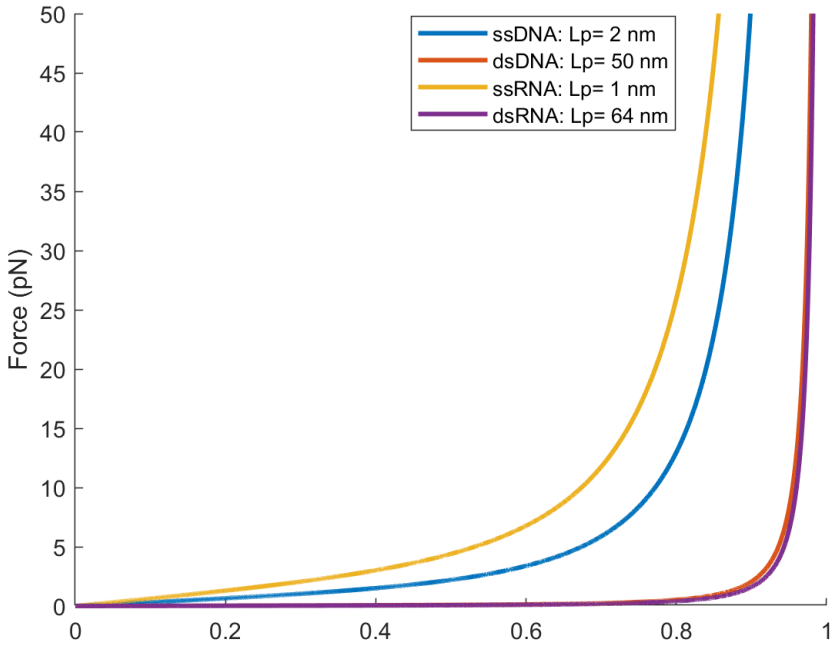

Figure 6: Simulated force-extension curves of several nucleic acid polymers at 298 K

The Force-extension behaviour model introduced above is only valid for extension values at low forces (under 50 pN). While the contour length of a relaxed DNA molecule is 0.34 nm, the theoretical maximum extension allowed by the DNA backbone is 0.7 nm. At higher force regimes, above 65 pN for example for a lambda DNA molecule, the force response of DNA changes as the contour length suddenly increases, from 0.34 to 0.58 nm/bp. This is called overstretching regime, a consequence of the drastic change in morphology of DNA, from the classical B-form to a more complex state containing a range of isoforms. Those isoforms can simply be denatured unpaired DNA (melting bubbles), or more exotic forms like P-DNA. It should be noted that the overstretching response of DNA is localized, with regions of entirely denatured DNA neighbouring regions of duplex DNA[41]. As mentioned earlier, the intercalative binding of fluorescent dyes will significantly disrupt the properties of DNA, increasing the length of each base pair they are bound to to 0.65 nm. As a consequence, experimentalists must take great care into accounting for those effects when measuring the mechanical properties of DNA in presence of intercalating agents.

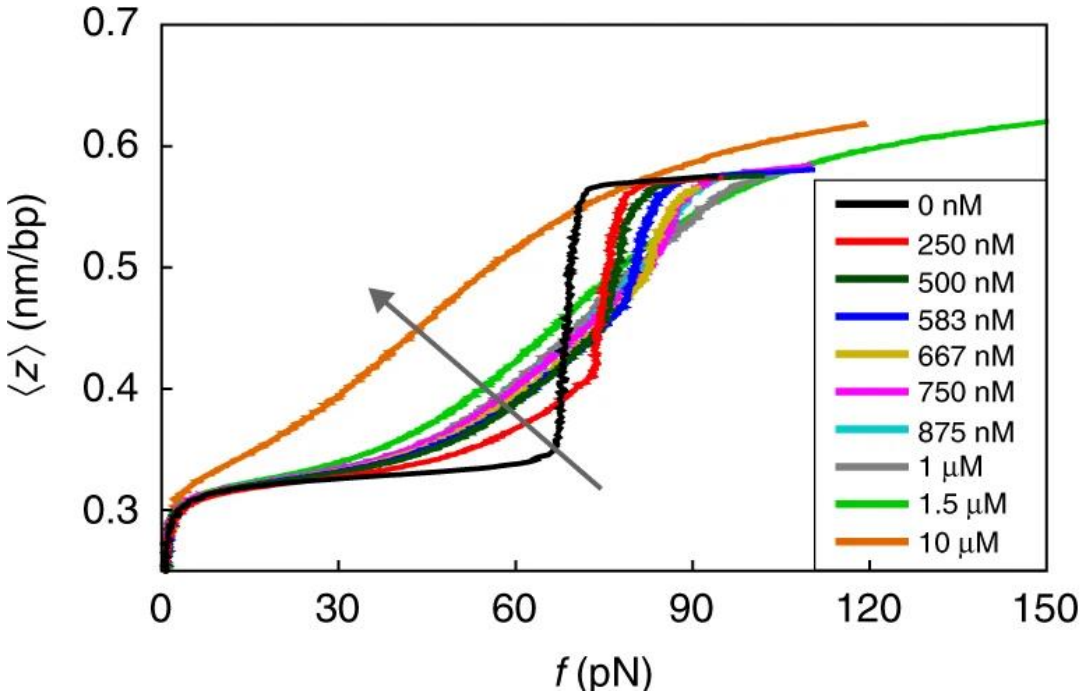

Figure 7: Extension-force behaviour of a 48.5 kbp DNA molecule from λ-bacteriophage at increasing concentration of fluorescent intercalator YO-PRO. The overstretching regime appears at forces over 60 pN, resulting in a doubling of the base pair length from the canonical 0.34 nm value. From Van Der Schoot et al., Hyperstretching DNA. Nature communications. 2017

The WLC model, while phenomenologically more accurate than the FJC, still makes simplistic and unrealistic assumptions. Indeed, while it has been used to accurately describe the behaviour of DNA, it does not perform well without adjustments at long[42,43] and short[44] (relative to the persistence length) contour length scales. There are multiple reasons for these shortcomings: there is still no account of DNA sequence, which can strongly effect the local properties of DNA and is increasingly important as the contour length decreases. In both models, the polymer does not interact with itself, meaning that two sections can cross each other. This becomes a problem at larger length scales, where excluded volume effects become more important.

Furthermore, as mentioned previously, the high negative charge density on DNA introduces repelling forces along the molecule, which stiffen the chain. As electrolytes approach the polymer and partially negate those interactions, complex nonlinear behaviours emerge that depend on both the concentration of charged molecules and their nature (valence, metallic or organic, etc…)[45]. The intracellular environment being known to vary considerably across time[46], there is a need for the accurate description of DNA dynamics beyond the most standard of experimental conditions. The simplest way to account for this is to introduce a dependence to Ionic strength in Lp, but this requires a careful theoretical approach and the use of more complex models taking electrostatics into account.

Various adjustments have been made upon the FJC and WLC to improve their accuracies[47,48], but the lack of a broadly applicable model that accounts for DNA supercoiling and its sequence remains, which could be critical for the quantitative understanding of many basic intracellular processes.

VII.2.iii Modeling of DNA Supercoiling

The behaviour of DNA in response to a change in its linking number follows two regimes. A small amount of supercoiling can be absorbed by the molecule without any drastic change in its configuration. The DNA tension rises with supercoiling until a critical value where it suddenly cannot compensate by shifting its helicity. Beyond this point, a sudden increase in tension is observed, called buckling transition[49], which leads to the relaxation of this torsional stress by the molecule by forming plectonemes. The length of the first regime (in terms of added supercoiling density) is highly dependent on the tension applied, the higher the tension, the more supercoiling density it takes to induce buckling. At a constant force, the post-buckling transition supercoiling-extension behaviour has been found to be broadly linear in numerous angular optical trap and magnetic tweezers-based publications [50,51]. At low force, the supercoiling-extension response is broadly symmetrical, between positive and negative supercoiling. But as tension increases past a critical value of 0.5 to 0.7 pN, an interesting behaviour arises, consequence of the chiral helical nature of DNA. Indeed, when undertwisting DNA, the molecule unwinds to absorb this mechanical stress, leading to no reduction of end-to-end distance. This behaviour is typically used to verify if a magnetically or optically trapped bead is attached to a single or several DNA tethers[52], a negative supercoiling-induced reduction in end-to-end distance at high tension being caused by the multiple DNA tethers being braided around each other. Even at a high constant force (typical of magnetic tweezers so around 5-7 pN), positive supercoiling will quickly collapse DNA to 10% or less of its contour length, before σ even approaches 0.25. On the other hand, a much larger amplitude of negative supercoiling is needed to result in the same contraction, past the critical tension value of 0.7 pN[53].

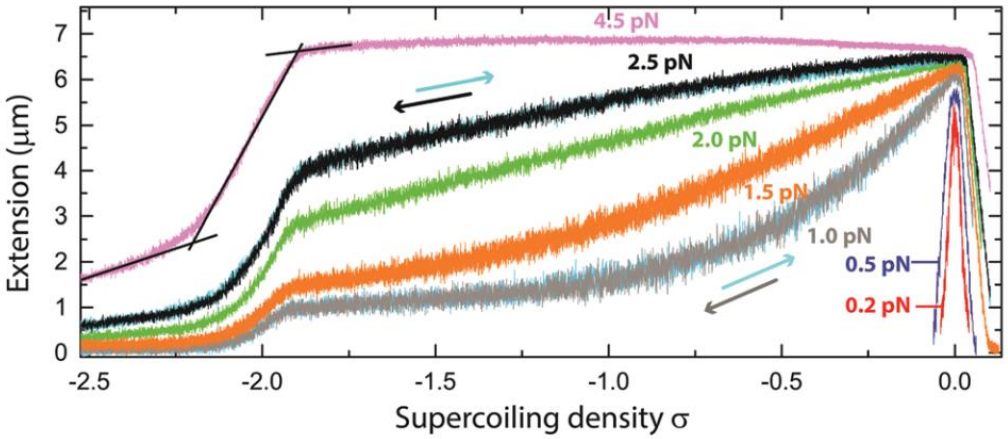

Figure 8: Extension of a DNA tether as a function of positive and negative supercoiling, at a constant force indicated. This shows the critical force regime that separates the two negative supercoiling force responses of DNA[51].

Even if a plectoneme leads to a general relaxation of mechanical stress, it leads to a necessary sharp bend at it tip. This has for consequence that particularly flexible sections of a DNA molecule seem to be preferential sites for the plectoneme tip to be pinned around. This can be sections of denatured DNA (bubbles)[54], usually AT-rich with a high flexibility, or mismatched regions, even of only one base pair[55]. Also, the stem of the plectoneme, where the DNA molecule writhes around itself, leads to a considerable charge density. Those repelling forces can still be screened by dissolved ions, causing a stabilising effect of plectonemes with higher ionic strength[56].

Quantitative models elaborated by Marko et al. have been quite successfully agreeing with experimental data linking DNA tension, supercoiling density and contour length, and are currently the reference models to compare experimental data of plectonemic DNA to. It still does not fully take into account parameters such as DNA sequence, generally visualizing instead DNA as an homogeneous flexible rod.

$$\beta E_p = \frac{2\pi^2 C(\mathrm{Tw}_p)^2}{L_p + m\gamma} + L_p \frac{A \sin^4 \alpha}{2r^2} + 2m\sqrt{\rho\beta A f} + [(L_p + m\gamma)/2A]\mathcal{U}(r,\alpha) - \ln \Omega(m)$$

Figure 9: Equation from the so-called Marko model, quantifying the free energy of a buckled supercoiled DNA. The term highlighted in green represent the twisting energy contribution, the term in red is the elastic energy of the DNA superhelices, the term in blue is the elastic energy contribution from the m plectoneme tips, the yellow term takes electrostatics in the plectoneme stem into account, and the term in black corresponds to the configuration entropy of the plectonemic domains.

As noted above, those models rely on a relatively simplistic isotropic elastic rod view of DNA, an inaccuracy that increases as contour length decreases. Sequence is suspected to play a significant role in the nucleation and localisation of plectonemes along the DNA contour length, which has been interpreted by S. Kim *et al*. to be mostly linked to intrinsic curvature[34].

VII.2.iv Molecular Dynamics simulations

Another theoretical approach relies on simulating the behaviour of DNA by creating a phenomenological model of molecules and of their interactions, called Molecular Dynamics (MD) simulations. The most precise (atomistic) simulations model molecules as assemblies of covalently linked atoms, interacting with each other[57]. Since every element in the system interacts with every other element present, the computational cost of those simulations rises exponentially with the size of the modelled systems even though cut-off distances are set to moderate this rapid increase. With the current level of computing power available to researchers, simulating an atomistic model of a system such as a DNA molecule a few tens of base pairs long and its solvent environment can yield timescales on the order of 10 nanoseconds per day on a single high-end GPU. This high cost must be accounted for by researchers in their simulations, depending on the size of the system and the length of time it needs to be simulated for. This is why researchers can choose to simplify their model molecule, first by approximating their solvent into fields[58] (implicit generalized Born model), then by changing the molecular model from atomistic to mesoscopic, or "coarse-grained" model such as OxDNA[59], approximating for example the different elements of a nucleotide (Backbone, base) into atom-like elements.

MD simulations are an excellent complement to experimental work, adding a level of precision inaccessible to experimentalists. But this gain in spatial precision is counterbalanced by the typically very short lengths of time biomolecules can be simulated for. Additionally, the current accessible forcefields do not allow the creation or destruction of covalent bonds, meaning that chemical reactions cannot occur in MD simulations. MD are thus adapted to studying other molecular characteristics such as charge density or distribution, bond angles and distances but will be extremely complex to implement to model events such as the action of DNA polymerases, nucleases or topoisomerases.

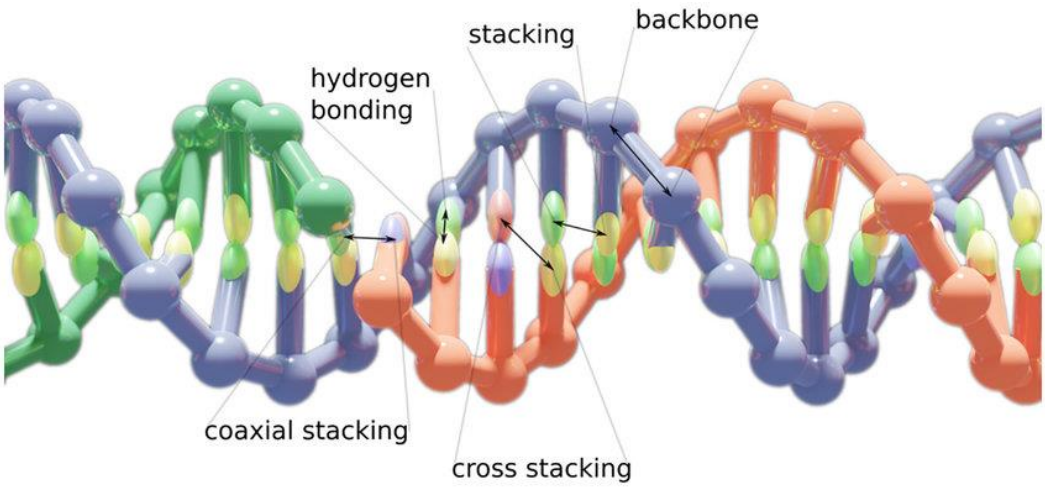

Figure 10: Graphical representation of the OxDNA model, approximating the DNA backbone as a single atom, and nucleic bases as another. The computational savings brought by this model allow the simulation of large tertiary DNA structures like origamis.

VII.3 Single-Molecule Techniques to study DNA

Since its inception around the first half of the 19th century, Molecular Biology has been able to progress at a tremendous pace thanks to the development of simple, quick and inexpensive experimental techniques such as the Western Blot or Gel electrophoresis. Those techniques usually rely on the generation of a signal by a large population of biomolecules, usually outputting an average value of the distribution of the states in the sample. While this allows for the obtention of a strong signal to noise ratio, the individual behaviours of each detected element is lost in the crowd, and dilutes the overall experimental result into a time and/or population average where individual diversity is no longer accessible. This section will thus present the principles behind a newer type of techniques aiming at solving those issues, based around the detection of single biomolecular elements. Those are called single-molecule techniques. While many types of single-molecule approaches exist to image micro to nanoscopic objects, such as Atomic Force Microscopy (AFM), or Electron Microscopy (EM), the practical benefits offered by optical microscopy outweigh by far the higher spatial resolutions of AFM or EM. This stems from the relatively weak impact of non-ionizing visible light on matter. Optical microscopy allows us to image our samples for large amounts of time (up to minutes), in an aqueous environment that represents best the native surroundings of DNA. EM is by nature destructive, is almost impossible to carry out in liquid aqueous conditions and does not capture dynamics. AFM, while relatively simple and easily compatible with a liquid aqueous medium, demands the complete and stable fixation of the object on a flat surface which will impact its native topology as well as its dynamics. Those reasons led to the choice of optical microscopy as a preferred imaging technology.

Beyond simple observation, single-molecule force transduction techniques are needed to perturb DNA and probe its mechanical responses, from tension to torsion. Those techniques will be briefly described, and their strengths and weaknesses compared.

VII.3.i Single-molecule vs. Ensemble Average Techniques

When investigating the properties of a biological system, a great amount of information can be extracted from observing a large population of such system, whether it would be cells or simply biomolecules. The advantage of this approach is that the signal of each element in the sample is combined to produce a much larger signal that is easily detected. In this average signal, the average state of the sampled population is outputted. The appearance and continuous development of single-molecule studies is the consequence of a need for more detailed information, where the individual behaviour of each element is recorded to build more complex models of their actions and properties.

For example, DNA hairpins are biomolecular constructs made of two complementary single stranded DNA molecules. One being much shorter than the other, there is a large single-stranded overhang. By controlling the sequence of the longer strand, one can introduce a self-complementary sequence so that the overhang is able to bind to itself into a loop. Additionally, two nucleotides among this folding domain can be functionalised with a fluorescent dye moiety. When the hairpin is open, each dye will have a classic excitation-emission fluorescent behaviour. But when the hairpin is closed, the dyes will be able to interact to exhibit a distance-dependent fluorescent signal. This signal can be detected to inform the researcher on whether the molecule is open or closed. This behaviour is expected to be dynamic, and dependent on environmental conditions such as temperature[60] or salinity[61].

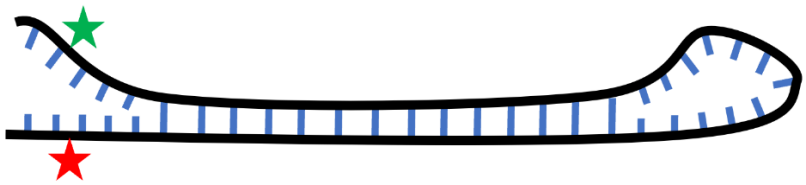

Figure 11: Cartoon of a DNA hairpin. The black line represents the DNA backbone, the blue line paired or unpaired bases, the stars represent single organic dyes able to produce FRET together. Depending on environmental parameters such as acidity, temperature or salinity, the hairpin's stability will be effected, which can be measured through the FRET acceptor emission.

If one were to investigate this process by classic spectrophotometry, measuring the fluorescent response at a range of wavelengths, one could obtain a bimodal distribution centred around the emission wavelengths of both fluorescent molecules, implying a distribution of both open and closed states. While some degree of information can be extracted from this data, like for example the relative proportion of the two folding states, a lot more could still be hidden. By taking a single-molecule approach and observing each DNA hairpin's signal across time by linking

them on a surface for example, one can construct a much more complex picture of the system. For example, exposing folding modes that were hidden in the previous distribution, or quantifying the kinetic constants of this folding transition with good accuracy.

VII.3.ii Single-molecule Fluorescence Microscopy

Fluorescence is a process involving the emission of photons by a molecule after being excited by a photon of higher energy (lower wavelength). The term "fluorescence" was first coined by George Stokes, observing that a fluorite sample exposed to ultraviolet light would emit a blue light. Fluorescence has proven to be an immensely useful tool to life scientists to investigate biological structures and processes. For example, the discovery of mitochondria was allowed by the use of a fluorescent marker called TMRE that was able to bind to their membrane. Initially confined to small organic dyes, the discovery of Green Fluorescent Protein (GFP) by Osamu Shimomura in 1962[62] triggered the explosive expansion of molecular biology. This discovery has had a colossal impact due to the ability to append the genetic sequence corresponding to GFP to those of proteins of interest in biological systems, effectively "tagging" them natively, with a limited impact on the metabolism of the studied cells. This discovery was deemed worthy of a Nobel Prize in 2008, awarded jointly to Shimomura, Tsien and Chalfie.

Made possible by recent technological advances especially in the domain of camera performance and illumination techniques, single-molecule fluorescence microscopy represents the pinnacle of this technology. Pushed to its limits, it allows the localization and discrimination of objects down to a nanometric precision[63] and can function within living tissues and even living animals[64]. This section will attempt to explain the basic principles behind fluorescence and its extension, single-molecule fluorescence, the use of fluorescent probes to image DNA as well as the characteristics of single-molecule fluorescence imaging.

a) Basic principles of fluorescence

Fluorescence is a luminescence process during which a molecule called fluorophore emits a photon a short amount of time after having been put in an excited state by the absorption of a previous photon of a higher energy (lower wavelength). When the excited state is considered metastable and it takes longer to reach a lower energy state, the process is called phosphorescence. The energy difference between absorbed and emitted photons is called the Stokes shift and is characteristic of a given fluorophore. This difference can be due to the deexcited state being of a higher energy than the initial resting state, or inversely, after excitation, there can be non-radiative deexcitation to a slightly lower level before radiative emission occurs.

A large enough group of fluorophores will naturally present a certain variability in terms of energy states, steric configuration, protonation states etc… This gives rise to a broadening of the possible compatible wavelengths to raise a fluorophore to an excited state. Similarly, since the energetic transition from absorbing a photon is often similar to the transition occurring during emission, the excitation spectrum and the emission spectrum are almost always mirrored. They also often overlap.

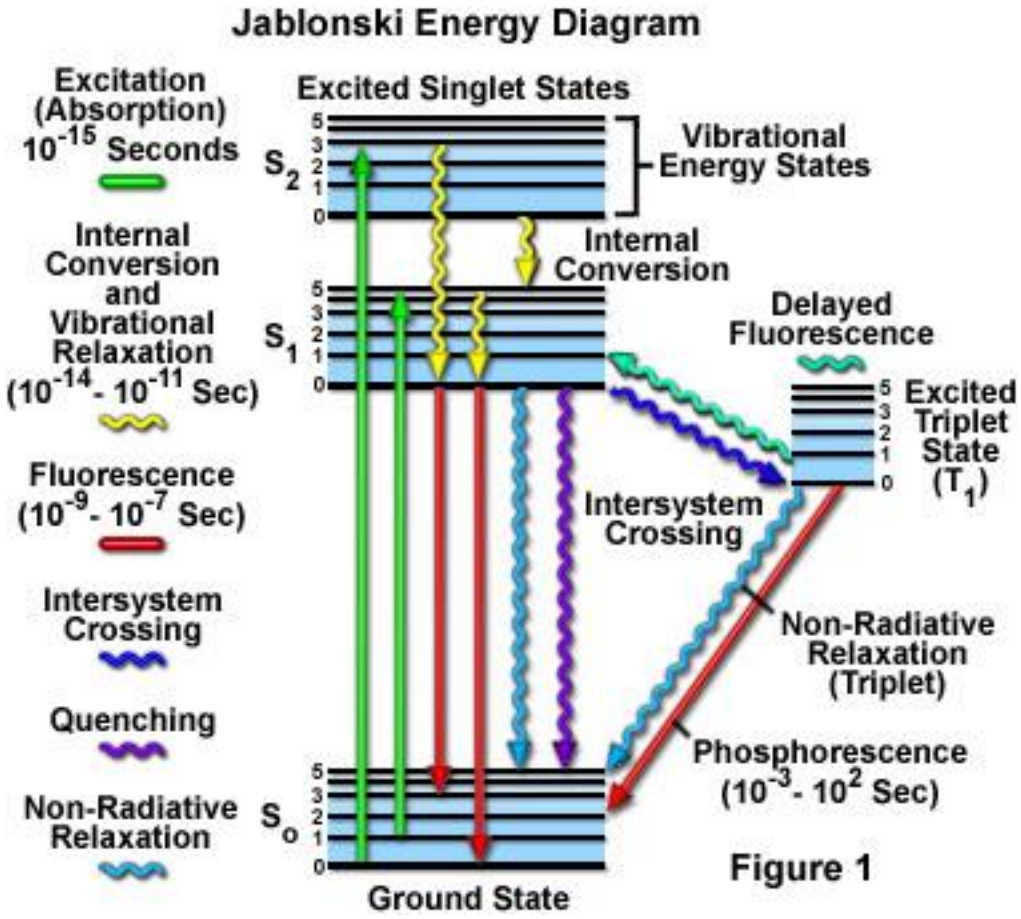

Figure 12: General Jablonski diagram of the various processes involved during a radiative excitation-deexcitation cycle. The colours and styles of arrows indicate a certain type of transition indicated on the left. Relevant time scales of some of those processes are mentioned. Image from micro.magnet.fsu.edu, credits to M. Davidson and I. Johnson.

A given population of excited fluorophores will decrease exponentially through both radiative decay (fluorescence) and non-radiative decay (collisional quenching, dipole-dipole interaction, resonance energy transfer, etc…). The concentration of excited fluorophores [C1] and deexcited fluorophores [C2] are related in such a way:

$$[C1] = [C2]e^{-(\lambda_R t + \lambda_N t)} \quad (28)$$

Where t is time, λ_R the radiative decay rate and λ_N the non-radiative decay rate. λ is typically within the order of a 1 to 10 ns, which is considerably lower than the best acquisition time of most relevant cameras which operate with a frame acquisition time on the order of the millisecond. During a single acquired frame of a video, up to several tens of thousands of excitation-relaxation events will have often occurred for a single detected dye. The specific lifetime of a fluorophore is thus a particularly important parameter to look for to make sure that it is appropriate for a certain type of fluorescence technique. The quantum yield Φ, which is simply the ratio between photons absorbed and photon emitted by a given fluorophore is also a key performance indicator, wanted ideally as close to 1 as possible. As a reference, the quantum yield of tryptophan is 0.13[65], eGFP's is 0.6[66] and fluorescein's is 0.8 to 0.99[67]. The decay of a population of fluorophores can be modulated by the properties of its environment (the solvent)[68], which can be of use to probe the properties of biomolecules

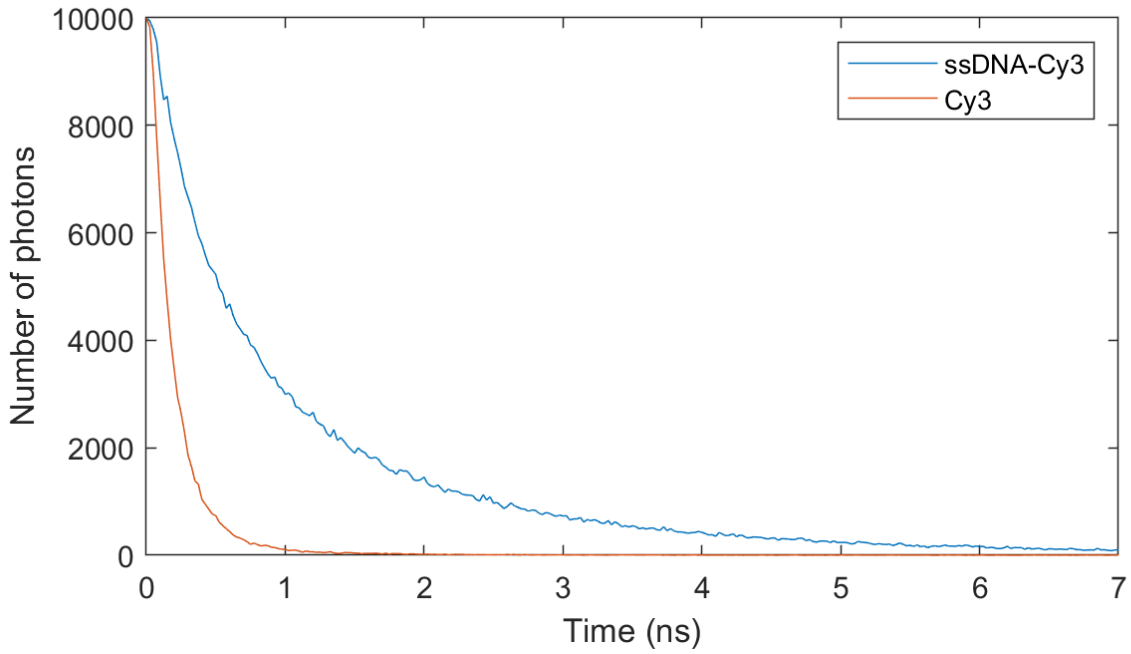

Figure 13: Fluorescence excitation decay recorded during a TCSPC experiment (Time-Correlated Single Photon Counting) unrelated to this project, of two populations of Cyanine 3 dyes: one freely floating, the other attached to the end of a single 49 bp long ssDNA molecule, both in PBS buffer.

The non-radiative decay of an excited fluorophore is not always something to avoid. This process is at the base of an incredibly valuable technique called Forster Resonance Excitation Transfer, or FRET, invented by Robert Forster in 1948[69]. To enable FRET, one can carefully select a pair of fluorophores (A and B). A's emission spectrum must overlap with B's excitation spectrum. A will be called the donor and B the acceptor of the FRET pair. This way, it is possible to excite the first fluorophore (A) at their typical excitation wavelength, then if B is nearby, a non-radiative energy transfer will occur, fluorophore A will thus be in a relaxed state while B will be in an

excited state. B will then eventually return to a lower energy state by emitting a typical fluorescence photon. Radiative energy transfer between A and B is extremely improbable, and the non-radiative energy transfer efficiency is highly distance-dependent (inverse sixth power distance dependance[70]). This resulted in FRET becoming a critical tool to investigate intramolecular dynamics of proteins such as conformational changes or to determine subunit number, as well as detect colocalization and its dynamics.

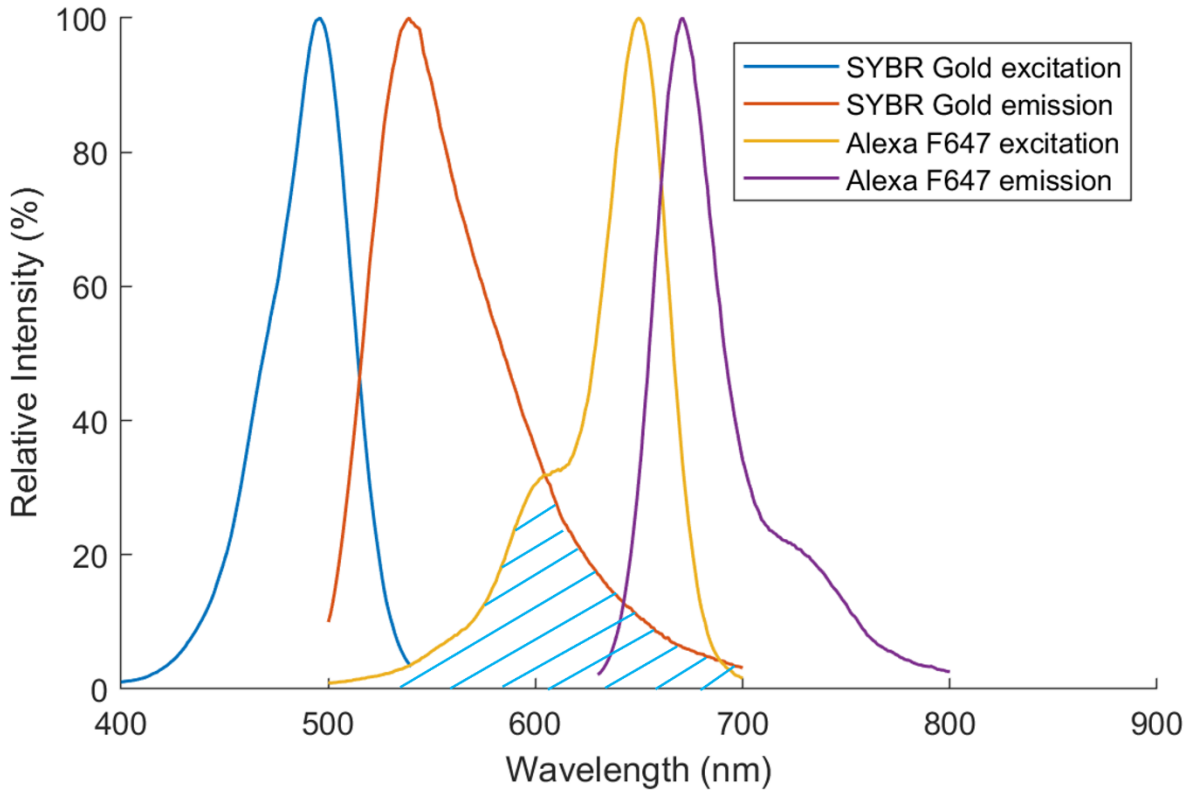

Figure 14: Graphs of the Excitation and emission spectra of two fluorescent dyes: SYBR Gold and Alexa Fluor 647. The dashed area highlights the (relatively small) overlap between the emission spectrum of SYBR Gold and the excitation spectrum of Alexa Fluor 647, overlap that will in theory allow FRET between two near-enough molecules. Data obtained from ThermoFisher.com (SpectraViewer).

The simplest way to measure FRET is to simply measure the individual intensity of the acceptor when exposed to the donor's exciting wavelength. More accurate and sensitive but also more technically complex and expensive, measuring the fluorescence lifetime reduction or quenching of the donor, caused by FRET (FLIM-FRET)[71] is an experimental technique with growing interest. This considerably simplifies the analysis and allows the use of acceptor dyes with poor quantum yields and mitigates several issues of intensity-based FRET measurements such as inefficient FRET or inner filter effects[72]. FRET is far from a single-molecule microscopy-exclusive technique and is more usually carried out in solution in cuvettes using spectrophotometers.

b) Fluorescent DNA probes

DNA itself is very weakly fluorescent[73], but not nearly enough to easily image directly in vitro, and its absorption spectrum is too broad. To be optically imaged easily, DNA needs other molecules to selectively bind to it. Those elements are called fluorescent DNA probes and are widely used by biochemists, notably for their gel electrophoresis assays, but are also a key tool for single-molecule biophysicists. As said previously, the fluorescence characteristics of a given fluorophore can vary depending on the molecule's environment. This includes noncovalent molecular binding. For example, the widely used fluorophore called YOYO-1 alone in aqueous solution will be effectively non-fluorescent, as its quantum yield is less than 10^{-3}. Upon intercalating into dsDNA, its quantum yield rockets up to 0.5[74]. This shift in Φ after binding usually occurs because of a strong decrease in non-radiative deexcitation, the dye being rotationally constrained by the DNA molecule it is bound to.

There are two broad groups of molecular DNA probes: organic dyes and fluorescent proteins. Organic dyes can exhibit a wider range of structures but are usually highly aromatic. They are typically small (~nm), bright (Φ > 0.3) and inexpensive. Fluorescent proteins are found either under a "tagged" form, in which the protein of interest is either coupled with an organic dye, or the DNA sequence coding for a fluorescent protein (usually a GFP variant) is added to a plasmid coding for the protein of interest and produced using a recombinant organism. This last method is an invaluable tool for in vitro live cell imaging, at the cost of a much lower quantum efficiency but with the benefit of a considerably enhanced relevance, as the studied cells do not need to be infused with a foreign compound. It is still possible to hybridize an exogenous organic dye with a specific protein inside of a live cell using FISH (Fluorescence In Situ Hybridization), but this method has gotten less popular due to issues with its specificity and impact on the normal state of a cell. GFP tagging continues to improve through biochemical and photophysical enhancements of the original GFP structure[75,76]. The fact that this project does not aim at studying DNA *in cellulo*, using protein probes does not present much interest and so organic dyes such as SYBR Gold[77], SYTOX Orange[78] and YOYO-1[79] have been used.

Depending on their chemical structure, DNA probes will bind to DNA in different ways. Most of them will be along three possible modes. The first being within the major groove, which is typical of the larger fluorescent proteins. The second would be binding within the minor groove, often more transient and less impactful on DNA, and favoured by longer and curved molecules such as YOYO-1. Minor groove binding dyes typically benefit from a strong quantum yield enhancement post-binding as their rotation along their central bonds are blocked and thus the non-radiative decay lifetime λ_N increases. The third depends on intercalation between two successive base pairs and is favoured for small dyes with a net positive charge and a flat aromatic profile, such as Ethidium. This last binding mode can significantly disturb the secondary structure of DNA and must then be accounted for when carrying out structural studies. Cyanine dyes can interestingly present both intercalative and minor

groove binding modes, as they possess small charged aromatic “heads” joined by a single easily-rotating polymethine chain. Therefore, the effect of each specific probe used in an assay on the mechanical properties of DNA[80] must be fully understood before using it during an experiment looking at studying the properties of bare DNA.

Finally, an important consequence of using a fluorescent probe is the eventual production of radical species due to the dye’s possible transition from its excited singlet state into a reactive triplet state[81] instead of its ground state. Indeed, the production of such reactive radicals is deleterious to DNA and during fluorescence-based experiments, those radicals can react with DNA and form single-stranded breaks called nicks. If the DNA was in any degree of supercoiling, the single bond will provide an axis around which the supercoiled DNA will be able to freely rotate. Eventually, nicks will appear on both strands close enough to each other to lead to the breaking of the dsDNA molecule. This destructive process must be mitigated by the experimentalist to increase the observation times under fluorescent light. For this, one can reduce the amount of incident light, at the cost of a lower signal-to-noise ratio (SNR). One can also use radical quenchers that will react with radical species before they reach the DNA, neutralizing them[82]. Additionally, single-strand breaks can be repaired by having a Ligase enzyme in solution. In any case, the influence of the use of each of those elements is to be investigated, as they all have the potential to disturb the structural properties of dsDNA.

c) Going single-molecule: super-resolution imaging

If a single dye were to bind to a single DNA molecule and was detected with an ideal microscope and camera, the resulting spot would not be of the size of the dye but instead even much larger than the thickness of DNA, by a factor of roughly 100. This is because those conditions meet the criteria for a diffraction-limited system. Indeed, according to Abbe’s law, light of wavelength λ being collected by a microscope objective of numerical index N will generate a resolving power d of:

$$d = \frac{\lambda}{2N}$$

(29)

The current best oil-immersion objective having an N of 1.49 and with a typical wavelength of 500 nm, this result in a resolving power of 167.8 nm, which is to be compared to DNA’s 2 nm thickness. This does not mean that a single point cannot be located with more than about 150 nm accuracy, but rather that two objects will have to be more than 150 nm away from each other to be accurately separated and not counted as one. If it is isolated, a single spot can still be accurately located within a few tens of nm by simply fitting the corresponding signal with a gaussian function (as a simple approximation of an Airy function). Thus, when introducing a detector (camera) in a single-molecule microscope, appropriate care must be taken to match

pixel size of the detector and the optical limit. The more spread out the spot will be, the more accurate the localization, at the cost of reduction of field of view and of the collection of enough photons across the detector. The required sensitivities of modern single-molecule experiments lead to cameras often being the most expensive elements of a bespoke microscope setup along with objectives and lasers.

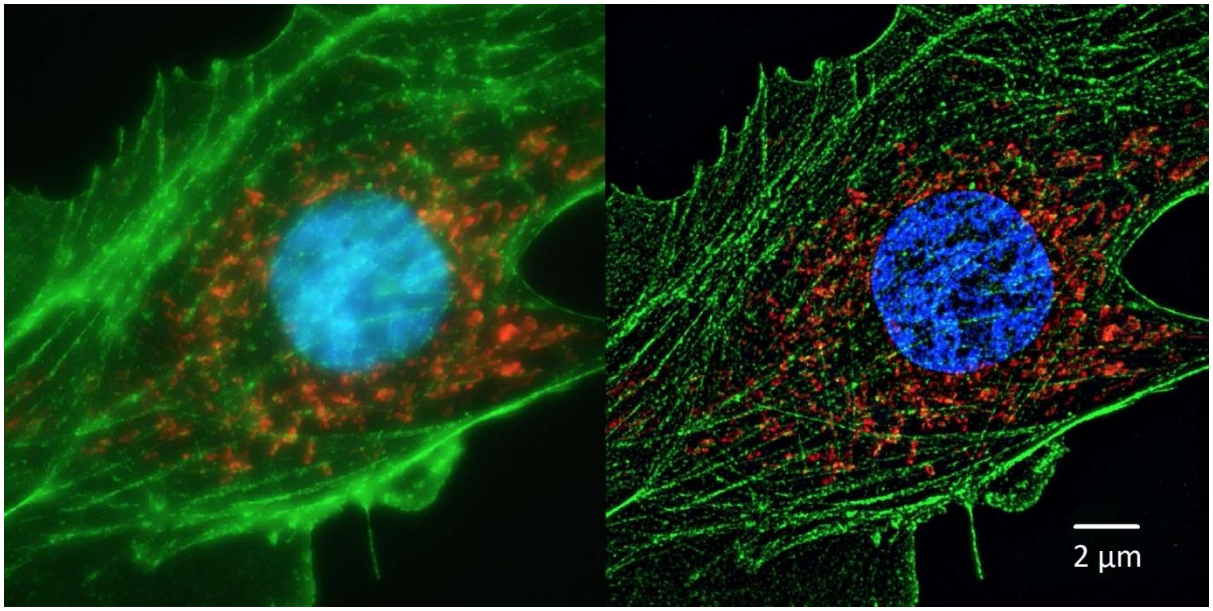

Figure 15: Comparison of the same human cell imaged through normal confocal microscopy (left) and STED super-resolution microscopy on the right. The actin filaments are tagged with a green fluorescent marker, the mitochondria with a red one and the DNA with a blue one. Pictures taken by Dr. Kandasamy, University of Georgia.

Tracking a single isolated fluorophore is relatively easy, but most studied living systems from cells to molecules contain dozens or even hundreds of individual fluorophores, sometimes closer from each other than the optical resolution limit. To enable those samples to be studied with super-resolution, one must ensure to excite only a fraction of the present population at a time. This is made possible by several techniques, STED microscopy relies on the selective depletion of fluorophores located around the region of interest[83,84], STORM/PALM (Stochastic Optical Reconstruction Microscopy/Photo-Activated Localization Microscopy)[85–87], made possible by the engineering of photo-activatable fluorescent probes, relies on repeated activation of a fraction of the population of fluorophores present in the field of view, followed by a reconstruction to enable localization of fluorophores more than 20 to 30 nm apart, which represents a 10-fold improvement on non-superresolved imaging techniques. Those techniques, while exceptionally accurate when well-tuned, are unfortunately struggling when looking at individual freely diffusing molecules. This is due to the photon budget necessary to detect a fluorophore being often too high to allow high framerate acquisition, typically limited to 100 Hz for the best sCMOS sensors, as well as the effectively limited number of excitation-deexcitation cycles a fluorophore can go through before photobleaching.

d) Fluorescence microscopy illumination modes

Every fluorescence microscope has fundamental parts in common. First, lasers are nowadays overwhelmingly favoured as a light source due to their spectral purity, power stability and tunable spectral profile. Several lasers can be combined into one beam. This beam will usually be fed through the back aperture of an inverted microscope body and reflected upwards by a dichroic mirror to and through the objective. The fluorophores inside of the sample will emit fluorescence photons, some of which will be emitted back down and collected by the objective. The dichroic mirror (a high-pass optical filter) should be appropriately chosen to be transparent to that emission wavelength, which will eventually be directed onto a camera. If several lasers are present, then the dichroic will need to be an appropriate band pass filter. Between every physical component cited, the incident light can be manipulated and improve the end signal. Otherwise, if nothing out of the ordinary is done, the system is said to be in epi-fluorescence, which is by far the simplest fluorescence microscopy illumination mode.

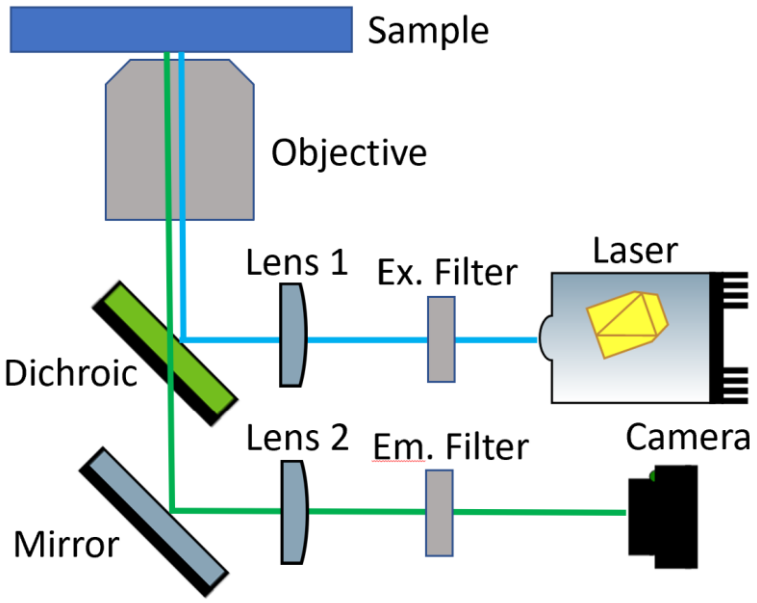

Figure 16: Simplified diagram of a basic fluorescence microscope.

By mounting a lens its own focal length away from the objective on a translational stage perpendicular to the incident laser beam, it is possible to incline the beam coming out from the objective in order to hit the sample at an angle. Beyond a certain value called critical angle, the incident light hitting the sample will be totally reflected internally, but an evanescent wave will still be present and propagate on the sample surface. This wave will allow for the selective excitation of dyes present on the surface and will thus lead to an increase in signal-to-noise ratio. This technique is called TIRF microscopy, for Total Internal Reflection Fluorescence microscopy. While this technique is not well suited to the type of experiments we will describe in the following chapters, a less extreme form of beam manipulation can be applied and

angling the beam at a less extreme angle can still provide appreciable SNR improvement while still penetrating deep enough in the sample. This technique is called HILO illumination[88].

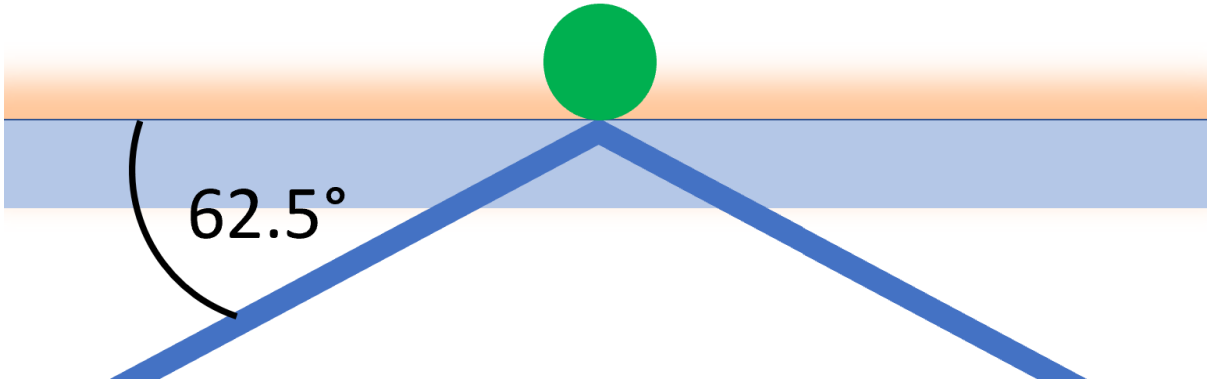

Figure 17:Cartoon of TIRF illumination. In dark blue, the incident and totally internally reflected fluorescence excitation beam, in light blue the coverslip, in green a fluorescent object surrounded by water and in orange the evanescent field responsible for fluorescent excitation. Most of the incident light is reflected away from the sample which will thus lead to a lower background fluorescence at the cost of excitation penetration.

VII.3.iii Single-molecule DNA Tension Transduction

Imaging single biomolecules across time can provide a great insight into some of their properties. But many molecular machines are able to produce significant amounts of force in a living cell. Those forces are then able in turn to effect other elements and processes. Being able to produce (and thus also measure) biologically relevant levels of forces can then provide a tremendous help for the researchers in their understanding of biomolecular processes. This section will attempt to provide the reader with a description of the possible relevant techniques in the context of the following experiments, their strengths and shortcomings as well as comments on when each technique is most appropriate and why.

a) Using Infrared Light

Optical Tweezers (OT) are a device relying on a technology invented by Arthur Ashkin in 1970[89] that became so valuable to the field of Life sciences that this led to his award of a Nobel Prize in Physics in 2018. If a near-infrared (usually 1064 nm) gaussian profile laser beam is focused into a diffraction-limited spot by a high NA objective, it gains the ability to immobilize a transparent object if that object possesses a higher Optical Density (OD) than its surrounding medium and is of a size of same order than the laser's wavelength (0.5-10 µm). By translating the microscope stage

and changing the focus (*ie* the objective relative height), it is possible to translate this optically trapped object in any direction. The potential effecting the force applied on the bead as a function of its distance to the centre has been studied extensively and is relatively easily accessible experimentally. Moreover, any deviation from the ideal central position will perturb the profile of the light coming out of the object, and this deviation can be harnessed to measure forces applied on the bead with a high accuracy and speed. This is achieved by imaging the back-focal plane on a Quadrant Photo-Diode (QPD), which is essentially a high-framerate camera with only 4 pixels arranged in a 2 by 2 pixels square. By coupling such a setup with a piezoelectric stage, it is then possible to produce biologically-relevant forces (few pN), again with high accuracy and speed. Algorithmically coupling the movement of the stage and the detected applied forces provides the possibility of force-clamping, which means imposing a constant tension in whatever direction required.

DNA does obviously not meet the criteria to be optically trappable with 1064 nm wavelength light. It must then be attached to an object that will, in our case a transparent spherical latex bead. This requires appropriate chemistry to covalently link several linkers to that bead, that will be able to attach to a specific chemical group added on a DNA molecule. The two classical systems used are the biotin/streptavidin and the digoxygenin/antiDigoxygenin systems. Those two solutions present no cross-binding, and so allow the selectively oriented binding of two objects at two separate ends of a DNA molecule, which in turn allows the creation of an object colloquially called DNA-dumbbells, for its resemblance with weighted dumbbell. This requires the use of two separate non-interacting trapping beams.

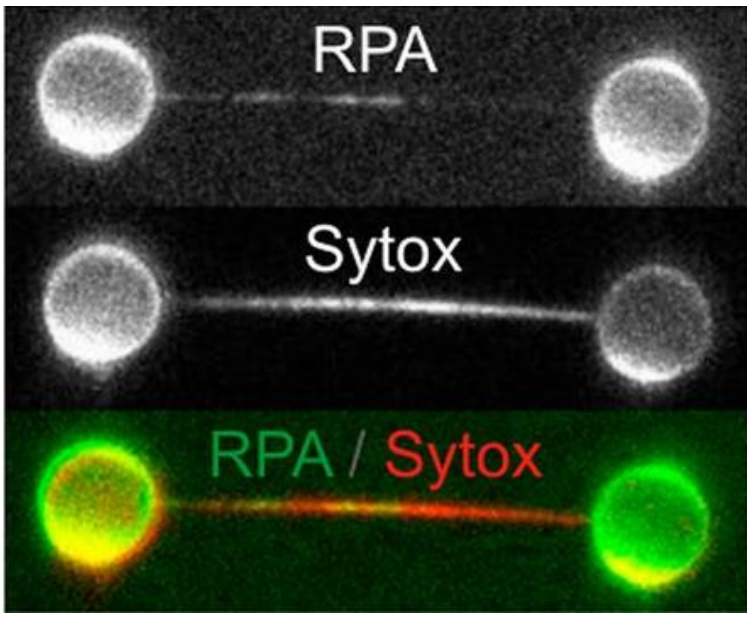

Figure 18: Fluorescence images of an overstretched DNA dumbbell, in two colour channels, then combined. The first channel receives fluorescence signals from fluorescently-tagged RPA protein, which binds to single-stranded DNA. The second channel receives fluorescence signals from dsDNA-bound Sytox Orange, the third channel is an artificially colour combination of both. This shows the local

denaturation of overextended DNA, showing that the molecule localizes this mechanical stress response instead of globally. From King GA et al., Revealing the competition between peeled ssDNA, melting bubbles, and S-DNA during DNA overstretching using fluorescence microscopy. PNAS. 2013

Optical trapping can reliably exert forces in the 0.1 to 1000 pN range depending on the regime of force it is calibrated to be used in, which is well beyond the linear stretching regime of DNA and can even explore over-stretched DNA regimes[90]. It is important to note that when using a spherical trapped bead, it is impossible to control its angle without making significant changes to the optical setup. This means that while translational control over the bead is strong, there is no rotational control and that the occurrence of significant levels of torque and tension will lead to relaxation by rotation of the bead within the trap. Optical tweezers are a powerful tool to probe the properties of a molecule like DNA with high precision[91,92]. And have been used to monitor even active DNA replication[93] or transcription[94].

The main practical issue with this type of setup is that it is relatively complex and expensive in time as well as money to design and build and are typically only used with the biomolecule of interest in a horizontal (along the image plane) fashion even if axial traps have been used[95]. If the user doesn't wish to build a multiple independently moving trap system, they must anchor the other end of the DNA to the surface or previously a pipette and use a piezoelectric stage to stretch DNA controllably. The optical trap then acts purely as a force measuring device rather than an actual force transduction device. If two traps are needed, then one must split the IR beam into several, either by splitting it into several polarization components or by timesharing it with acousto-optics. If timesharing is chosen, it must be carried out at timescales higher than the typical relaxation rate of a trapped bead, usually beyond 10 kHz[96]. If static splitting is chosen, it becomes much harder to use the outcoming IR light to measure forces.

b) Using magnetism

A second commonly-used way of generating tension on DNA relies on the use of Magnetic Tweezers (MT). Again, DNA is not sensitive to low intensity magnetic field, so the attachment of a paramagnetic object, typically a latex bead infused with Magnetite (Fe_3O_4) nanoparticles. Holding a permanent magnet close to the sample will orient the bead along the magnetic field lines, as well as some attraction due to the locally uneven magnetic field. As a consequence, using permanent magnets to manipulate microbeads can introduce challenges and necessitates careful calibration of the system, especially to track the bead position in the dimension perpendicular to the image plane.

Most MT experiments are usually carried out in a vertical fashion, where the DNA is held perpendicular from the sample surface, forbidding accurate localization of binding events or secondary structures along the DNA contour length. It is possible to design an apparatus that allows changing the magnet position after supercoiling is

applied so that the DNA tether is held horizontally[56], but the resulting small separation between surface and biomolecule might introduce a bias in the observed behaviour of DNA, and it can be difficult to ensure an even illumination of the molecule along its contour length.

The strengths of this single-molecule manipulation technique revolve around its simplicity, and the fact that it lends itself particularly well to multiplexing, as a large number of particles can be manipulated and tracked at the same time[97]. Its main weakness is that video tracking is the only way to quantify the force applied on each bead with no other direct feedback from them. Video acquisition in fluorescence can also be difficult to do, due to depending on the available camera framerates. Thankfully, a large amount of work has been done to help new users build and calibrate magnetic tweezers systems[98,99].

c) Using Flow

A third possible way of exerting physical forces on DNA is to use the flow of the surrounding liquid to stretch DNA in its direction, and was the technique first used to stretch DNA molecules in water. This approach lead to the development of the technique known as DNA curtains[100,101], in which a large amount of DNA molecules attached in a row perpendicular to the flow are stretched and imaged simultaneously, which provides an appreciable throughput boost by effectively multiplexing the experiment across the whole microscope field of view.

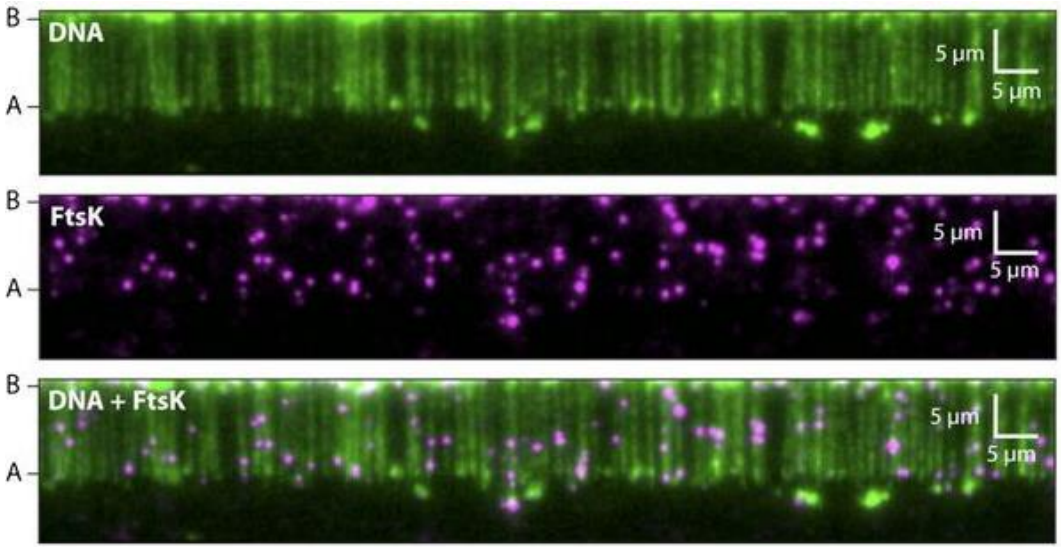

Figure 19: Fluorescence microscopy images of a DNA curtains assay, showing the YOYO-1-labeled and flow-extended DNA molecules only in the first channel, the fluorescently labeled FtsK translocase protein in the second channel, combined into a single image in the bottom channel. From Lee J et al [101].

Independently of force production, control of flow within a sample is an appreciable upgrade to a single-molecule microscope, as it allows the experimentalist to carry the same experiment on the same single-molecular complex but in different chemical environments. Using the properties of laminar flows, it is even possible to create a sample in which several channels of different composition can flow alongside of each other and be freely accessible by an optically trapped object. But careful considerations must be taken to characterize the true nature of the flow near the surface, as no-slip conditions dictated by fluid mechanics dictate a varying flow profile as a function of height.

c) Other methods

Several other methods exist to produce tension on a DNA molecule. An Atomic Force Microscope (AFM) can be of use for this. Since the method depends on the precise detection of a force applied on a nanoscopic cantilever, it can also be used to accurately produce those forces. Therefore, by attaching a DNA molecule between the cantilever tip and the sample surface, one can precisely stretch the biomolecule[103]. This unfortunately doesn't allow the imaging of the molecule easily, and in-liquid AFM is notoriously more complex and expensive than dry AFM which itself requires a considerable amount of expertise and optimization.

The recent advent of DNA nanopore sequencing promoted the use of those devices for different purposes. A natively charged DNA molecule can be trapped within such a pore, and one can apply and electric potential to force its translocation through the membrane, enabling the use of those nanopores not just as sequence or contour length measuring device, but also controllable force-transduction devices[104] that can even be coupled with optical trapping[105]. Again, this method is not suitable for an approach aiming to image the DNA molecule and is only suitable to study other properties of DNA fragments. It is on the other hand one of the leading techniques for Next Generation Sequencing (NGS) techniques[106,107,108].

A final example of a microscale force transduction technique is acoustic trapping, using sound MHz-frequency soundwaves to manipulate micro-scaled objects such as cells across length scales of hundreds of nanometres. This technique functions by forcing objects to localize within the pressure nodes of a standing acoustic field, the same way as a powder spread on a metal plate that is made to vibrate will self-organize to form frequency-dependent patterns. This permits effecting forces on the order of the piconewton on micrometer-scale objects. This technique has been applied to the manipulation of single cells[109], with the advantage over light-based techniques being a much higher damage threshold due to lower power densities. This type of technique lends itself well to multiplexing, allowing the simultaneous manipulation of up to several dozens of objects[110], but selective control can also be achieved using focused beams[111].

VII.3.iv Single-molecule Torque Production

The previous sections of this document have underlined the fact that tension is only a part of the picture when investigating the physical response of DNA to perturbations. Torque is a critical parameter. Affecting one is not enough, both should be reliably and independently controlled to obtain a detailed insight into the physics of DNA. OT and MT techniques that have been introduced previously can be used to do this, and we will then show that since none of them is perfect for our specific use case, a combined approach linking both MT and OT is the key to achieving full control on the topology of DNA.

a) Using magnets

To impose a torque on a DNA molecule, permanent magnets are still the simplest and cost-effective solution. To twist a magnetically tweezed DNA tether, one simply needs to rotate the magnet above the sample along the axis perpendicular to the image plane. As long as this type of experimental configuration is chosen (vertical), this solution is by far the best. If a horizontal DNA configuration is needed (to image it for example), then additional constraints appear, notably due to the limited lateral clearance around the sample plane. An important shortcoming of the use of permanent magnets is the difficulty in obtaining a locally homogeneous magnetic field. If a significant gradient is present, the beads will experience varying levels of attractive force towards the magnet, and decoupling tension and torsion becomes particularly difficult.

To circumvent this issue, it is also possible to use electromagnets instead of permanent magnets, in the form of at least two perpendicular pairs of Helmholtz coils through which two amplified oscillating signals with an orthogonal phase can be fed. This technique provides the advantage of a higher control over the magnetic field, in the form of varying power, oscillation profiles, speed and does not introduces any vibrations in the system, which only limits the spinning rate of a bead by its hydrodynamic drag. Also, by choosing an appropriate size and separation between each coil, one can produce a homogenous field across several mm^2, which is far beyond the typical field of view of a single-molecule microscope. This allows the production of torque without any attraction towards the magnet. Furthermore, the axis along which the magnetic field rotates does not have to be perpendicular to the sample plane, so it is easy to implement this to allow rotation parallel to the sample plane, which enables detecting the DNA molecule along its entire contour length through fluorescence microscopy.

Magnetic torque tweezers have been used extensively to investigate the response of DNA to mechanically induced supercoiling[50,53,112], but also study the impact of DNA-processing enzymes such as topoisomerases[113,114] and polymerases[115] which can create or relieve torsional stress on a DNA molecule.

b) Using a polarized Optical Trap

It is possible to impart some level of torque on an optically trapped particle, by polarizing the trap's incident light and imposing a rotation of that polarization over time. It isn't possible to impose a torque on a spherically symmetrical object. One can use "imperfect" microspheres with edges and dents[116], but this introduces issues in modelling the response of such irregular objects[117]. Instead, the common method used is to produce cylinders from the cleaving of an etched surface, which are then functionalized with a binding protein[118]. This approach is complex, cannot allow rotation along a horizontal axis and cannot be parallelized, but enables the user to leverage the accurate and video-independent high-bandwidth detection of force typical of optical tweezers systems, which can be necessary in some cases.

An original technique was recently developed by King et al, able to induce negative supercoiling in DNA using a classic double trap setup[119]. This technique relies on the production of two highly stiff traps able to move independently. A DNA molecule is attached between two beads and subject to considerable stretching force (above 20 pN). This causes the stretching of the molecule without changing its linking number. Indeed, while the two beads forming the dumbbell are freely floating, the torque induced by the overstretching of the DNA will not be enough to cause the much larger beads to rotate, due to surface-related drag. While overstretched, one of the two non-covalent biotin-streptavidin bonds at each end will stochastically break, allowing the DNA to unwind. The biotin-streptavidin link will eventually be reestablished and the result will be a negatively supercoiled DNA molecule. This can be repeated for increasing levels of supercoiling. While this technique is impressive in its simplicity and ingenuity, it is not possible to positively supercoil DNA, or impart a predefined level of supercoiling since it is based on uncontrollable stochastic events.

c) Using intercalators

The binding of an intercalator dye in-between two base pairs has been shown to extend that pair's effective length by up to 100%. This means that the effective helicity of DNA will be halved. If a DNA molecule is kept topologically constrained (both ends prevented from rotating) before being exposed to intercalators, their binding will change the DNA linking number, resulting in an eventual buckling. C. Dekker et al used the action of the intercalator SYTOX Orange, an exceptionally bright dye, to induce supercoiling in DNA molecules bound by their two ends to a surface, detecting the presence, nucleation as well as diffusion of plectonemes[120].

VII.3.v Best of both worlds: Magneto-Optical Tweezers

It is rather easy to notice that optical trapping and magnetic tweezing complement each other particularly well. Where one excels in accurately producing and measuring tensile forces (optical traps), the other finds its main weakness. Where one shines by its ease to produce simple and reliable torque (magnetic tweezers), the other shows a need for complex fabrication methods and optical design. Those facts lead us to choose a combination of both technologies to produce a device able to independently produce tension and torque, while allowing the imaging of a DNA molecule along its entire contour length.

To produce a rotating magnetic field, the Helmholtz coil method was chosen due to the advantages listed above, along with a robust single optical trap. To produce tension, the device is equipped with a piezoelectric stage which enables precise 2D movement. The DNA molecule of interest will be attached on one end to an anchor bead stuck to the surface to achieve topological constraint, the other end will be attached to a magnetite-infused microsphere held suspended in solution by the optical trap.

This device can provide an unprecedented level of control over the topology of single molecules of DNA while still remaining visible thanks to the combination of four techniques: optical trapping, magnetic tweezing, force transduction and single-molecule fluorescence.

VIII Experimental Techniques

This chapter will attempt to describe the various experimental procedures carried out during this project.

VIII.1 General Experimental Considerations and Data Acquisition

VIII.1.i General Experiment Configuration

The chosen experimental configuration is a result of the available components in the system and their role. We chose to use the optical trap as a force measuring device, but it is not really able to produce forces on its own, due to its static nature. Instead, we combine it with the nanostage, which will be able to move the surface of the sample with great precision in 2 dimensions. This results in the need for the studied DNA molecule to be anchored to the surface. We chose to do this by using large microspheres (~7 µm diameter) stuck on the sample glass surface, and we will call those anchor beads in the rest of this document. Those anchor beads are functionalized with an antibody protein called anti-Digoxigenin (anti-DIG) which can noncovalently bind with a small digoxigenin molecule. This moiety can be covalently bound to nucleotides, providing us with the ability to attach a DNA molecule on the anchor bead. One end of the DNA molecule is functionalized with digoxigenins, the other end is functionalized with biotin which are able to bind to streptavidin or neutravidin proteins. Those elements will provide us with the ability to form tethers in situ, with great stability as the biotin/streptavidin bond is the strongest noncovalent bond found in Nature[121] (10^{-14} mol/L affinity constant), and the DIG/anti-DIG bond is weaker[122] (dissociation constant K_d of 12 nM vs 0.1 pM for biotin/streptavidin) but still largely sufficient. We thus have an asymmetrical DNA functionalization and can then work with a consistent orientation. The biotinylated end of the DNA tether will be attached to a smaller microsphere (2 or 3 µm diameter) to keep it from touching the surface with a horizontal tether.

Figure 20: Cartoon of the magneto-optical tweezers experiment configuration. The AntiDig-covered anchor bead in dark blue, magnetic trapped bead in light blue, dsDNA tether in between. The optical trap is symbolized in red, and the Rotating blue arrow symbolizes the oscillating magnetic tweezers.

VIII.1.ii Tethering Experiment Protocol

A tethering experiment typically unfolds as follows:

a) Preparation step

Work during this step aims at preparing the microscope, checking that all the components in the system function allowing them to run long enough to reach stable regimes.

Steps:

- Turn on Magnetic Tweezers system at least 45 minutes in advance, set its angle to 45° to allow current through both coil pairs.

- Turn on the fluorescence laser 30 minutes in advance.

- Control that the spot of the optical trap comes out of the condenser lens clean with yesterday's sample.

- Turn on the Camera, cool down its sensor to -80°C (10 minutes)

b) Calibration step

This step must be repeated for every tether formed or found, in order to mitigate the fact that different magnetic beads displacement within the optical trap lead to different responses that must be precisely quantified every time to output credible displacement and thus force values.

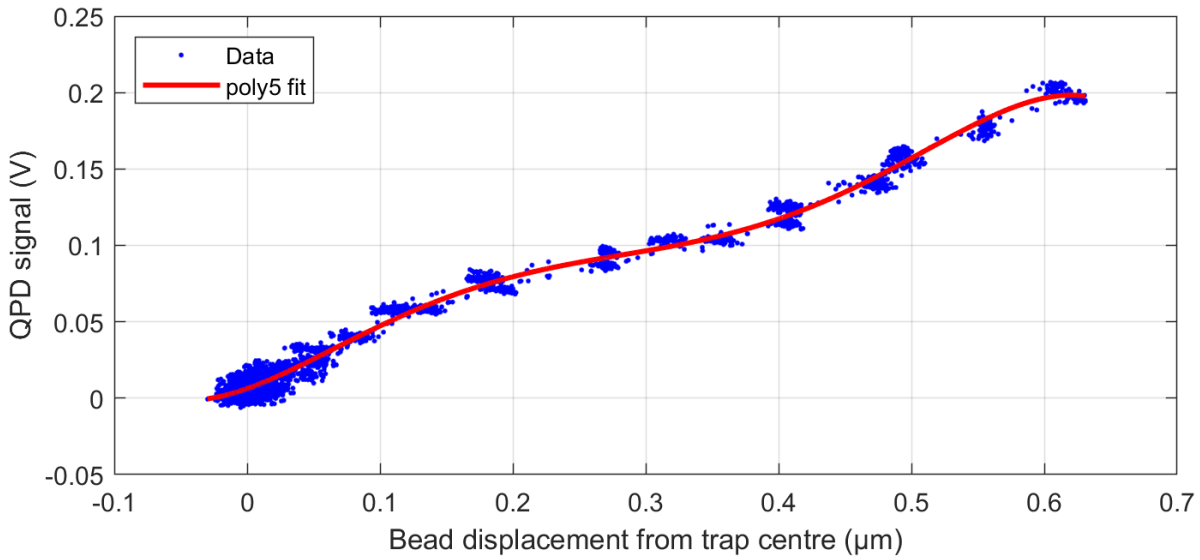

Figure 21: Example of a QPD signal-bead displacement fitted to produce a calibration curve.

Steps:

- Find a "pre-formed" tether, or create one by manually moving a trapped bead in the close vicinity of an anchor bead until tether formation (the bead is pulled out of the trap as the stage is moved)

- Manually orient the bead to be roughly vertically aligned with the anchor bead

- Extend the tether using the nanostage, monitoring the perpendicular force measuring QPD channel. If a significant signal is detected, reorient the trapped bead laterally and try again, until the perpendicular channel outputs no signal as the tether is extended.

- Extend the tether until the trapped bead is displaced by 100-200 nm from the initial centre of the trap and keep it in position for 10 seconds to let possibly present secondary structures or nonspecific adhesions relax and unravel.
- Relax the tether, bringing the beads close together to about 1 µm.

- Turn on video and QPD acquisition, then extend the tether in increments of 50 nm, with 1-2 s of pause in between each step, until the bead is displaced by ~50% of its radius (750 nm).

- Repeat the above step in the opposite direction, until the trapped bead is back in its original position related to the anchor bead, then turn off QPD acquisition.

c) Force-extension step

The force-extension behaviour of DNA molecules is well known and has been extensively characterized. Carrying out this measurement on each DNA molecule studies should be done as it is non-destructive (no reliance on fluorescence) and provides a decent benchmark of the "quality" of this particular construct. It can help detecting possible nicks or multiple tethers.

Steps:

- Turn on the nanostage "tapping mode" (sawtooth movement pattern) and start oscillating the stage along the tether with a 1 µm amplitude. Make sure to monitor the perpendicular force channel the entire time to detect any lateral drifting from the previous configuration.

- Increase the stage amplitude carefully, until a bead deflection of approximatively 500 nm is detected.

- Turn off the camera LIVE feed, turn on the Labview Data acquisition then acquire a video. Aim to acquire approximatively 10 stretch-relax cycles.

- Turn off the QPD acquisition, then stage tapping mode.

d) Twisting step

- Extend the same tether as much as possible, without detecting any significant QPD signal/bead deflection. Turn off LIVE feed, turn on Labview data acquisition then acquire a small video sequence to register the initial bead position.

- Start a new video acquisition then quickly start "removing" 50 turns from the DNA molecule by applying 50 cycles in the Magnetic Tweezers module. If tension detected quickly increases, there is more than 1 DNA tether.

- Repeat the previous step until the target DNA undertwisting value is reached.

- Apply the sum of turns added in previous steps, with the opposite phase (overtwisting DNA). This resets the DNA molecule in its initial supercoiling state.

- Start a new video acquisition then quickly start "adding" 50 turns from the DNA molecule by applying 50 cycles in the Magnetic Tweezers module.

- Repeat the previous step until the target DNA overtwisting value is reached.

- If fluorescent probes are present, turn off the brightfield illumination, start video acquisition then turn on the fluorescence laser, until tether breakage.

VIII.2 Optical Trapping

Optical trapping is nowadays a workhorse of single molecule biophysics studies. It is a relatively simple to set up but also deceptively complex technique that enables the ability to sense the forces involved in fundamental biological processes like DNA replication or even kinesin mobility. This section will aim to accurately describe and explain the specific design of the optical trap module on this microscope.

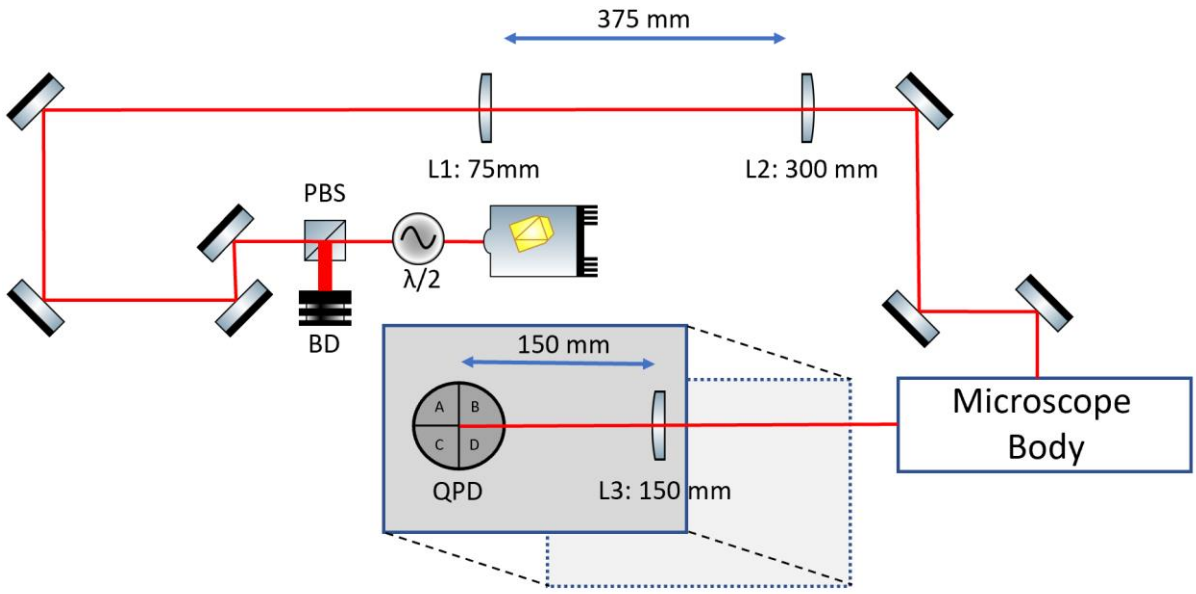

Figure 22: Schematic of the Optical Tweezers layout. Double-ended arrows indicate relevant distances between components. Each important part of the setup will be described in detail later in this section, namely power regulation, beam delivery and force spectroscopy modules.

VIII.1.i Fundamentals

An optical trap typically consists in a near-infrared (most often 1064 nm wavelength) beam tightly focused by a strong (high Numerical Aperture) objective. For a Gaussian laser beam of given wavelength, the theories behind its mode of action vary depending on the size of the trapped particle. We will focus on the case in which the particle is of larger diameter than 1064 nm. If the particle's refractive index is sufficiently different from the index of its surrounding environment (water), it will experience two forces while in the vicinity of the trap. The first one is called scattering force or radiation pressure and is directed along the direction of propagation of the light. It is is the result of conservation of momentum of the photons reflected by the bead. The second force, called trapping force or gradient force, can also be explained

by conservation of momentum but this time as a consequence of light refracted by the particle into the buffer.

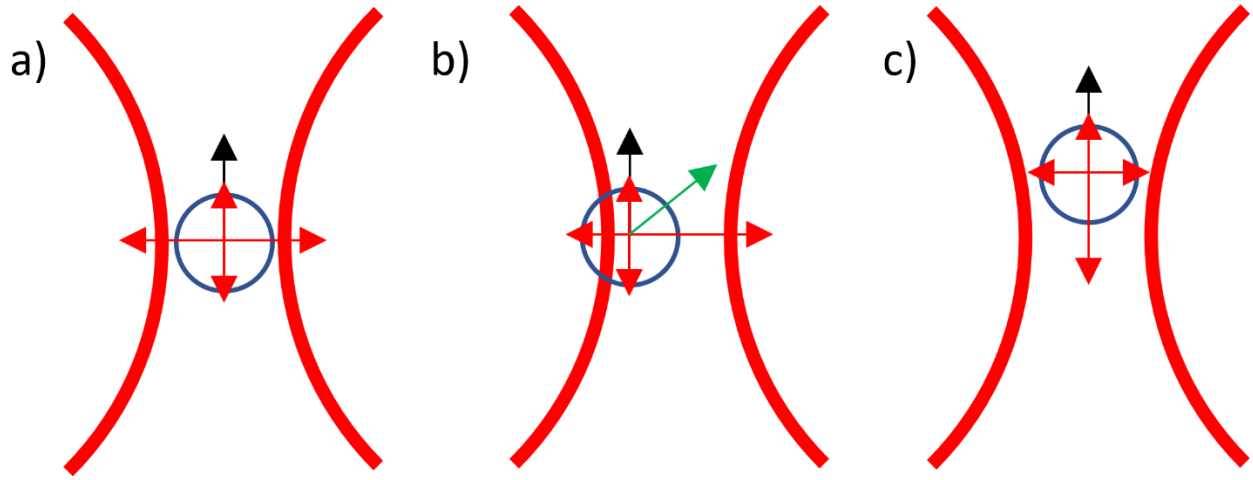

Figure 23: Force diagram of the optical trap-induced forces experienced by a bead at several points relative to the trap centre. a) The bead is located perfectly aligned with the region of highest intensity (beam waist). The resulting gradient force (components in red) is nil, while the radiation pressure force is directed upwards. The total force is thus exactly the radiation pressure force, pulling the bead upwards. b) The bead is vertically aligned with the beam waist, but horizontally deflected. The vertical component of the gradient force is nil, its horizontal component is directed towards the centre of the beam waist. The radiation pressure force being still present, the resulting force is oblique, symbolized in green. c) When the bead is in its equilibrium position, it is vertically aligned with the beam waist, negating its horizontal gradient force components and resulting in a downwards gradient force. The magnitude of this force matches the radiation pressure, the beads thus stays suspended in the same position relative to the beam waist.

The inputted laser beam being collimated and with a gaussian profile, it is focused by the objective into a diffraction limited spot which location is called the beam waist and present the highest light intensity. Along the axis of light propagation, the local intensity thus increases towards the beam waist, then decreases past it. The same can be said laterally. As a consequence, a bead that isn't centred on the beam waist will experience a force directed towards that location as one side will be refracting a higher amount of light as the other one. At equilibrium, the trapped particle has scattering, trapping and gravitational forces balanced, which results in its maintained position centred laterally on the beam waist and slightly downstream from it.

The potential produced by a Gaussian profile beam is Gaussian itself, with the following form

$$U(x) \propto e^{\frac{-(x-x_0)^2}{2\sigma^2}} \quad (30)$$

Which for an ideal point-like trapped particle results in a force such as

$$F(x) \propto (x - x_0) e^{\frac{-(x-x_0)^2}{2\sigma^2}} \quad (31)$$

This can be approximated to a cubic function whose two inflection points define the region around the centre of the trap in which the trapped bead will experience a linear force as a function to displacement, which will be the useful region for our studies.

VIII.1.ii Construction of an Optical Trap

The construction of a functional optical trap is a rather simple task, that essentially relies on directing a collimated beam of near-infrared laser light coupled into the back-aperture of a high-Numerical Aperture objective, above 1.2. It should be equipped at the very least with an adequate power-regulation system, independent from the laser head itself, as well as an appropriate beam delivery into the objective with careful alignment to ensure the production of a functional and symmetrical trap.

a) Power regulation

The typical laser beam powers used in optical trapping, on the order of 100 mW, are actually significantly above those used in most fluorescence microscopy modes (0.1 to 20 mW). The laser emitter chosen in our case is capable of a 4 W maximum output at 1064 nm (class 4 laser). As a reference, commonly used laser pointers output a beam of power less than 0.5 mW. For power stability reasons, it is not advised to run the laser at a small fraction of its maximal operating power, so there is a need to controllably and reliably modulate the beam power downstream from the emitter itself. This is achieved by first running the beam through a half-wave plate mounted on a rotational mount. This allows us to modulate the fraction of the beam that is vertically or horizontally polarized. The beam is then directed into a polarization beam-splitter which redirects one of those two components safely into a beam dump. The rest of the beam is then used for the optical trap, and we are thus able to modulate the power of the beam by simply rotating the half-wave plate, through an electronically controlled motorized mount.

The Laser being quite powerful as well as enclosed for safety, a cooling system was devised to prevent its shutdown by overheating. This was done by mounting the laser head sideways, attaching a radiator to it with thermal paste in between for good heat conductivity, and a PC fan was placed in front of that radiator. While it is not ideal for the beam stability to have turbulent air currents present, this solution was deemed

cost-effective enough to keep, with a possible future upgrade using a more expensive watercooled Peltier module, transporting the heat away from the enclosed box.

b) Beam expansion and delivery

Most high-end laser systems, including ours, are able to produce a well collimated laser beam, but they also tend to have a near but non-ideal gaussian cross-section. In order to mitigate this issue, the beam can be expanded using a Keplerian telescope formed by two plano-convex lenses separated by the sum of their focal lengths. The ratio between the focal lengths of the downstream and upstream lenses results in the expansion factor of the beam, that will stay collimated. If the beam waist is larger than the back aperture of the objective, the part of the beam that will penetrate it will have a near-Gaussian profile, greatly improving the trap profile and thus its stiffness.

Once the beam is expanded, great care must be put into delivering the beam into the objective. The beam must hit the centre of the back-aperture, parallel to the lens' optical axis. This can be achieved using a pair of mirrors before the delivery to steer the beam to satisfy both of those criteria (beam position and angle). This should initially be done by eye with the objective removed, using a card made of IR-sensitive fluorescent material. Once this is achieved, one should mount the objective in its socket, insert a tunnel slide sample full of water and focus on the coverslip surface inside of the tunnel. By removing protective IR filters in the image path, one will be able to detect the reflection of the optical trap on the surface and make finer adjustments until a symmetrical four-lobed pattern is present.

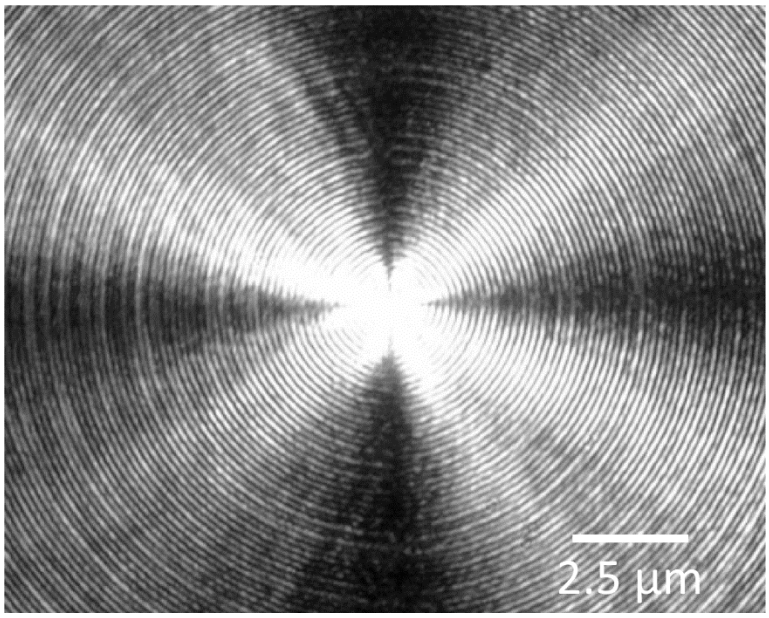

Figure 24: Image of the back-reflexion of the optical trap on the sample coverslip.

VIII.1.iii Measuring Forces with an Optical Trap

As explained earlier, an optically trapped particle will experience a net force pulling it towards an ideal position within the optical trap. Any deflection from this position is the result of another applied force. Therefore, by measuring the deflection of the particle along with a few other parameters, it is possible to use the trap as a force sensing technique. The microscope fluorescence imaging camera can be used to monitor this deflection, but its bandwidth is too low to be acceptable. Instead, the use of Back-Focal Plane (BFP) interferometry is a much more accurate and higher bandwidth technique that is relatively easy to implement, provided that the appropriate carte is taken to calibrate the system.

Installing a BFP interferometry module simply requires filtering the outcoming near-Infrared light downstream of the trap itself and redirect it through the condenser onto an “imaging lens” that will focus it onto a Quadrant-Photodiode (QPD). This allows the detection of the bead deflection from the trap in 3 dimensions at bandwidths beyond 50 kHz, up to 80 kHz without a specialized PCI-E acquisition system.

a) Quadrant Photodiode System

The QPD is an assembly of four photodiodes, brought close together to form a quadrant separated into North West, North East, South West and South East quadrants. Each quadrant is linked to two others, forming a “top” and “bottom” half, and a left” and “right” half. As each diode is illuminated, it outputs a voltage, directly proportional to its illuminance. By measuring a voltage difference between two halves, one can infer the position of the centre of the beam hitting the QPD along that dimension. By linking the vertical and horizontal dimension, divided by the total illuminance, one gets the absolute position of the beam on the sensor. The detector being sensitive, it is important to carefully modulate the power of the incident beam to make sure to stay in a linear response curve regime as the power varies. While photon budget is a critical resource during visible light fluorescence experiment, we are in this case not constrained in any way, far from it. The inputted trap power being on the order of 100 mW, even collecting 10% out of the sample and into the condenser lens still results in considerable levels of light, able to damage the device. This modulation can be achieved by adding IR-rated filters and ensuring that the device receives less than 1 mW of infrared light and outputs a SUM signal between 2 and 10 V.

When a bead is trapped, and thus close to the centre of the trap, it perturbs the profile of the outputted beam shone on the QPD. This perturbation is measured and translated into a force by the processes described below.

b) Stiffness Calibration

The one-dimensional movement of a free particle diffusing in a fluid is a well characterized system, governed by the Langevin equation:

$$m\frac{d^2x}{dt^2} = -\lambda\frac{dx}{dt} + \eta(t)$$

(32)

Where x is the position of the particle, λ is the hydrodynamic drag and η a random force representing the stochastic impact of fluid molecules on the particle. The first inertial term can be safely ignored due to the low Reynolds number at such scales, we are thus left with:

$$\frac{dx}{dt} = \eta(t)$$

(33)

While a particle is held in place by an optical trap, it is still subject to this random force, but also to the force induced by the trap, keeping it in its optimum. As long as parameters like the bead size, the environment temperature and the liquid's viscosity are known, it is possible to essentially compare the movement of the bead while trapped with its theoretical behaviour and extract a trap stiffness, assumed linear around its centre.

The first method to extract this quantity uses the equipartition theorem, dictating that the average kinetic energy of the bead in a given dimension is $1/2k_BT$. Since the potential around the centre of the trap is quadratic, this results in the following equality:

$$\frac{1}{2}k < x^2 >= \frac{1}{2}k_BT$$

(34)

$$k = \frac{k_BT}{< x^2 >}$$

(35)

With $<x^2>$ the mean-squared displacement of the bead. This technique is quite easy to implement, especially if the operator is missing a back-focal plane interferometer and must rely on a camera. While it can be used to sanity-proof the results obtained by a different method and usually gives a figure on the order of the

actual stiffness, it should not be used if one has access to a high-bandwidth detector like a QPD.

Instead, the best method to extract the trap stiffness is to instead look at the power spectrum of the bead's movement while held by the trap. The actual displacement in nanometres does not need to be calculated, so this method relies on obtaining the raw trace of the bead on the QPD for a short amount of time, typically around a second or two and Fourier transforming it. The typical power spectrum density graph of such an experiment ranging between 0 and 2000 Hz, a typical camera cannot be used due to their frame averaging effect, as their acquisition rate is typically between 40 and 100 Hz for high-end devices geared towards single-molecule detection.

The typical power spectrum density (PSD) graph of a trapped bead starts at low frequencies with a plateau, and decays at higher frequencies with a $1/f^2$ dependency. This signal can be fitted by a Lorentzian function, such as:

$$(f) = \frac{D}{\pi^2(f^2 + f_c^2)}$$

(36)

Where D is the diffusion coefficient ($\frac{k_B T}{\zeta}$) and f_c the corner frequency, that points towards the critical frequency value where the bead's movement spectrum transits from trapped to diffusive (the bead is held fast at lower frequencies, but is still able to diffuse at higher frequencies, Brownian motion being mitigated but not erased). The trap stiffness and corner frequency are related according to the following relation:

$$k = 2\pi\, \zeta\, f_c$$

(37)

Where ζ is the viscous drag coefficient and k the trap stiffness. Therefore, since the particle is a sphere of radius r in a liquid of dynamic viscosity η,

$$k = 12\, \pi \eta r f_c$$

(38)

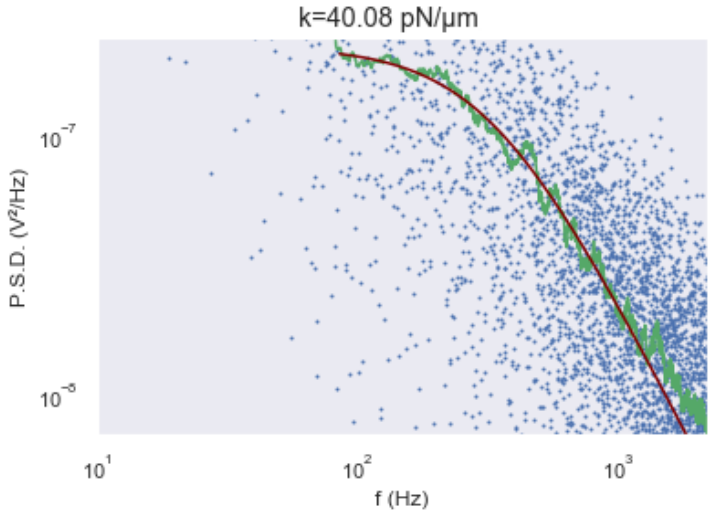

Figure 25: Example graph of the signal from an immobile 2 µm trapped bead in Fourier space in blue, moving average in green and fit using the model described above, yielding a 40.08 pN/µm stiffness.

c) QPD response calibration

Once the stiffness of the trap has been established, one must quantify the QPD response as the bead is displaced from the trap. This can usually be done by scanning the trap across a bead stuck on the surface, recording the resulting wave-like signal that can be extrapolated to apply to all the beads in the sample. The centre region of this pattern can be approximated with a linear function, resulting in a quantification of the sensitivity (in nm/V) of the device. By multiplying the outputted voltage by the sensitivity then by the stiffness, one obtains the force effected on the bead. A slight drift in the height of the condenser lens will affect the sensitivity, as well as a change in trapped bead size or composition (magnetite distribution). This technique is only valid if the back-focal plane (BFP) of the condenser lens is imaged on the QPD.

Using the equations noted in the previous section could allow one to obtain a µm/V response rate value, but this would only be valid for very small deviation from the centre of the trap. Since the metallic suspension in the beads prevent us from using classic levels of trapping laser power, we must rely on a weaker trap for which inducing and measuring sub-100 pN forces will require a significant bead deflection.

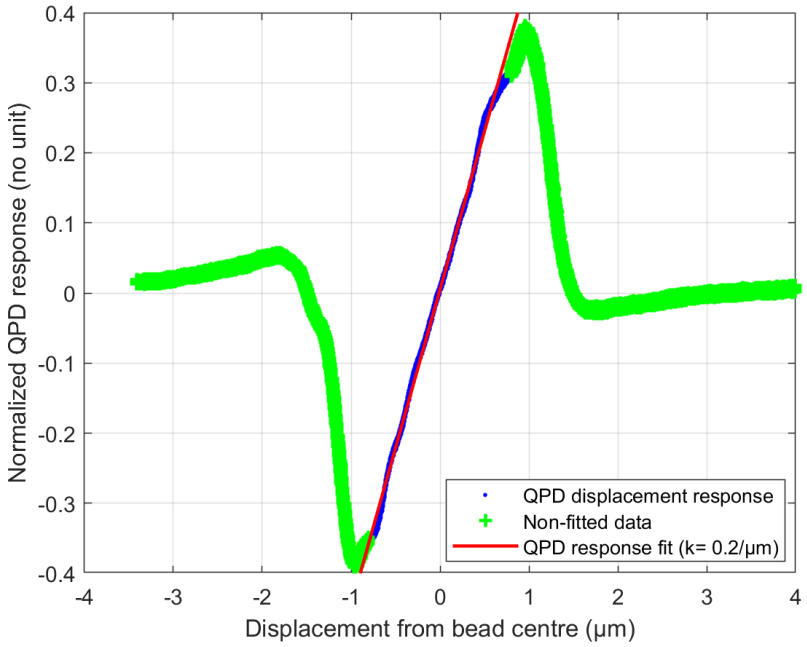

Figure 26: Graph of the normalized detected signal from the QPD when scanning the optical trap across a surface immobilized 1 µm bead, with the system calibrated for proper BFP detection.

In the case of our relatively large 3 µm beads (compared to the typically used 1 µm diameter beads), this technique unfortunately does not work well. Indeed, if the system is correctly aligned so that a 1 µm bead produces the expected pattern (see Fig. 26), a 3 µm bead will lead to a very different pattern, formed by several sine-like waves instead of one. This is due to the fact that the condenser lens is limited in size and thus numerical aperture, which limits the amount of light that can be collected. Empirical changes were made to the system to allow the production of a single wave pattern with an approximately linear central region. This was done by moving the condenser upwards, resulting in a collimated beam of light being outputted from the condenser lens, and using a shorter focal length lens to focus the parallel bead on the QPD.

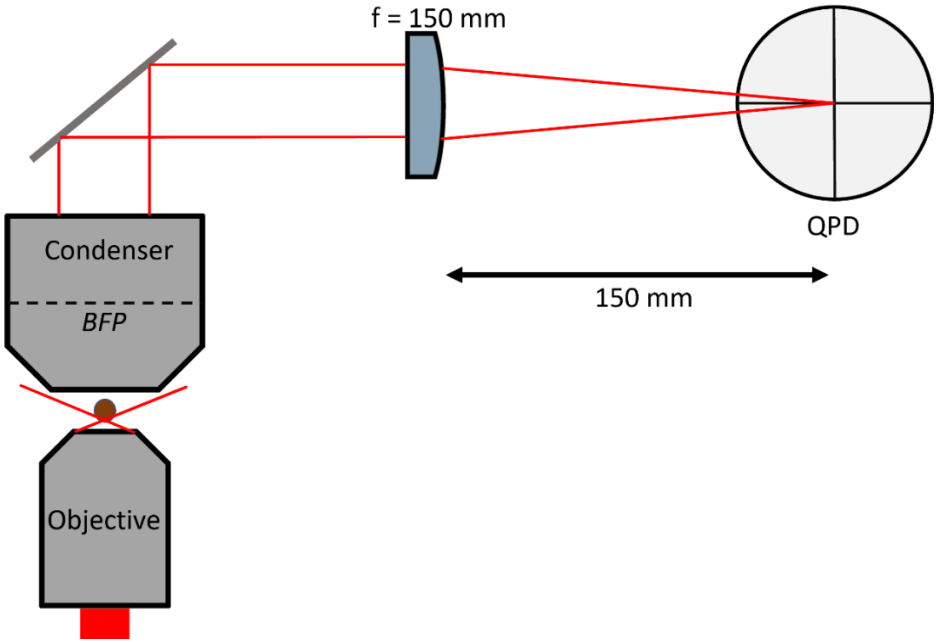

Figure 27: Optical schematic of the QPD force spectroscopy system. The beam enters the back of the objective, overfiling it, is concentrated into a diffraction-limited spot located under the trapped bead, the condenser collects a fraction of the trap light, collimating it. The beam is then focused onto the QPD, like an imaging lens would on a camera.

This solution, even if inelegant, seemed to produce satisfying results, but it was soon found that the vertical amplitude of the wave-like pattern would be considerably smaller than the typical amplitude of the signal produced during a tethering experiment, despite exploring a much wider range of bead deflections. This lead to an inaccurate deflection detection at odds with what we know about this sort of experiment in terms of maximal deflection of the beads out of the centre of the trap while remaining trapped. A considerable amount of effort was put in diagnosing this issue, from carefully controlling the collimation of the expanded beam to exploring a wide range of possible condenser lens and QPD positions and lenses, with no success. Therefore, a new calibration method needed to be devised that would remain consistent with the tethering experiments results.

The decision was thus taken to attempt to calibrate the bead response in a configuration much closer to the actual tethering experiment (trapped bead in solution, a few microns above the surface). It was thus decided that a calibration of the instrument response would be carried out for each and every bead involved in a tethering experiment. This can obviously not be done while attached to the glass surface, since attachment is usually permanent, and the height of the experiment doesn't match. Therefore, one can wait until a trapped bead is tethered to an anchor bead, starting with the trapped bead close enough to the anchor so that no meaningful force is applied by the DNA, and the bead deflection from the trap is thus nil. The QPD signal is then recorded, along with a video of the trapped bead, and the nanostage is moved in small increments of a few hundred nanometres, keeping each position for around a second. This results in a progressive displacement of the bead as the tether is stretched further and further, and an accompanying QPD signal in the

relevant channel, while the other channel representing a perpendicular force is monitored to make sure that it stays constant, which indicated a negligible tether angle relative to the stage movement. The video is then processed, tracking the trapped bead to quantify its movement. A relationship can then be drawn between displacement and QPD signal and fitted with a polynomial function to account for the diversity in response curves. While accurately measuring the size of a bead from an image is difficult and prone to errors, accurately measuring its centre position isn't, as long as it is kept in focus.

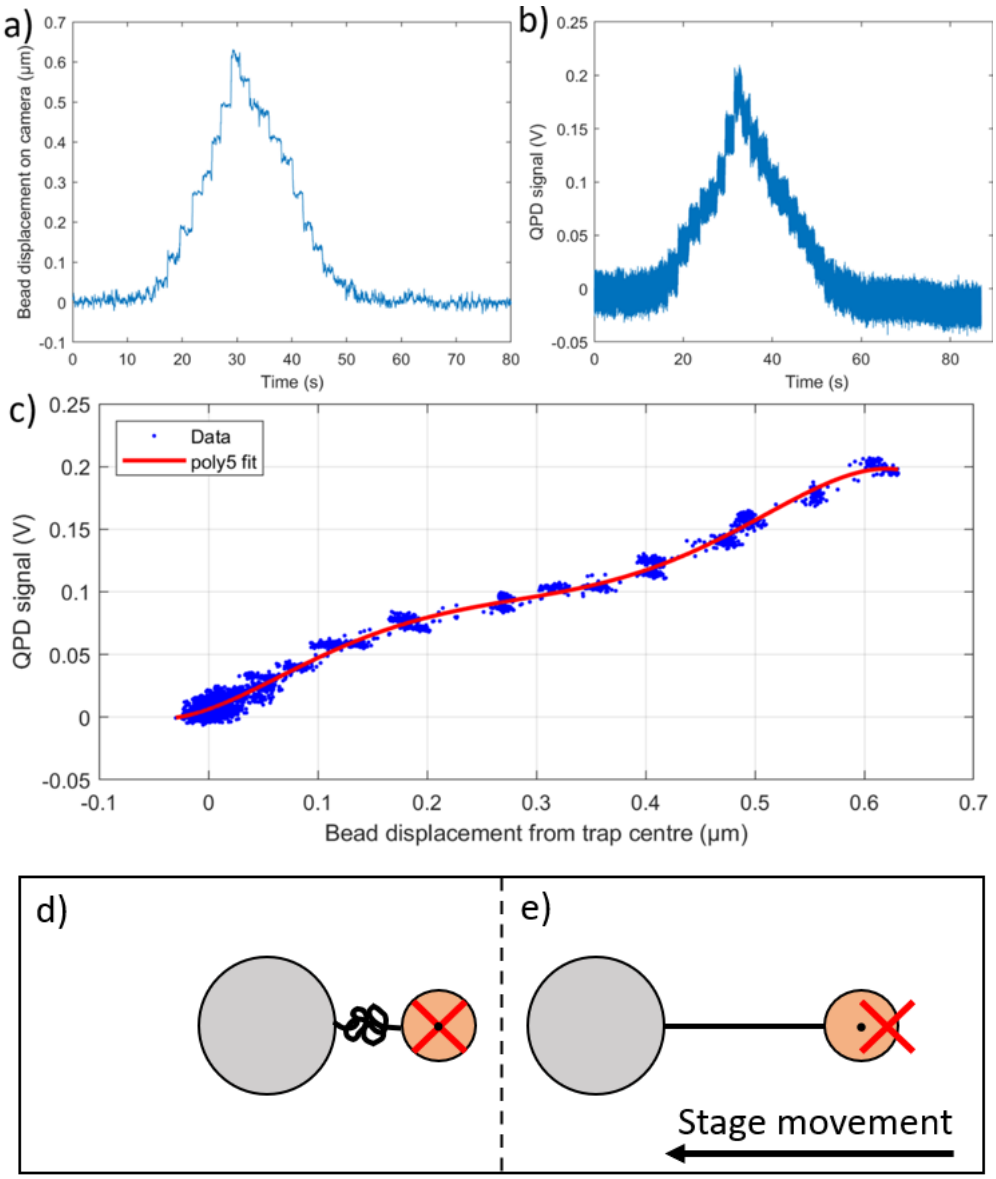

Figure 28: Graphs of the data used to calibrate the QPD response for every bead. a) Graph of the detected displacement of the bead over time. b) Graph of the detected QPD signal over time c) Resulting graph of the QPD signal as a function of the bead displacement. d) Schematic of the beginning of the stretch cycle: The trapped bead in orange is allowed to remain centred with the trap, allowed by the low DNA extension. e) Schematic of the end of the stretch cycle: moving the stage

displaced the grey anchor bead, extending the DNA and pulling on the trapped bead, causing a displacement. This displacement is measured in brightfield and linked to the corresponding QPD signal.

If the mismatch between surface attached bead QPD response and trapped and tethered bead QPD response did not exist, the surface calibration method would be preferably used, even if it is slightly less relevant. This is because only half of the force response curve can be explored with the stepwise stretching method. This is due to the impossibility of pushing the bead in the other direction without colliding with the anchor bead and considerably impacting the measurement. This is not really an issue since only an event leading to a sudden and considerable increase in DNA persistence length would cause this, up to a value on the same order as the contour length of the DNA tether. Such a phenomenon has never been observed nor theorized, so as long as the ellipticity of the QPD signal is symmetrical around each axis, it can be concluded that the QPD response for small deflections due to Brownian noise will be symmetrical.

VIII.3 Magnetic Tweezing

As briefly mentioned in the introduction, Magnetic tweezers systems allow the production of torque and/or tension on a paramagnetic particle. This section will describe a rather original method based around the use of electromagnetic Helmholtz coils to generate a magnetic field, as opposed to the more classic use of permanent magnets. This technique provides the user with the ability to produce a highly homogeneous magnetic field (compared to the typical experiment dimensions), to avoid producing any meaningful tension on the optically and magnetically trapped particle.

VIII.2.i Fundamentals

The two pairs of Helmholtz coils are mounted perpendicularly to each other, each pair producing a component of the final torque applied to the magnetic beads inside the tunnel slide sample. Let us focus on one element of this system, a single Helmholtz coil. According to the Biot-Savart law, the magnetic field $\vec{B}$ produced by a single wire loop in a defined position r in space follows the relationship:

$$\overrightarrow{B(r)} = \frac{\mu_0}{4\pi} \oint \frac{IdL.\overrightarrow{r'}}{|\overrightarrow{r'}|^3}$$

(39)

Where μ_0 is the vacuum permeability, dL a wire element, I the current in the coil and r' the distance from the wire loop.

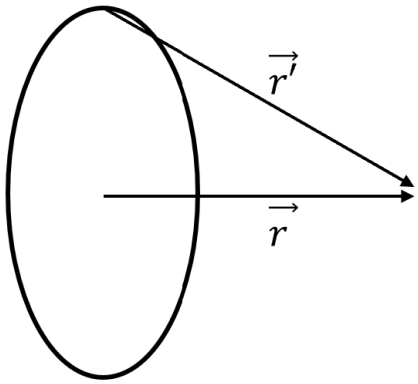

Figure 29: Model of an ideal Helmholtz coil.

$$\overrightarrow{B(r)} = \frac{\mu_0 IR}{4\pi|\overrightarrow{r'}|^3}\oint dL \quad (40)$$

If we choose $|\vec{r}| = y$, then $\left|\overrightarrow{r'}\right| = \sqrt{(R^2 + y^2)}$, so

$$\overrightarrow{B(r)} = \frac{\mu_0 IR}{4\pi(R^2 + y^2)^{\frac{3}{2}}} 2\pi R \quad (41)$$

$$\overrightarrow{B(r)} = \frac{\mu_0 IR^2}{2(R^2 + y^2)^{\frac{3}{2}}} \quad (42)$$

Therefore, for a coil containing N loops,

$$\overrightarrow{B(r)} = N\frac{\mu_0 IR^2}{2(R^2 + y^2)^{\frac{3}{2}}} \quad (43)$$

Simulations made in the past by Dr Z. Zhou proved the dual coil pair system to provide a homogeneous field with less than 1% variation over a volume greater than 4 mm^2, which is well beyond the 1225 µm² field of view (35 µm side square) accessible with this system. This results in a lack of pulling force from the coil system, since

$$\vec{F} = \nabla(\vec{m}.\vec{B})$$

(44)

Where $\vec{F}$ is the force experienced by the bead and $\vec{m}$ is the bead's magnetic moment.

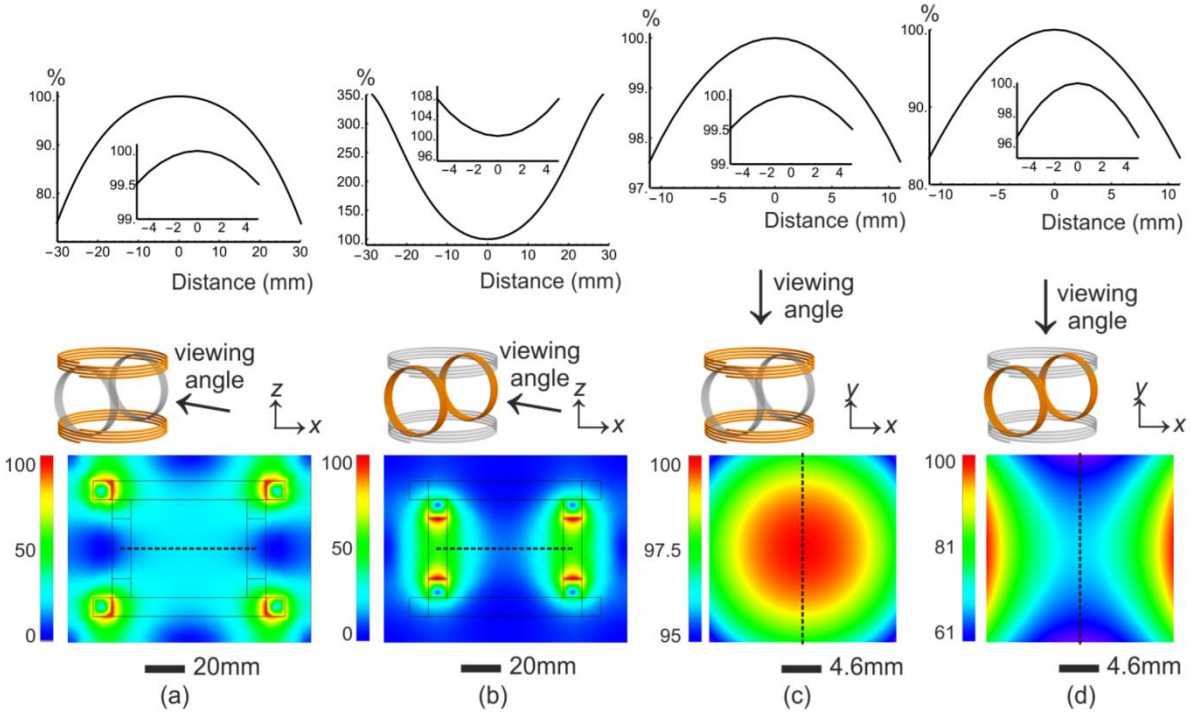

Figure 30: Modelization of the spatial distribution of the magnetic field produced by each Helmoltz coil pair from two angles. This shows a minimal gradient 100 µm from the centre, imaged by the objective. Modelization and data visualization by Dr. Zhou.

The coil mount is also decoupled from the stage, so this homogeneity should be preserved when moving the sample, as long as it is smaller than 2 mm which is well beyond the channel thickness of 150 µm and trapping depth ability of the objective which doesn't exceed 20 µm. Dr. Zhou also calculated the stiffness of the tweezers to be 3500 pN.nm.rad^{-1} with a 4.8 mT local magnetic field and a 3 µm magnetic bead. This value being several orders of magnitude above DNA's torsional stiffness[123], we can assume that unless supercoiled to a level much beyond biological supercoiling ($\sigma < 1.2$), a supercoiled DNA molecule will not be able to effect meaningful torque on the bead. This prevents the device from being able to measure supercoiling-induced torque in its current configuration. By attaching a small sub-micrometric particle on the trapped bead, torque measurement could theoretically be done, but one should be careful about accounting the possible effect of this added anisotropy to the trapped object. this could result in the perturbation of the trapped particle for example,

aligning itself so that both main and marker bead are aligned perpendicularly to the surface.

VIII.2.ii Characterization and Control of MT-induced Stage Drift

When the coils are turned on, one can quickly observe a significant drift, typically over several micrometres per minute. This drift was found to be reversible after turning off the current in the coils, which suggests a heat-induced deformation of a component in the system, possibly generated by Eddy currents from magnetic induction. This drift was observed with every metallic component in the system removed, with the exception of the objective, it's holder and the Nanostage. This drift could not be prevented, as lowering the coil current to a value that would not allow a trapped bead to rotate would still produce significant drift.

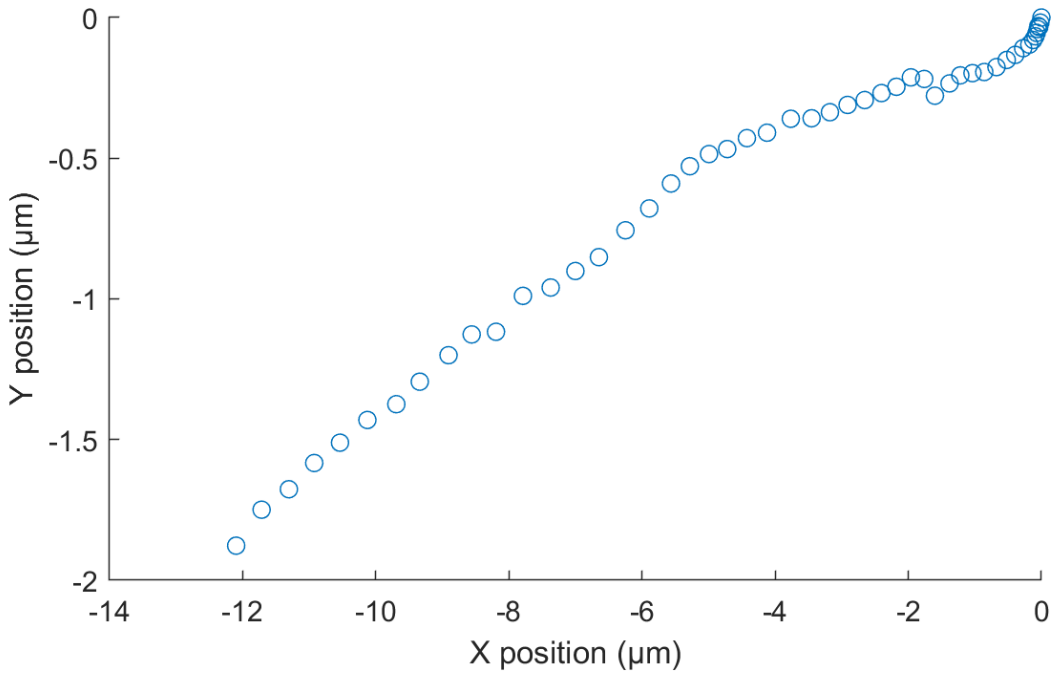

Figure 31: 2-dimensional chart of the position of a surface-immobilised anchor bead when the magnetic tweezers are turned on, for 25 minutes. Each point is 30 seconds apart in time. This shows that unless solved, the device cannot currently switch its magnetic tweezers module on or off during an experiment.

This led us to decide to turn the magnetic tweezers system on more than 30 minutes before the start of an experiment. This provides enough time to the system to equilibrate, and the drift is found to be mitigated entirely. Unfortunately, it prevents the ability to compare the response of a single DNA molecule with and

without magnetic tweezers on, every experiment can either be carried out with the MT on, or off but not both.

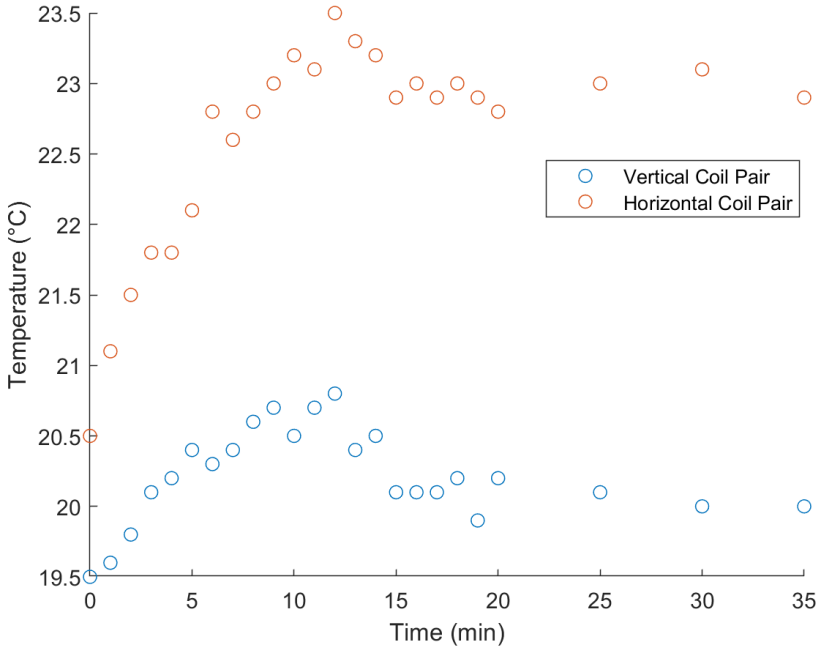

Figure 32: Graph of the measured temperature of the Helmholtz coils over time

This issue could be mitigated depending on the origin of this thermal drift. If it is caused by the coils themselves heating up, then it would in theory be easy to solve, adding a watercooling system by simply wrapping water pipes around it along with a chiller system. If on the other hand the heating is caused by Eddy currents along specific metallic parts on the coils and sample mounts, the issue would be much more complex to solve, requiring testing the metallic makeup of every piece in the system and replacing them accordingly with less responsive materials. This was attempted, removing every metallic part directly around the sample (metal prongs, sample holder screws, etc…) with no effect on the drift. This suggests that either the source of this drift is a structural component in the system that cannot be removed, or it is simply due to the Helmholtz coils radiating heat and creating thermal gradients within the sample itself and its surroundings.

VIII.2.iii MT Performance and Influence of the OT on Bead Rotation

Watching a video of a trapped magnetic bead under the influence of the magnetic tweezers can be misleading. The relatively high sphericity of the beads can lead one to believe that a bead in spinning when it is really rocking. Additionally, even if the spinning movement is somewhat clear, a common optical illusion caused by the 2D projection on a screen of a 3D objects leads to the impossibility to tell in which direction the object is really spinning. This creates the need for camera-decoupled methods to confirm that the magnetic tweezers are functioning correctly.

The simplest sanity-check one can do to check that the coils are functioning properly is to remove the objective and suspend a standard compass where the sample should be, facing the operator. One can then easily confirm that there is indeed a rotating magnetic moment and confirm what its direction is. This however does not confirm that a trapped bead is really spinning. In order to do that, one must make use of the trap back-focal plane detection system. If the bead is spinning, displaying the QPD signal from a spinning bead in the Fourier space will lead to the detection of large peaks around the inputted MT signal frequency, as well as around its harmonics.

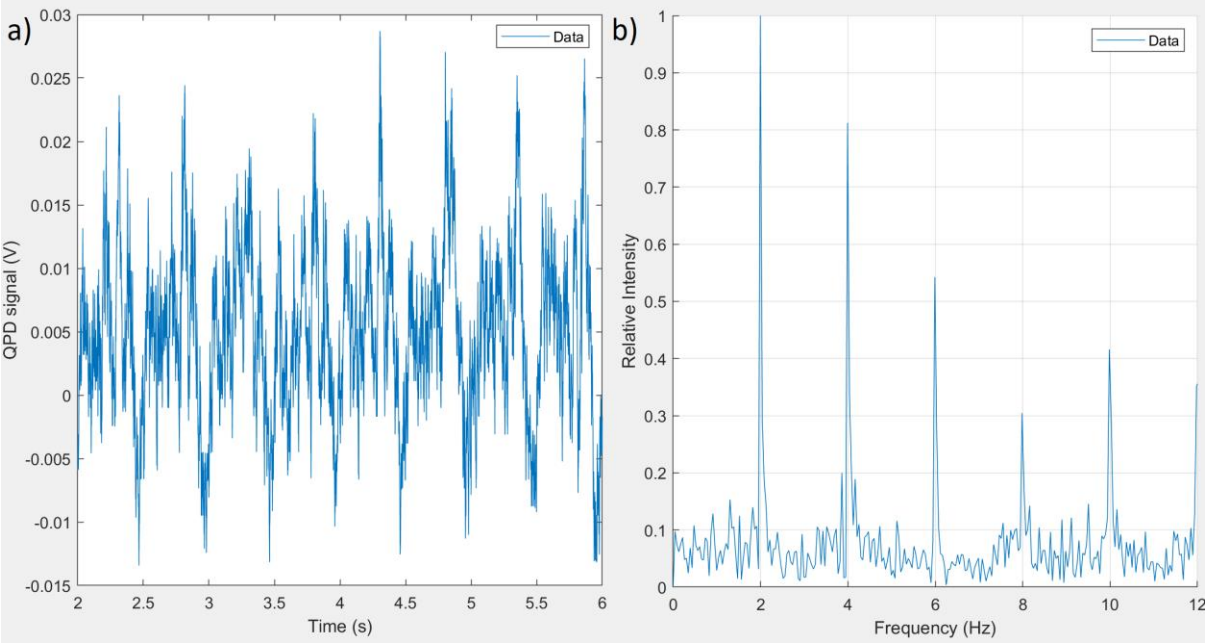

Figure 33: QPD signal of a spinning bead at 2Hz. a) Signal across time, showing 8 repeated patterns in 2 s. b) Same data but displayed in Fourier space, showing a main peak at 2 Hz and its harmonics at higher frequencies.

These measurements lead to the appearance of an interesting effect. At high trapping laser power, it was found that the trapped beads would not rotate as well as with low trapping power. This lead to the hypothesis that the magnetite infusing the bead could influence the bead trapping, producing an imperfect static optical torque trap. This suggests that the use of lower trapping powers might be preferable to

ensure that the effective applied number of rotation matches the theoretical number. This will unfortunately decrease the stiffness of the trap and thus the maximum stretching forces that can be applied.

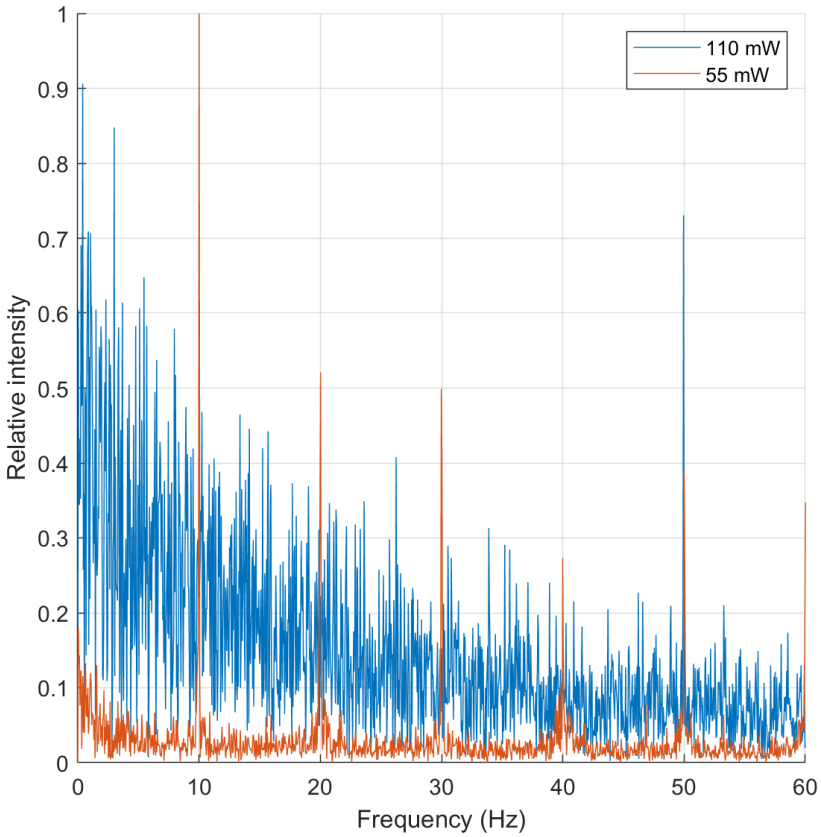

Figure 34: Graph in Fourier space of the signal resulting from the same bead spinning at 10 Hz, with 110 mW of trapping power in blue, 55 mW in red.

The maximum spinning rate was also explored, and found to be 20 and 50 Hz, after which the frequency graph becomes significantly noisier and presents peaks at lower frequencies than the MT oscillation, a possible consequence of the competition between the torque induced by the magnetic tweezers and the hydrodynamic friction from the surrounding fluid.

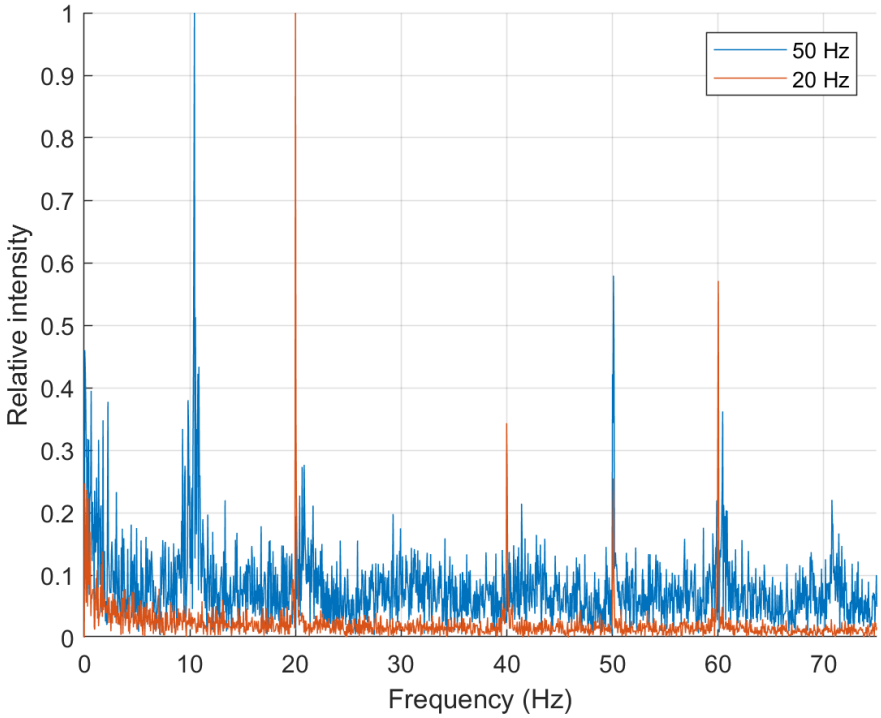

Figure 35: Graph in Fourier space of the signal from the same spinning bead, at 20 Hz in red and 50 Hz in blue.

VIII.4 DNA Tether Synthesis

This work was carried out along with and under the direction of Dr. Jamieson Howard. The end-goal of the work described in this section is to obtain a solution of double-stranded DNA containing a central section of defined length, roughly 15000 base pairs (bp) in length, with each end functionalized on both strands with multiple moieties able to bind to one of the two beads used in the experiment. One end will be functionalized with DIG (Digoxigenin) moieties, the other with biotin moieties (each end being called a “handle”).

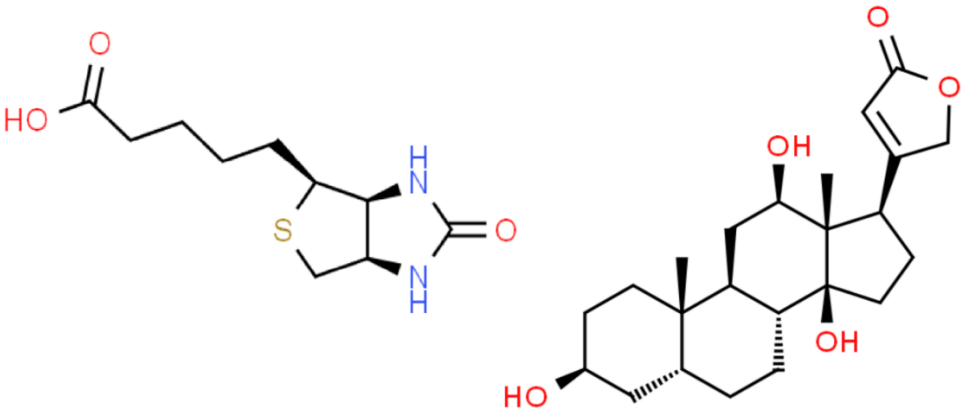

Figure 36: Chemical structures of Biotin on the left and Digoxigenin on the right, from Chemspider.com

The multiple attachment points on each end are designed to permit control over the topology of the molecule, as it would freely rotate around a single molecular bond if any of the two ends was attached to a bead by a single moiety. It is also important to accurately control the sequence of the centre part, which can be expensive, difficult or outright impossible to do with some DNA synthesis techniques. This is why the approach chosen relies on obtaining this segment by selectively cutting a widely available and carefully controlled DNA molecule, originating from a lambda bacteriophage virus plasmid. The centre part of the tether was obtained from a Lambda phage plasmid supplied by New England Biolabs (NEB), and cleaved with the restriction enzymes NgoMIV and NheI-HF, yielding a 14639 bp product of interest along with two 20040 and 13823 bp fragments. This mix was ethanol precipitated and resuspended in 10mM Tris at pH 8.0.

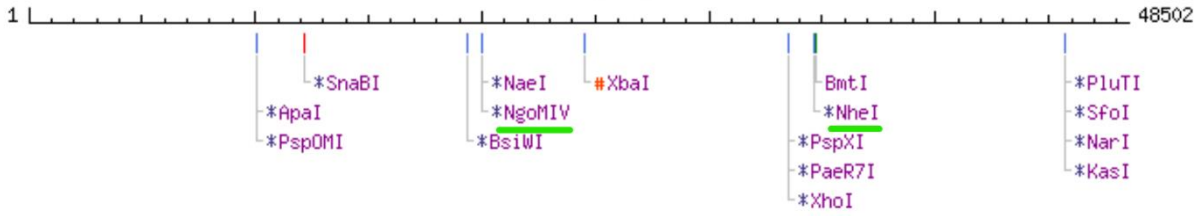

Figure 37: Map of some of the restriction sites present on the lamb template, with the two relevant ones underlined in green. From NEB cutter (nc2.neb.com)

The handles were produced by amplifying a 498 bp long fragment of the pBS(K+) plasmid by PCR reaction, with a fraction of the Thymine nucleotide mix being replaced by either biotin-16-dUTP (desoxyriboUridine TriPhosphate) in a 1 to 1 molar ratio or digoxigenin-11-dUTP in a 6.5 to 1 molar ratio, assuming a lowered incorporation efficiency compared to normal dTTP nucleotides which will be shown below. The product of those reactions should be two 515 bp double-stranded handles, with either 120 biotins or 32 digoxigenins. Those reactions were monitored by gel electrophoresis and the handle products were purified using a Qiaquick PCR purification kit from NEB. These purified products were then digested with

NgoMIV (biotinylated handle) or NheI-HF (digoxigenin handle) before being purified again through a Qiaquick purification kit. This last digestion was done to create “sticky ends”, complementary with the cut lambda fragment.

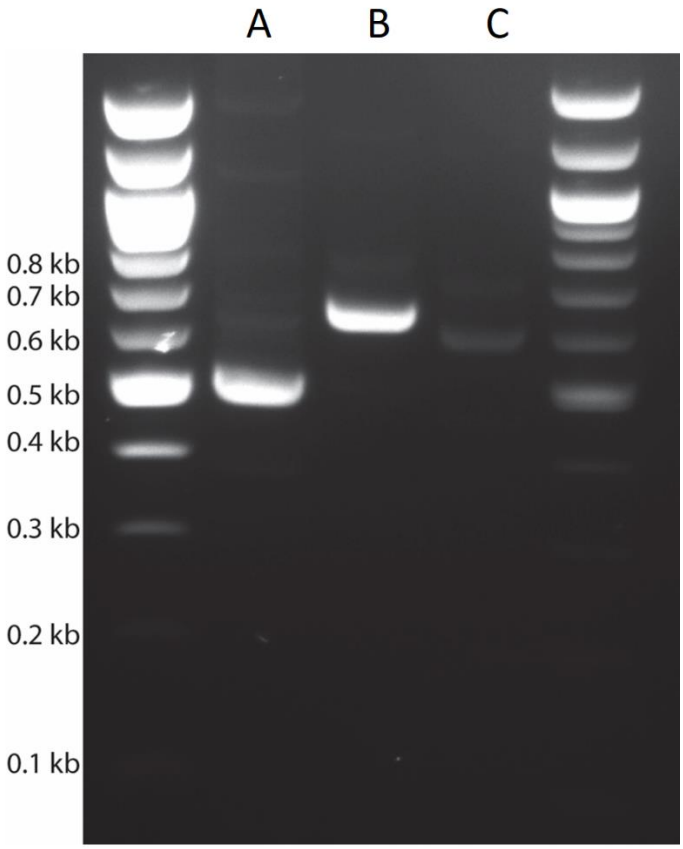

Figure 38: Gel electrophoresis image of the result of a handle production test run. Lane A is the nonfunctionalized handle, line B is the biotinylated handle and line C the digoxigeninated handle. The functionnalized handles appear to be longer than they are due to the mass added from the multiple biotins and digs they carry. The efficiency of the digoxigeninated handle PCR is notably lower than the biotinylated handle which appears to be relatively comparable in terms of quantity to the unfunctionalized handle.

The three resulting products (handles and cut lambda) were then mixed and ligated using T4 ligase from NEB. The resulting product was then ran through an agarose gel using electrophoresis and the appropriate band was cut out, dissolved and purified with a large molecular weight agarose gel Qiaquick extraction kit (Quiagen). The reason for this last step was the inevitable ligation of the handles on the several unwanted lambda digestion products, some semi-labelled with a single handle, some multiple times the intended length. The resulting product was a 15.7 kbp molecules, functionalised at both ends with several dozens of digoxigenin or biotin moieties.

VIII.5 Fluorescence microscopy and choice of DNA-binding dye

Many single-molecule fluorescence microscopes use advanced techniques to increase detection accuracy, for example with TIRF microscopy by lowering background intensity[124], or PALM/STORM to resolve objects closer to each other than the maximum resolution criterion. Since detecting DNA is really about detecting a large amount of DNA-binding fluorescent organic dyes localized between base pairs, there is no need to maximize their signal to be able to observe them for long periods of 30 seconds or more. This section will explain the way the epifluorescence imaging is carried out.

VIII.5.i Fluorescence microscopy

The fluorescence excitation beam is outputted by a rather nonconventional laser, a Fianium SC-400. This device outputs a broad spectrum of laser wavelengths, from near-UV to Infrared, with most of the spectral density being localized in the latter part of the spectrum, for a total available power of 4 W. This enables us to select and tune the excitation light to better match the excitation spectra of the observed molecules, instead of potentially having to buy new lasers or use poorly matching ones in case of change of dye.

The beam is first filtered by a Hot Mirror, reflecting most of the Infrared light. It is then split into two components by a dichroic mirror transmitting wavelengths above 550 nm, reflecting light under that value. Each beam passes then through 2 gradient filters mounted on vertical translation mounts. One is a Short Pass filter, the other Long Pass. This allows us to finely tune the spectrum to fit SYBR Gold's.

The beams are then recombined using a second dichroic mirror with opposite properties to the first. They are then expanded by a telescope (50 mm to 300 mm, 6X expansion), the downstream lens being placed on a perpendicular translation stage for oblique illumination. Oblique illumination is made possible as this lens is its own focal distance away (300 mm) from another, which is then its own focal distance away from the objective. The resulting beam coming out in the sample is thus collimated and its angle of incidence can be changed by moving the translation stage mounted lens for TIRF or HILO illumination.

VIII.5.ii Choice of dye

SYBR Gold is the chosen fluorescent DNA intercalator for all of our experiments. It had previously been extensively used for gel staining[125] but has been recently proving to be a dye with very interesting performance for single-molecule DNA imaging. It is exceptionally bright ($\varphi = 0.6$ when bound to DNA) and presents much reduced levels of nonspecific binding to the surface and bead than the previously used YOYO-1 dye. Its structure was kept a trade secret for more than two decades until recent work by Kolbeck et. al determined its structure using high-

performance NMR spectroscopy[126]. Its effects on DNA was investigated in detail in the same work using magnetic tweezers-based techniques, such as contour and persistence length extension and twist reduction, all a consequence of its intercalative major groove-binding mode. SYBR Gold is used at a nominal concentration of 1 µM, a 1 in 10000 dilution, and is kept dissolved in DMSO in 1 µL aliquots and refrigerated at -20 °C.

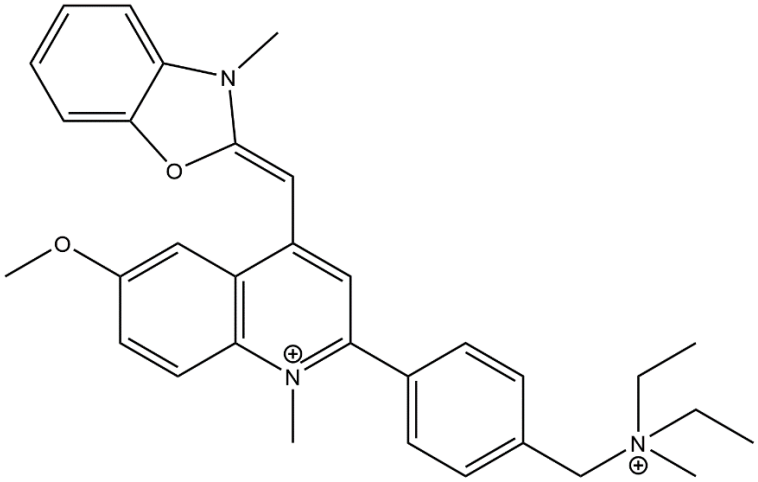

Figure 39: Molecular structure of SYBR Gold, as determined by Kolbeck et. al. [124].

IX. Technical Development

A considerable share of this project was spent controlling, recalibrating and improving various elements of the device as well as of the sample itself. While the setup was technically working (DNA tethering, force transduction, magnetic tweezing…), it suffered from a low performance in several key areas. Tension produced by the optical trap was only able to effect forces below 2 pN which severely limited the accuracy of persistence lengths computed from force extension curves. The fluorescence imaging allowed the detection of a tether but only with high levels of noise and for a few tenths of a second before its destruction. Finally, the control software was missing a few features such as manual nanostage control and accurate Magnetic Tweezers control. These areas were deemed critical for the success of the project and for the future use of the microscope. This chapter will attempt to describe the measures taken to improve the setup performance in several key areas.

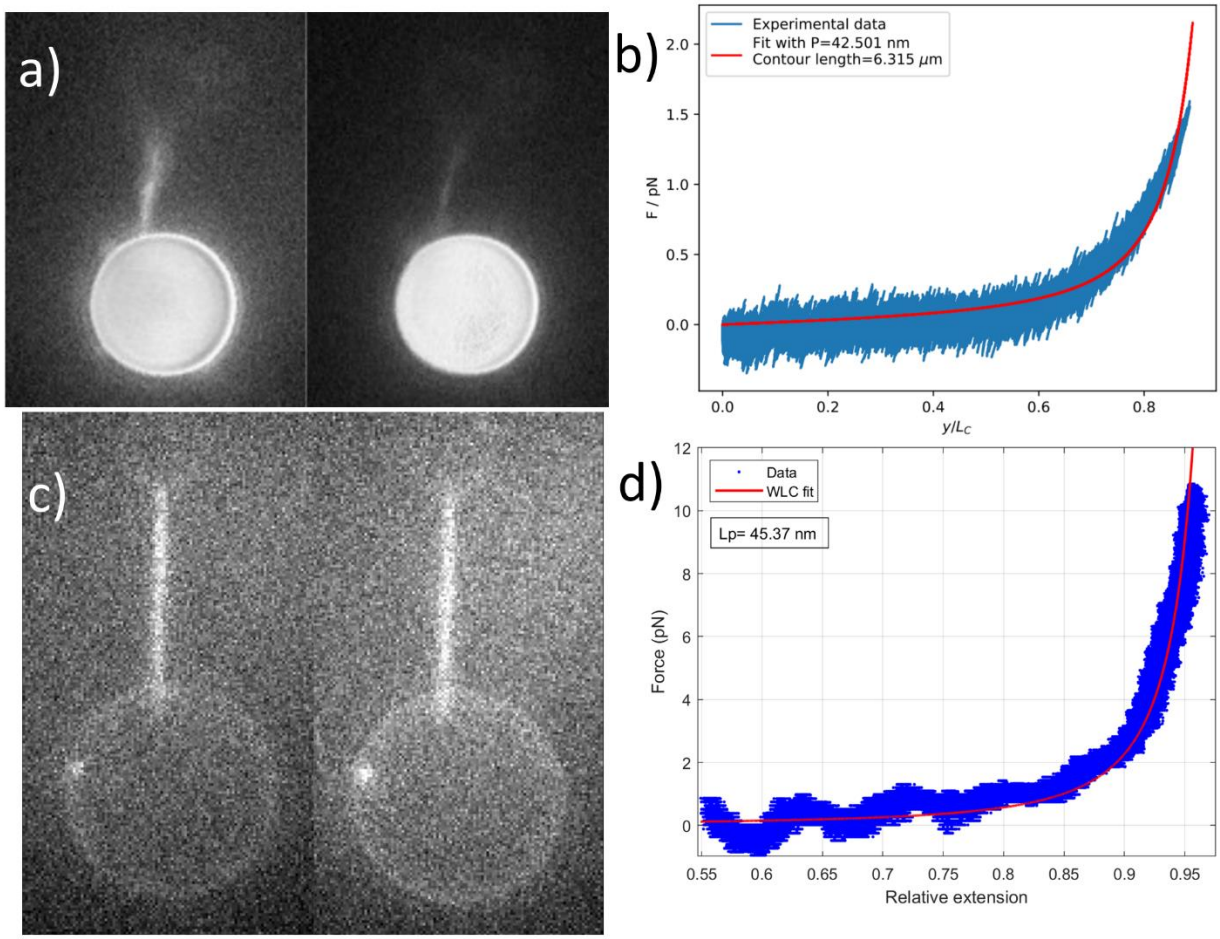

Figure 40: Comparison of the assay performance before and after this project. a) DNA tether pictures acquired by Dr. Zhou, the tether is somewhat visible but becomes dim quickly, then breaks after 250 ms. b) WLC-fitted force-extension data obtained by Dr. Shepherd, showing the optical trap then-low stiffness. c) Fluorescence images of a DNA tether obtained after several improvements, the tether is clearly visible and stays so for more than 30 seconds, allowing the acquisition of force-extension data while under illumination, without ROS scavenger. d) Fitted force-extension data showing a much-

improved ability to exert forces. The periodic oscillations at low extension are caused by spurious signal caused by the beads proximity.

IX.1 Microscope Design

IX.1.i Hardware

The improvements carried out on the optical setup itself were centred around three goals: decouple fluorescence and trapping beams, improve the fluorescence detection of and overall control on the DNA tethers and conserve the ability of the setup to do oblique illumination.

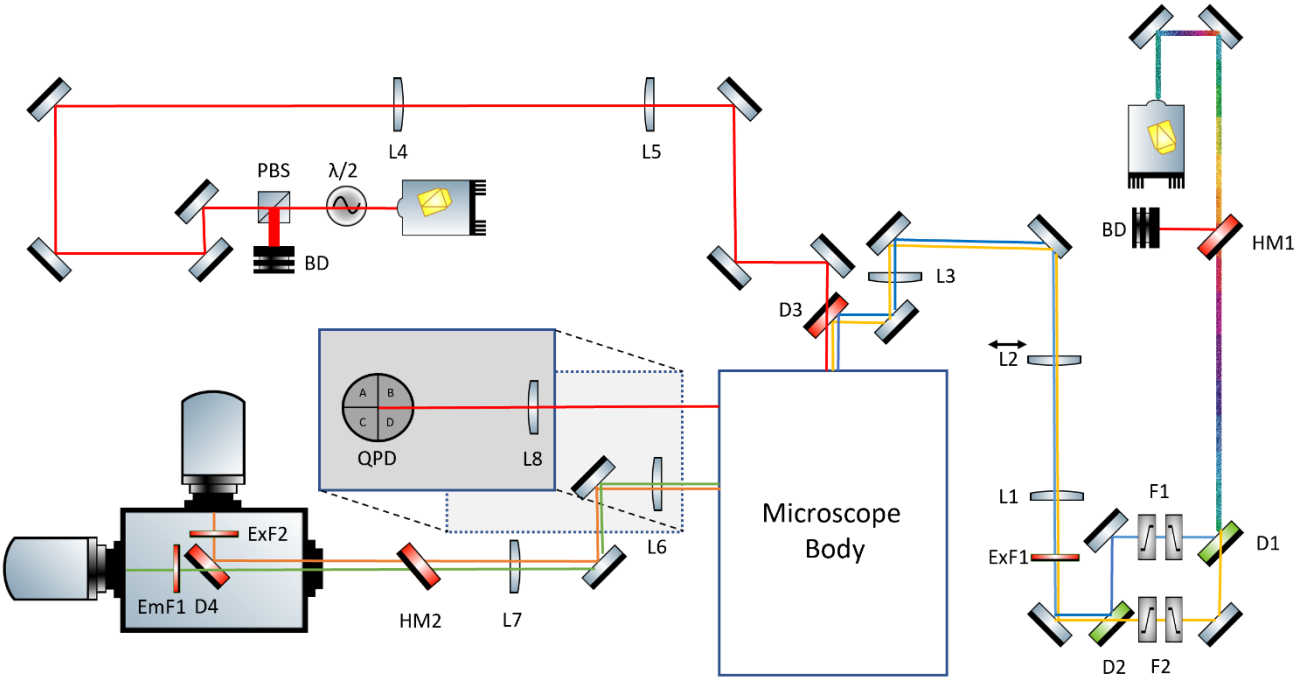

Figure 41:F To-scale schematic of the final microscope optical layout. L= lens, D=dichroic mirror, F= gradient filter, em/exF= emission/excitation filter, BD= beam dump, HM= hot mirror λ/2= half-wave plate, PBS= polarization beam-splitter

a) Decoupling the trap and fluorescence excitation paths

In its original form, the optical trap suffered from an important drawback. A lens was present near the back-port of the microscope body, conjugated with the objective back-aperture. This was originally done when the microscope was fitted for TIRF microscopy, its role being to deflect the fluorescence excitation beam with the critical angle needed to achieve Total Internal reflection. Because of this, the fluorescence excitation and optical trap beams had to be combined upstream of this lens, and so any steering of the infrared beam would result in hitting the lens at an

angle, reducing the stiffness of the trap. Since the tethering surface experiment was located at least 2 µm away from the surface, TIRF illumination was impossible to carry out as the evanescent wave can only penetrate a few hundreds of nanometres from the surface at best. Additionally, if a user decided to use the microscope for TIRF experiments (irrespectively of optical trapping), the adjustments to the TIRF lens positions occasionally needed to realign the beam would have drastic effects on the optical trap.

The decision was thus taken to remove this lens and use a longer focal length lens (500 mm) before the two laser beams are combined. As a consequence, the IR beam can now be steered into the objective back-aperture with two mirrors, independently from the visible fluorescence laser beam. The resulting trap stiffness was thus increased by a factor of 10, yielding typical stiffnesses of 20 pN/µm at the usual working powers.

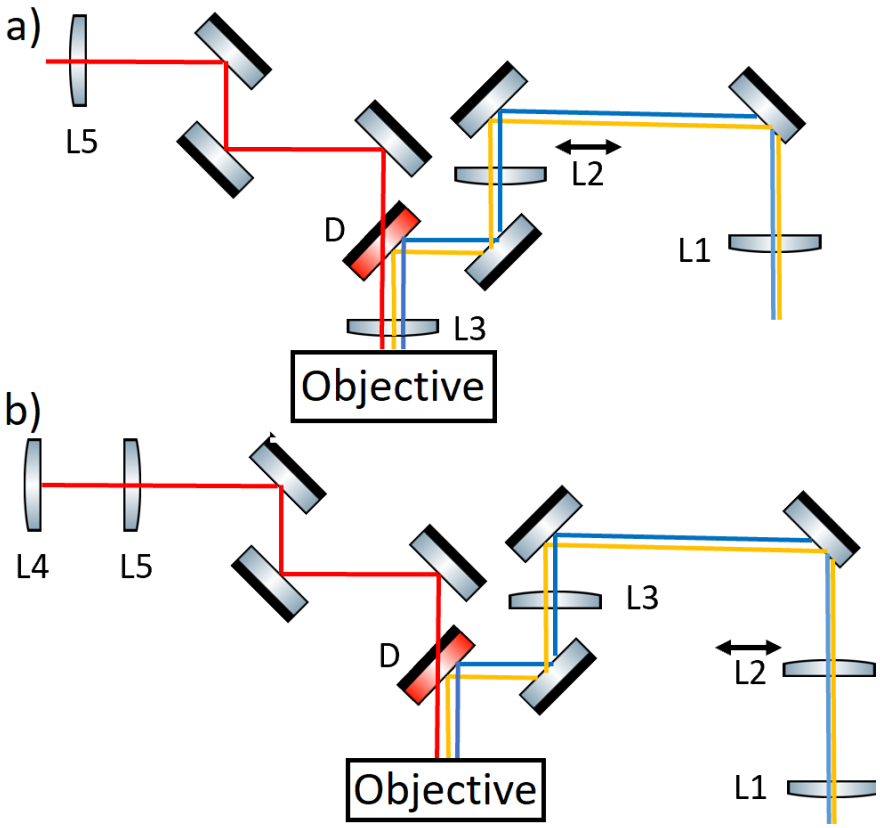

Figure 42: Optical schematics of the beam delivery setups, before (a) and after (b) modification. D stands for dichroic mirror, L for Lens, the double headed arrow indicates mounting on a translation stage. a) The previous design had IR beam expansion and fluorescence beam focusing done by a single lens, L3. L1 and L2 would expand the fluorescence beam, with L2 being able to angle it for TIRF. b) The new design has IR and fluorescence beams entirely decoupled. L4 and L5 expand the IR beam, L1 and L2 expand the fluorescence beam with L2 being used for TIRF as it is conjugate with L3, L3 focuses the fluorescence beam onto the objective back-aperture for a collimated outputted beam.

Additionally, the setup was then able to trap a wide range of particles sizes, down to 500 nm up to 15 µm, when in the past 3 µm particles were the smallest to be easily trapped.

b) Focus adjustment

The previous method used to adjust the focus to match the plane where a trapped bead was located was to use a "Correction module" mounted on magnetic mounts. While the module was functional, it needed to be finely adjusted every single time, and drastically reduced the field of view to less than 150 µm². A similar effect was produced by mounting one of the lenses in the imaging module (L2) on a translation cage, to permanently shift the focal plane to the one of the trapped bead. This resulted in no loss in the field of view, and a lower distortion of the image. Every bead size requires a different lens displacement, so it is important to recalibrate the camera equivalent pixel size every time that the lens is moved.

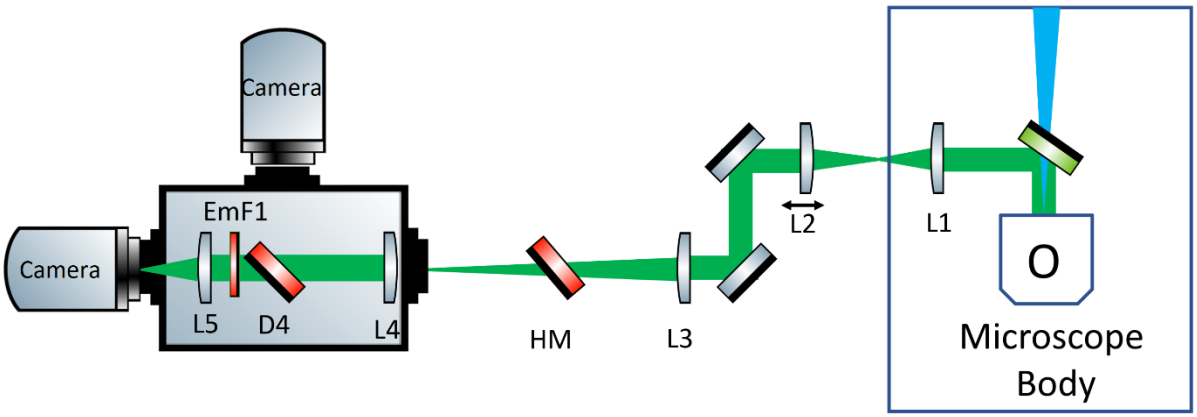

Figure 43: Schematic of the Imaging part of the optical setup. The fluorescence excitation beam comes focused onto the back-aperture of the objective, the fluorescence signal from the sample comes back through it, is reflected by the dichroic mirror and focused by an internal lens onto the side port of the microscope body. This divergent beam is collected by L2 which is mounted on a cage and can translate along the optical axis to change the focal plane. L3 focuses the beam onto the back of the TuCam which contains a simple 1:1 telescope that will thus focus onto the image sensor of the camera. The second colour and camera path is ignored for clarity.

c) New TIRF illumination setup

TIRF illumination is achieved when the fluorescence excitation module is engineered so that the sample sitting on top of a coverslip in a tunnel slide chamber is hit by a fluorescence excitation beam at an angle of incidence below the critical refractive angle. This causes total internal reflection at the glass-water interface, reducing the exposure of the sample to the excitation beam and thus increasing the

SNR of fluorescent molecules on the surface. With a micrometre mount, it is possible to deflect a specific lens laterally to modulate this effect, the angle of incidence decreasing with increasing deflections. One can thus reproduce the critical angle of total reflection, predicted by the Snell-Descartes law, such as:

$$\theta_c = sin^{-1}\frac{n_1}{n_2}$$

(45)

Where n_1 and n_2 the optical indices of glass and water, 1.33 and 1.5 respectively. This predicts a 62.5° angle of incidence to achieve TIRF. To link lateral lens deflection and angle of incidence, one must build a "TIRF stack" formed by a coverslip, several slides with objective oil in between, and graph paper between the last two slides. The stack is placed in the sample holder, and the micrometre is twisted, recording the lens deflections leading to increments of 1 mm deflection on the stack. This allows the determination of the angles of incidence through simple Pythagorean geometry. The necessary lens deflection is identified to be 10.04 mm to achieve a 62.5° angle of incidence. The relatively low number of points in this graph is due to the unoptimized placement of the relevant lenses to achieve TIRF. The decoupling of fluorescence and trapping beams has as a necessary consequence the displacement more upstream of those lenses, which as a consequence implies that the same lens deflection will cause a greater beam angle out of the objective. Nevertheless, TIRF illumination was attempted on a calibration sample made of 80 nm fluorescent beads. The intensity emitted by each bead was summed the summed intensity of an area of the same size without a bead (background) was also summed and subtracted to the bead's, applying an approximate background correction. This was repeated 100 times, and the ratio of background-corrected bead intensity to its nearest background intensity value was calculated, in TIRF and epifluorescence illuminations. This shows a notable increase in bead brightness at equal illumination power in TIRF, confirming that the ability for oblique illumination was conserved.

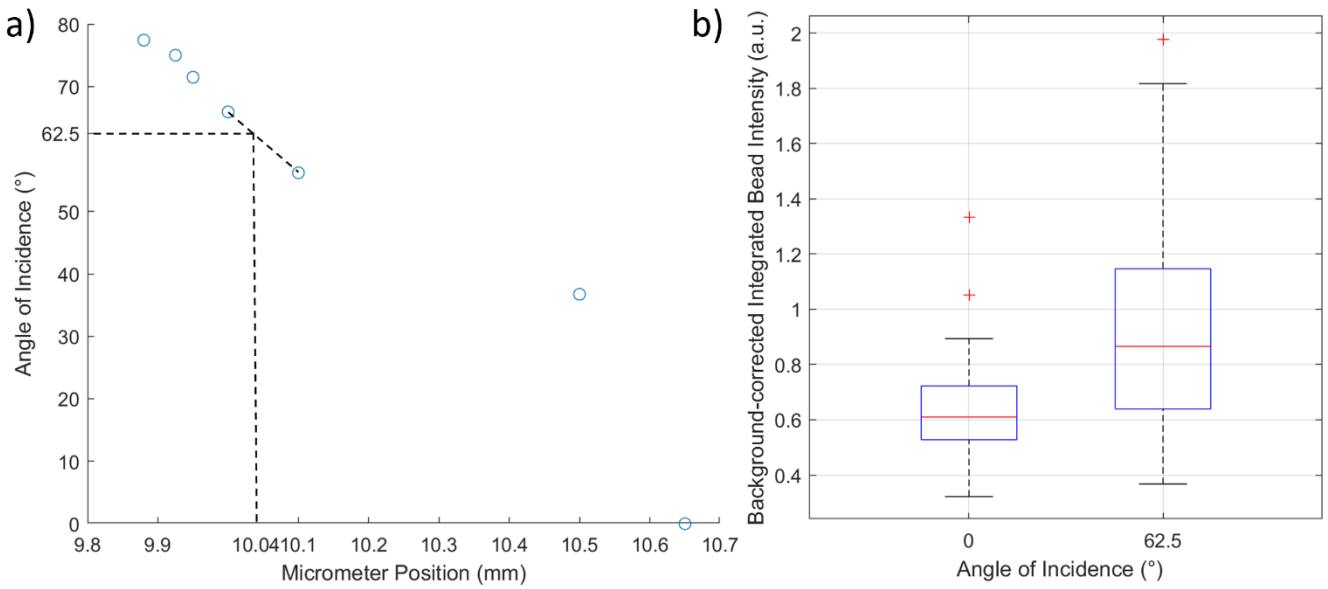

Figure 44: a) Graph of the measured deflection of the fluorescence excitation beam as a function of the TIRF lens micrometer mount position. b) Box plots of the relative background-corrected integrated intensities of 80 nm fluorescent beads attached on the sample surface, in epifluorescence and TIRF illumination modes.

Even if the typical tethering experiments do not allow TIRF illumination due to the molecule of interest being too far off of the surface to be excited by the TIRF evanescent field (around 150 nm), TIRF is not relevant to those experiments. But similar less extreme forms of oblique illuminations such as HiLO can still be applied, which will help improving detection accuracy or reduce the necessary amount of power to excite fluorescent dyes on a DNA molecule.

d) Nanostage recalibration

It was found early on that due to possible earlier damage or miscalibration, there was a linear mismatch between the inputted movement into the nanostage, and its effective movement. This issue was easily solved by using a two dimensional calibration graticule to apply the necessary multiplier to correct the accuracy of the nanostage. The absolute position of the graticule was determined by measuring the line profiles of the graticule lines during their movement. This was on the other hand more difficult to achieve for the third (vertical) axis. To remediate to this, an approximate calibration technique was devised, leveraging the narrow size distribution of the Micromod microspheres. Microspheres of 2, 3 and 10 µm diameter were immobilized on a sample surface, and areas where each of the three possible size beads were present were selected. Since the absolute size (and thus height) of the beads were known, the nanostage was moved up and down so that each bead would be in focus, one after the other. This gave an appropriate estimate of the necessary correction factor, but the impossibility to explore a wide range of heights considerably limited the accuracy of this result. During the last year of the project, the nanostage's controller Z-axis suffered damage that rendered it inert, and the choice was made to not send the device for repair due to the complete dependence of the setup on its presence, as well as the additional delays caused by the pandemic.

IX.1.ii Labview Control Software

The Labview programme controlling the setup (camera control excepted) was improved to meet the demands of its users. The data acquisition subroutine was rebuilt manually to allow for more flexibility in terms of channels and data acquisition rates. The programme was also modified to be able to run Python programmes for in situ stiffness calibration for example.

The Magnetic Tweezers controlling software was also upgraded significantly. When in the past it could only be turned on and off at varying frequencies and amplitude, it is now capable of outputting a fixed number of turns, including the ability to twist at fractions of a turn. It is thus now much easier to apply a series of defined supercoiling densities to a single molecule.

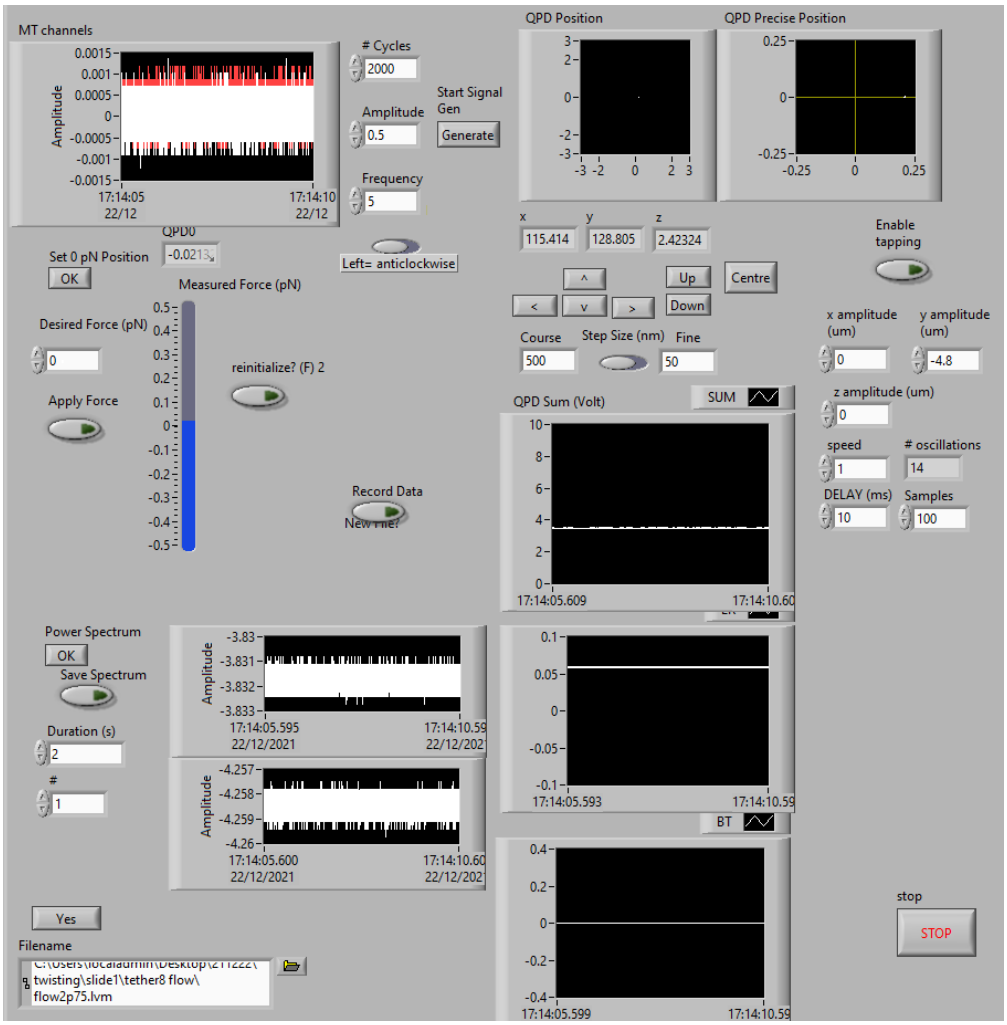

Figure 45: Front panel of the Labview program controlling the microscope. The graph at the top left monitors the voltage across each Helmholtz coil (here 0) while the rest of the interface in this region allows for triggering force clamping. The bottom left half has displays of the nanostage movement (in V) as well as saving settings. The displays in the right part of the GUI monitor the QPD signals in 2D as well as across time.

IX.2 Surface and Bead Chemistry

The surface-dependent aspect of the tethering assay introduces some delicate issues. On one hand, the antiDIG anchor beads need a strong and stable attachment to the surface, able to withstand several flushing steps without detaching, as well as repeated pulling cycles when acquiring force-

extension data. On the other hand, once the 3 µm magnetic beads are introduced in the sample, if their affinity for the surface is too high, the operator only has very limited time to try to create a DNA tether before all the magnetic beads are irreversibly stuck. Once the tether system is assembled, the nonspecific fluorescence from the surface must not be too high, to allow for an easy detection of the DNA.

IX.2.i Surface Chemistry

The previous method of surface attachment of beads was to create a Nitrocellulose layer on the coverslip by dipping it in a 2% solution in amyl nitrate before air drying. This is particularly easy, quick and creates a good surface for attachment but suffers from two issues:

- The surface is hard to passivate, and freely-diffusing 3 µm magnetic beads will quickly get stuck, after around 10 to 15 minutes, even after BSA passivation. This reduces an experiment to one or two tethers formed at best and severely reduces the throughput of the technique.

- DNA-intercalating cyanine dyes used in our assay have a strong affinity with this substrate and result in an overwhelming background noise that prevents clear visualisation of the DNA, without using high laser powers that will quickly destroy it. This prevents the video detection of long processes and reduces the Signal to Noise Ratio of the detected DNA. This is also not mitigated by the use of passivating agents like BSA, the cyanine dyes being considerably smaller and thus still able to access the nitrocellulose covered surface.

To mitigate those issues, a Self-Assembled Monolayer (SAM) of epoxy-terminated silanes was chosen as it was used successfully in previous related work[45]. Silanization has been widely used to prepare surfaces with a high chemical homogeneity[127], with a wide variety of chemical functionalisation, adjusting the physicochemical properties of glass[128] or metal oxide surfaces[129]. Silanization is also a necessary step to construct PEGylated surfaces, currently the gold-standard for reducing nonspecific adsorption of fluorescent probes[130]. PEGylation was not used in this project due to its relatively high preparation time, and its performance in terms of passivation being actually so high that it would require additional steps to couple digoxigenin moieties to allow binding of the anchor beads.

The chosen technique requires a careful cleaning of the glass surfaces before a simple 1-pot functionalisation in a gentle solvent (isopropanol). The resulting surface is both able to fixate protein-labelled beads by covalent linking with available amine-terminated amino-acids, and prevents the nonspecific binding of polar cyanine dyes, resulting in lower levels of fluorescence background noise. This surface was used in previous work to couple a monolayer of Neutravidin proteins to a surface. Once passivated with Bovine Serum Albumin (BSA), the surface allows the use of the sample for extended periods of time, beyond an hour.

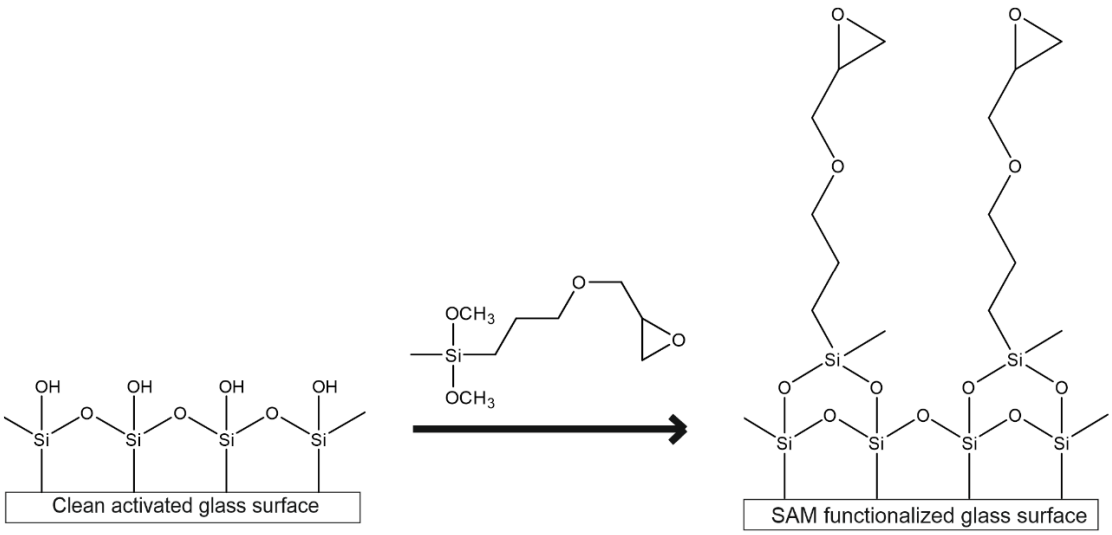

Figure 46: Silanization reaction

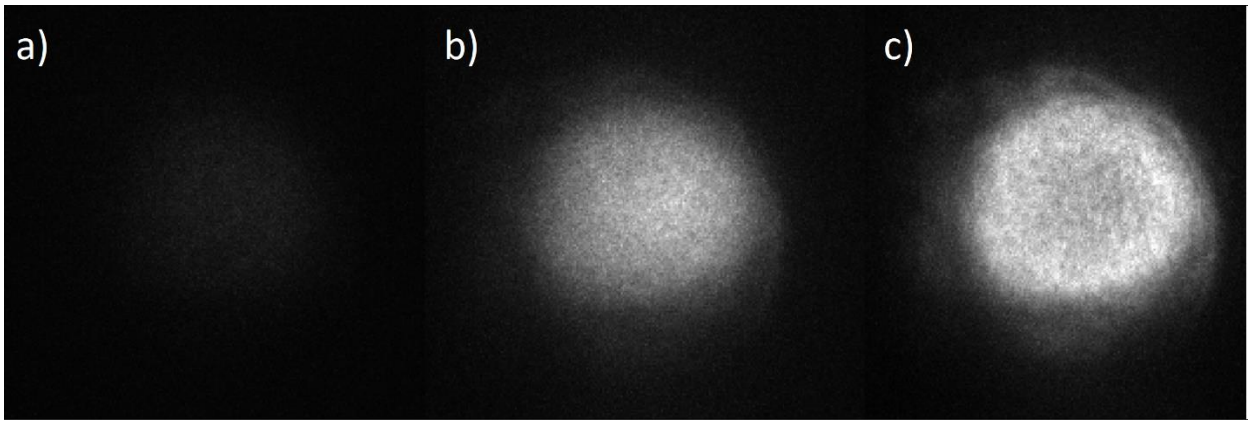

Figure 47: Pictures taken from the sample surface, 10 frames after illumination. a) Plasmacleaned coverslip b) silanized coverslip c) Non cleaned coverslip. This shows that the silanization does cause the background intensity to increase compared to bare glass, but is still a considerable improvement over the Nitrocellulose surface which will overwhelm the camera sensor even at low illumination power (150 µW)

While it is extremely difficult to measure the density and quality of the silane monolayer and even more to prove that a covalent bond with proteins are formed, a simple contact angle test can be carried out to confirm the level of hydrophobicity of the glass surface after several steps of cleaning then silanization. This hydrophobicity was found to be consistent with previously reported silane surface values[131].

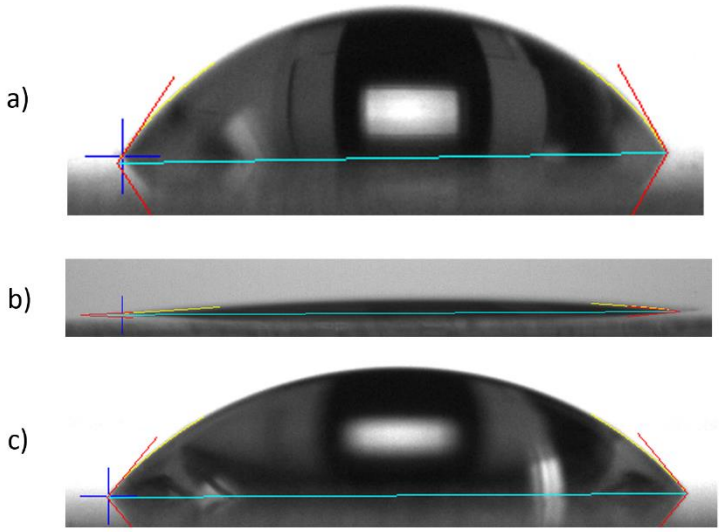

Surface state	Contact angle (°)
a) Uncleaned	58.93
b) Cleaned	4.62
c) Silanized	50.91

Figure 48: Contact angle measurement of the surface of the same coverslip, untreated, cleaned then silanized.

IX.2.ii Bead-protein Conjugation Chemistry

The anchored antiDIG beads used in the past were supplied by Spherotech, already coated with the antibody. While those beads were performing satisfyingly in terms of surface attachment and DNA binding, they suffered from a critical issue. With cyanine dyes in the buffer, the antiDIG bead would exhibit overwhelming levels of fluorescence. This could be due to a possible binding of the dye to a particularly dense coating of antibodies or possibly also the chemical makeup of the bead (polystyrene) somehow presenting a high affinity with the dye. The use of surfactant (Tween-20) reduced this fluorescence in quite high concentrations (0.1%), but still not enough to be usable.

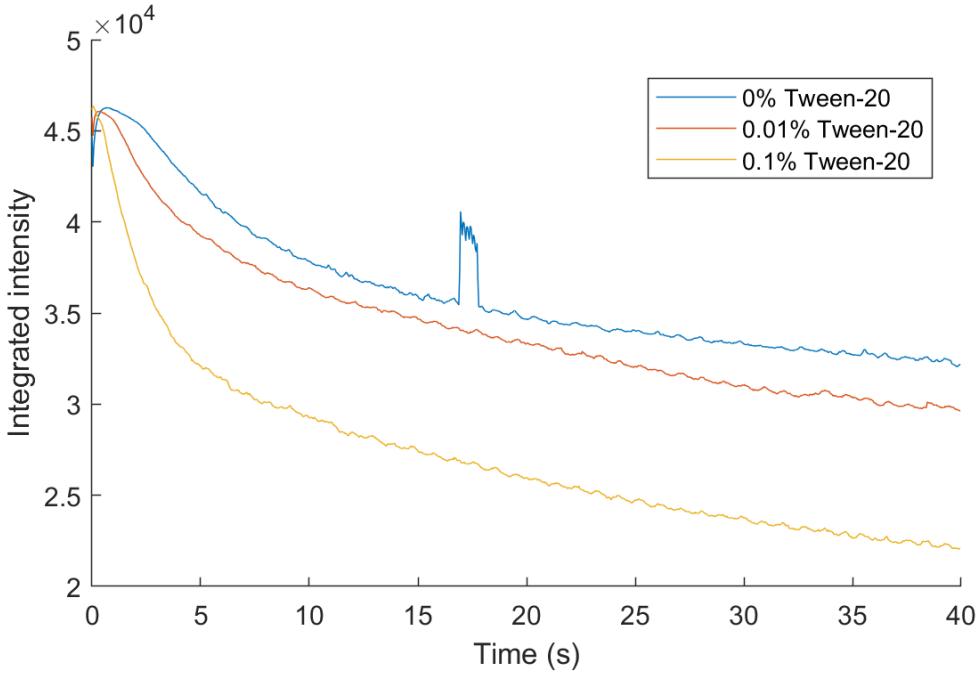

Figure 49: Integrated intensity measured from a surface attached anchor bead over time, in presence of 1 µM SYBR Gold and PBS, with a total laser power of 150 µW.

Another set of beads was found, produced by the same manufacturer that supplied the streptavidin-coated magnetic microspheres, but without antibody coating. Those beads were coated manually with commercial antiDIG by leveraging their carboxyl-coated surface to apply a classic EDC-NHS linkage. This was again done using the accessible amine moieties on the protein.

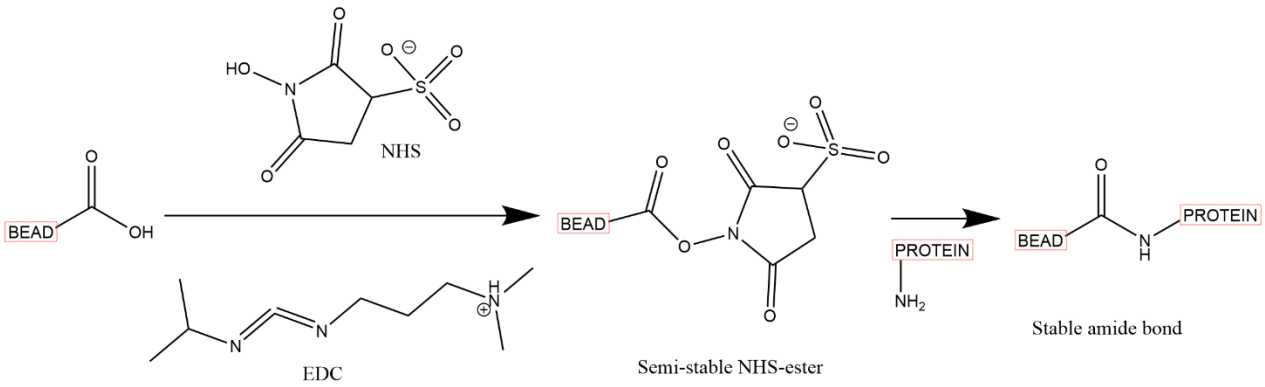

Figure 50: Chemical reactions leading to Bead-Protein covalent coupling

This approach resulted in anchor beads presenting a much-reduced fluorescence signal, either due to a lower antibody density or the different bead material.

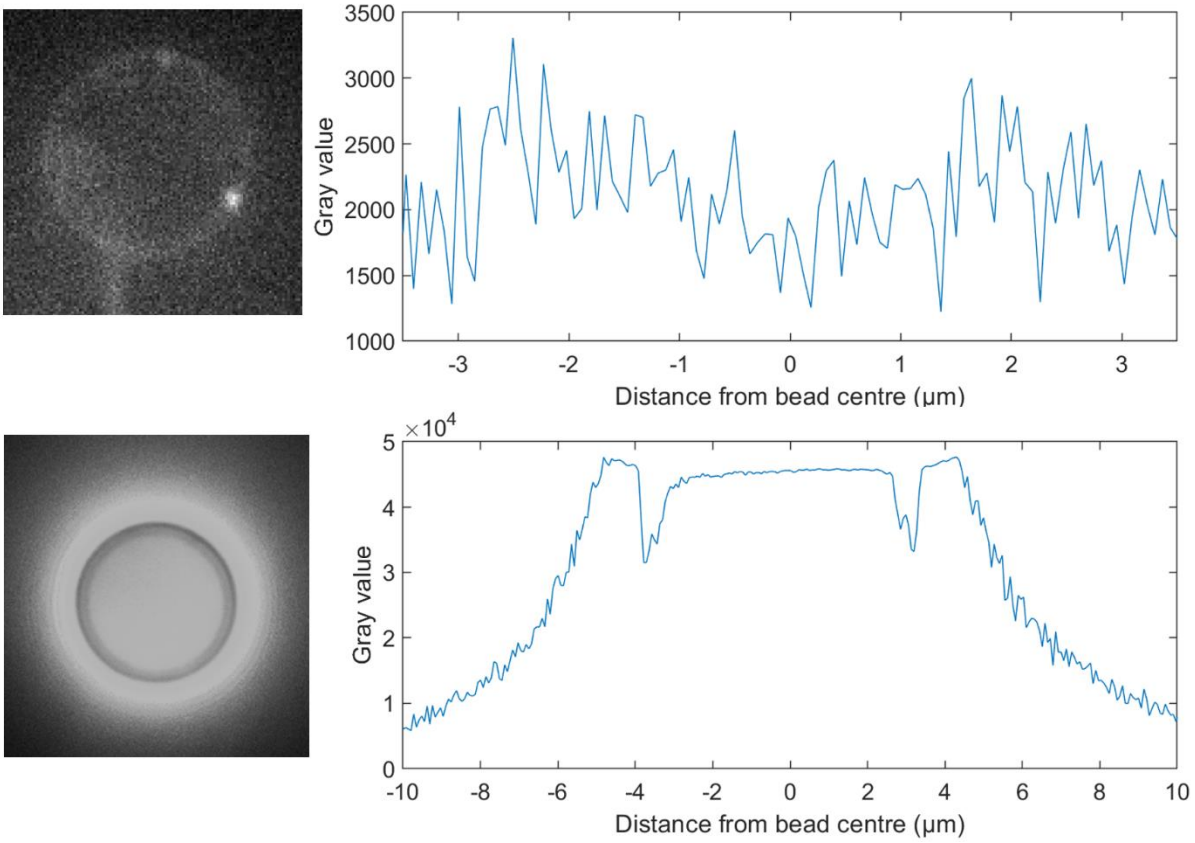

Figure 51: Equally scaled images and line profiles of Micromod (dark on top) and Spherotech (bright on the bottom) anchor beads, in presence of 1 µM of SYBR Gold, illuminated with 150 µW excitation laser power. A DNA tether is visible under the Micromod anchor bead to give relative intensity scale. The camera sensor is overwhelmed by the Spherotech bead brightness even at such low illumination power.

IX.4 Microfluidics

The latest development carried out on the microscope was the creation of a continuous flow cell. During an experiment, it is now possible to create a flow of buffer across the sample channel, mitigating multiple issues with the experiment and enabling a range of new experiments. Unfortunately, this feature was developed towards the very end of the project, and couldn't benefit the tethering experiments, but will be available for future work on the setup.

IX.4.i Flow cell designs

Designing microscopy flow cells is not typically a difficult endeavour, and those have been successfully used for quite a long time. They typically rely on an inlet/outlet system made of a chemically inert polymer tube, mounted perpendicularly to the sample and coupled with the tunnel through a hole in the slide. In our case, this is not

possible to do due to the cramped environment around the sample. Indeed, the tunnel slide is sandwiched between the objective and a large condenser lens in optical contact with the slide. Furthermore, the distance between the horizontal Helmoltz coils being restricted by the diameter of those coils, the sample slide is cut short along its length to about 45 mm.

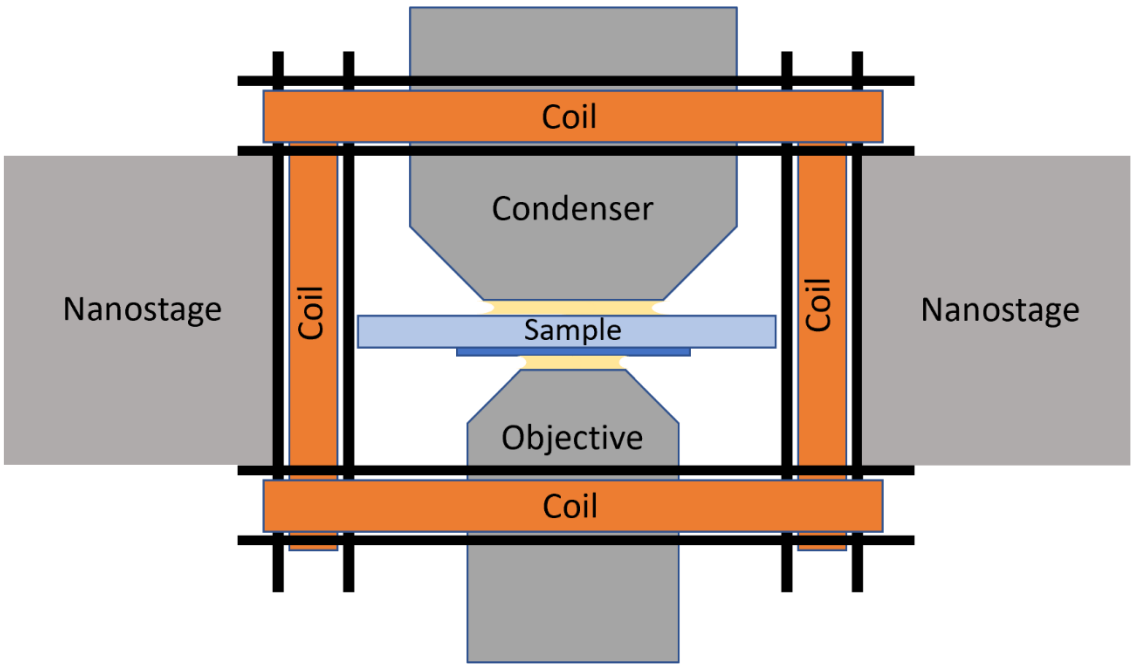

Figure 52: Schematic of the sample's immediate surroundings, view from the front. Sample holder not shown. The nanostage is shown on either side of the sample but actually revolves around it entirely, and was omitted in the centre for clarity.

This doesn't allow us to simply use a long tunnel slide, with an inlet and outlet far away from the condenser. The solution is thus to drill a hole horizontally into the slide, along its length, followed by a small perpendicular hole at the end of it, for introduction in the tunnel. This is quite a difficult thing to do with a typical glass slide, which is why I chose to instead use a plastic sheet 2 mm thick, cut to the dimensions of a typical slide. Acrylic, being transparent to both visible and 1064 nm light and presenting no significant autofluorescence properties, was selected as the material to cut those slides out of. A 25G syringe needle was cut into a 5 mm cylindrical section and inserted into the hole to act as a coupling between tube and slide. Also, typical Scotch tape is not appropriate to build the tunnel anymore, since both ends have to now be closed. I thus decided to cut a sheet of Silicone (Polydimethylsiloxane, or PDMS, Silex Ltd) 250 µm thick to use as a spacer between slide and coverslip. As long as the surfaces of both slide and coverslip are kept carefully clean, once the chamber is built it is able to withstand considerable pressures before failing, which typically happens at the interface between tube and sample rather than at the PDMS spacer. To mitigate the inevitable occurrence of a chamber failing and spilling its contents into the microscope body, the decision was taken to apply negative pressure to pull fluid out of an Eppendorf tube rather than positive pressure with a full syringe. If the cell

fails, air will rush in and the experiment stops without damage to the microscope body.

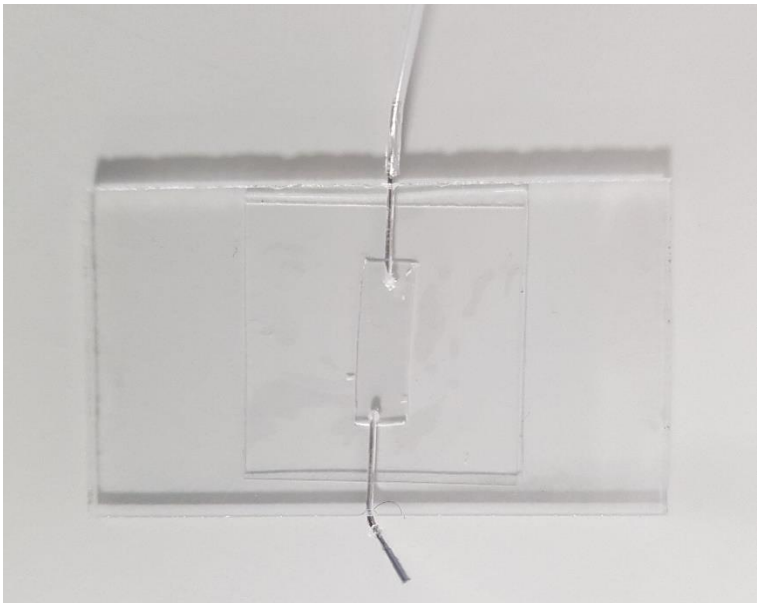

Figure 53: Picture of the assembled flow cell, with the outlet tube disconnected.

Working with this type of cell requires one significant change from the typical sample preparation. The cell must be built and mounted empty first, then injected with various solutions. It is impossible to incubate the cell first then couple the tubes, as air will be present in the dead volume of the tubes and will make experiments impossible once the flow is turned on, as the shearing forces induced by the air bubble progressing through the channel will rip away any object stuck to the sample surface.

IX.4.ii Optical trapping under flow

One simple experiment was carried out as a proof of concept. A 3 µm magnetic bead was trapped and brought approximately 10 µm deep in solution. The force on the bead was measured with no flow, then the syringe pump was turned on and different flow rates were applied, resulting in an increasing displacement of the bead from the centre of the trap, seen on Fig. 54.

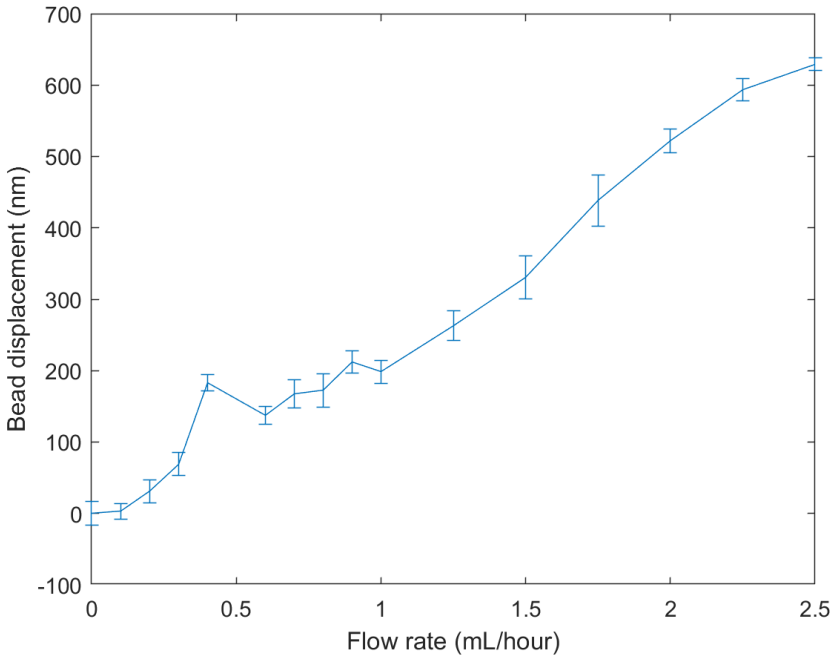

Figure 54: Line graph of the observed displacement of a 3 µm trapped bead with increasing flow rates

This shows an approximatively linear response of the trapped bead to increasing lateral flow rates, in essence a proof of concept that the system is fundamentally compatible with experiments under flow.

X. Pulling on & Twisting single DNA molecules

This chapter will describe the final application of the device after extensive modifications. We will first use the demonstrated ability of fluorescent DNA intercalators to influence the properties of DNA through their binding as a benchmark for the ability of our system to detect changes in DNA's mechanical properties. After this, we will describe the result of the experiments aimed at supercoiling DNA by twisting a tethered magnetic bead.

X.1 Influence of DNA Intercalators on the Mechanical Properties of DNA

While they are necessary to detect single DNA molecules, dyes binding to DNA will disrupt its mechanical properties when they intercalate. This fact raises the question of the relevance of intercalated DNA as a proper benchmark to study the properties of bare DNA. As our knowledge of the impact of these intercalators grow, this issue becomes more and more mitigated, the system should thus remain an appropriate tool to study these effects.

In order to study the properties of intercalated DNA, one must first measure those of bare DNA to establish a proper baseline that can be compared to highly accurate previous work done by Lipfert et al[126]. To do this, force-extension curves were measured on several DNA tethers, in the absence of any intercalating dye. 8 separate force-extension experiments were tallied, and fitted with a simplified 99% accurate WLC force-extension model[38]:

$$F = \frac{k_B}{L_p}\left(\frac{1}{4} * \left(\frac{x}{L_C}\right)^{-2} - \frac{1}{4} + \frac{x}{L_C} - 0.8 * \left(\frac{x}{L_C}\right)^{2.15}\right) \quad (46)$$

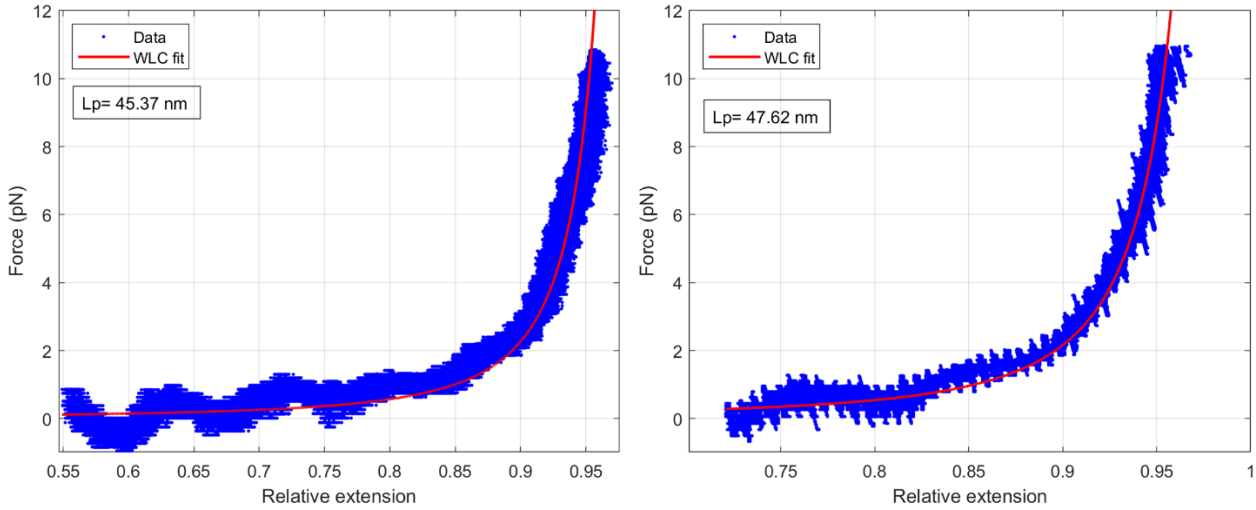

Figure 55: Example graphs of two force-extension curves of DNA in PBS. The data has been smoothed by rolling median, but the fit was applied to the raw data. Each curve represents 10 to 15 extension-relaxation cycles.

Those fits resulted in an average persistence length of 40.74 nm ± 7.8 nm (median of 42.55 nm). These values are coherent with reported values in the literature[132,45], if not slightly lower than the expected 50 nm since this solution does not contain divalent ions in significant quantities, showing that the assay worked satisfyingly. These experiment in themselves proved to be a challenge due to the difficulty of forming single tethers. This is caused by a conflict between two aspects of the experiment. On one hand, the more DNA is present on the anchor beads, the easier it is to form a tether. On the other hand, too great of a DNA coverage leads to a rapid attachment of the magnetic beads onto the anchor beads, tethered by multiple DNA molecules and leading to an irreversible bead-bead attachment.

The first step for this solution to this issue was to determine a DNA concentration that would only lead to 4 to 5 DNA molecules on anchor beads on average. This was done by imaging anchored beads in fluorescence without any magnetic beads present. While this prevented or at least mitigated the possibility of creating double tethers, it also lead to issues in manually forming tethers (by approaching anchor and trapped bead until in close proximity). With a success rate of less than 5 % lowered effectively further by the high chance of a tether being in the wrong configuration (too low on the anchor bead, placed too far left/right), a different method was devised. Instead of trying to manually form the tethers, it was decided to instead incubate the magnetic beads in the sample for 45 min so that tethers would form on their own by simple diffusion. Without any laser active and with enough training, it is relatively easy to distinguish a bead that's stuck to the anchor to a bead that is pulled close but still diffusing while observing the sample through the microscope eyepiece, which grants a much larger field of view than the camera.

These experiments were then repeated in the presence of 1 µM of SYBR Gold dye but first without fluorescence illumination. 6 brightfield DNA tethers force-extension experiments were selected and fitted with the same model. Due to the known effect of SYBR Gold on the contour length of DNA molecules it is bound to, the contour length was kept as a variable, constrained between 5 and 10 µm.

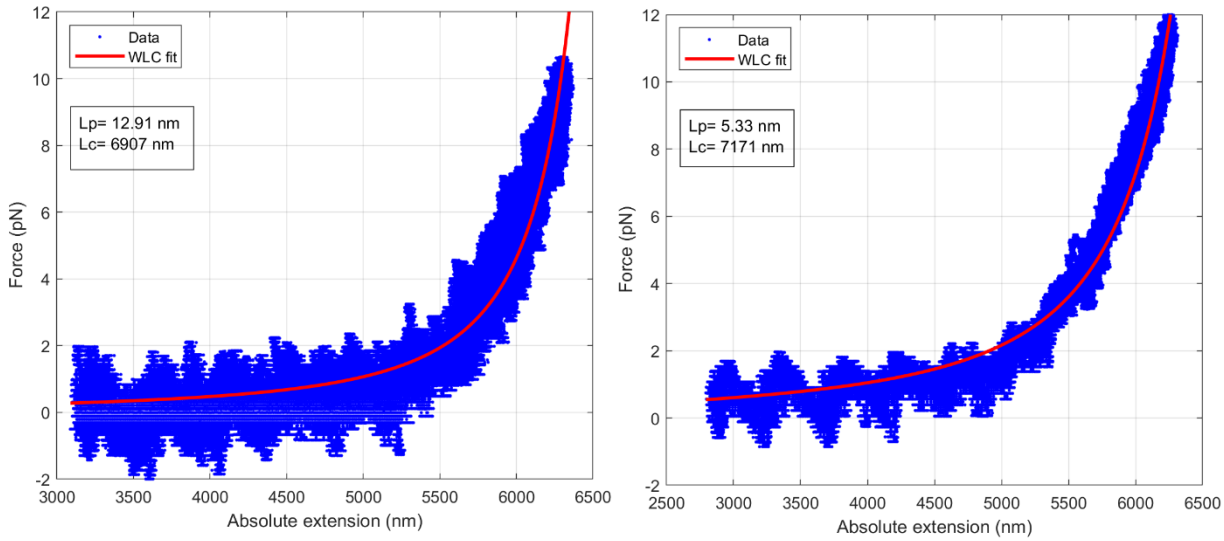

Figure 56: Example of fitted force-extension data obtained on DNA tethers in presence of 1 µM of SYBR Gold without any fluorescent excitation.

Thanks to the work done to characterize the impact of SYBR Gold on single DNA molecules, a predicted contour length increase factor was expected to be 1.45 at dye concentrations of 1 µM. The result on our fitted construct contour length should then be a 45% increase from 4970 µm to 7220 µm. The fitted values for contour length were found to be in generally good agreement with this expected value, at an average of 7498 ± 116 nm (median of 7380 nm). In contrast, the persistence length fitted values were found to be surprisingly low, at an average of 9.07 ± 3.09 nm (median of 8.19 nm), when they should be higher by a factor of approximately 15 %, going from 50 to 57.5 nm. This experimental result would imply a "stiffer" force response as extension increases when the expected result is that DNA would be left "slacker" when bound to a significant amount of dye molecules, as its effective base pair length is increased and its helicity is thus decreased. A possible explanation for this discrepancy might be that the uncertainty in measuring absolute extension obtained initially by video tracking of trapped and anchor bead introduces an error that is too high to be compensated by the Matlab fitting algorithm. Imposing a fixed contour length of 7216 nm in the fitting only worsened the quality of the fits.

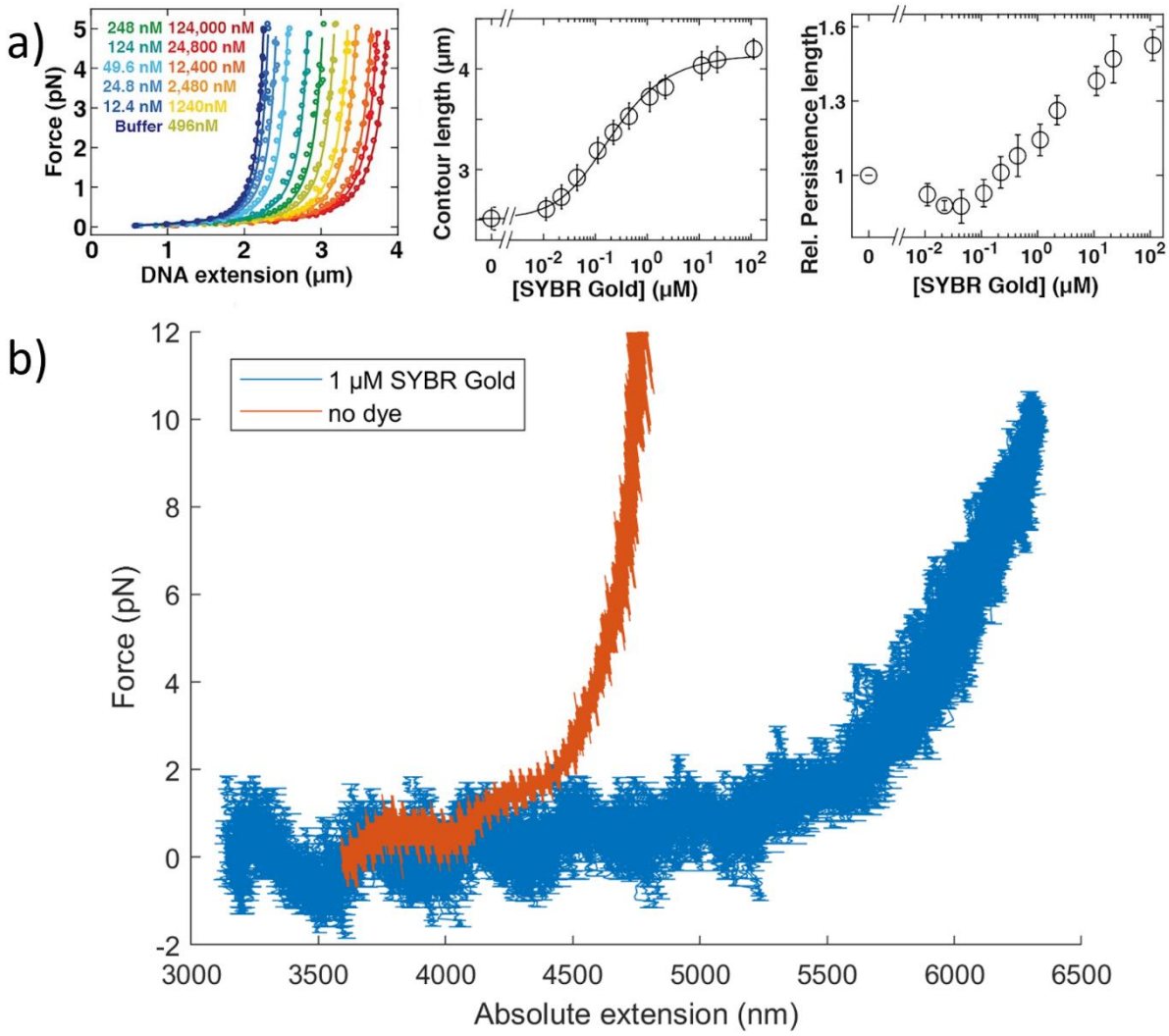

Figure 57: The impact of SYBR Gold binding on DNA's tensile properties. a) Data obtained by Kolbeck et al.[124] showing the impact of the binding of SYBR Gold on dsDNA.The first graph shows several force-extension curves obtained under a range of dye concentrations. The second shows the contour length increase (from 2.6 µm) as dye concentration increases. The third shows the measured effect on the persistence length of DNA tethers. b) Example of force-extension curve data obtained with and without SYBR Gold in solution. This shows the expected effect of the dye qualitatively, extending the apparent contour length of the tether, reducing the slope of its force response due to a supposed persistence length increase.

This experiment was also carried out for the first time under fluorescence, demonstrating the much-improved performance of the fluorescence imaging and allowing the monitoring of the force response of the tether for several tens of seconds until breakage occurred.

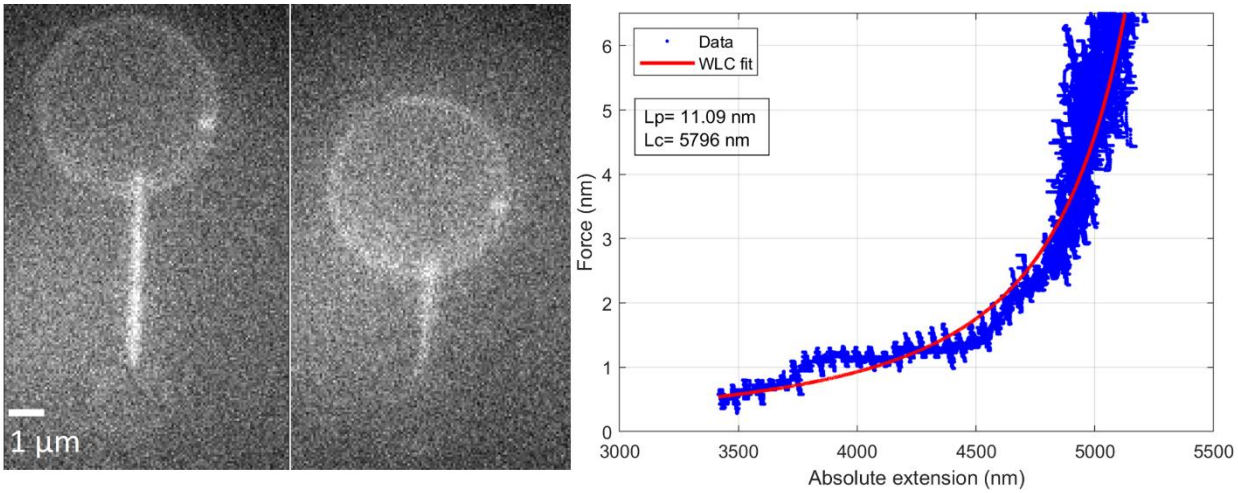

Figure 58: On the left, two fluorescence images of the tether under maximum, then minimal extension. On the right, corresponding fitted force-extension data.

The resulting fitted parameters did unfortunately not match expected values, for persistence length as well as contour length. This is suprising since in this case the uncertainty on the tether extension is much reduced by the ability to simply measure its value at the maximum of extension on the fluorescence image. This could be the result of the makeup of this particular trapped bead, or be nonspecifically attached to one of the bead, shortening its effective contour length. Single-stranded breaks would also lower the effective persistence length of the molecule.

X.2 Twisting DNA

After confirming that the optical trap system was able to measure forces on single DNA tethers, it was time to attempt supercoiling it.

X.2.i Supercoiling one DNA Tether

The first and simplest experiment to attempt was to find a DNA tether, confirm its "quality" by recording a force-extension curve then proceed to supercoiling it. This was done in a "position-clamp" type fashion, where the nanostage is kept static and the force response is recorded. An arbitrary "high" tension was first produced, the tether was underwound by 200 turns (σ= 0.145) to verify an expected absence of force response, brought back to native Linking number, then overwound in increments of 50 turns. Two scenarios occurred during those experiments: either a force response was detected during underwinding, in which case there was necessarily several tethers, or no force response would be detected either way, at which point the tether was deemed non-torsionally constrained and thus discarded. All of the tethers that were found to produce a force response during supercoiling were revealed to be

multiple tethers in fluorescence. This would be characterized by the “Y” shape of the tether, with the two different anchor bead attachment points forming the branches that would meet where the DNA molecules would be spun around each other, forming a kind of simple braid.

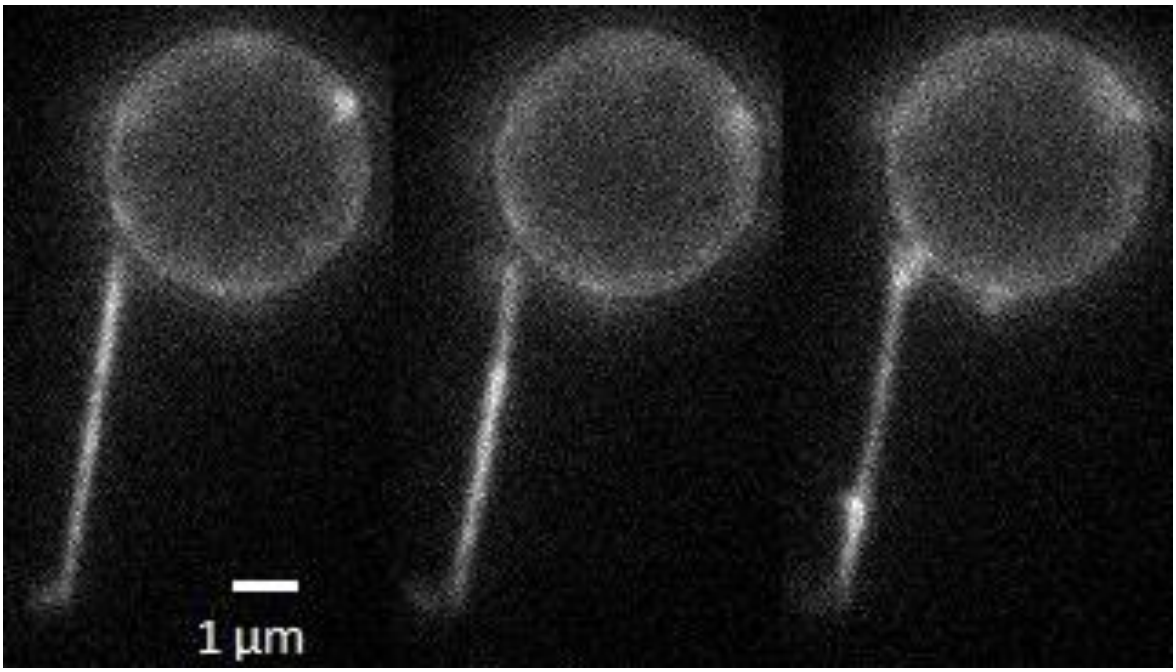

Figure 59: Pictures showing a braided "double" tether, where the DNA molecules have been spun around each other, appearing as one brighter tether. One of the two tethers snaps near one end and retracts along the second. This proves the ability of the magnetic tweezers to impose a torque on DNA, this kind of structure has not been directly observed previously in fluorescence. The tethers appear longer than usual as this was obtained with an unpurified DNA mixture containing larger than the 14.5 kbp fragments.

A major issue when exclusively working with “pre-formed” tethers is that once a tether has been worked upon with the magnetic tweezers, one cannot find a new tether on the chip and proceed as with the previous. Indeed, since the entire sample is affected at the same time, the level of supercoiling on the other tethers is unknown. One should not assume that the total level of supercoiling is simply the sum of the applied turns on the sample. This is because of the variability in tether/bead configurations, leading to an inhomogeneity in their response to supercoiling when the magnetic bead isn’t trapped. The tunnel slide being 22 mm long, the magnetic field gradient becomes significant and will thus also apply a tensile force directed towards the area right above the objective lens. This way, using “pre-formed” tethers, the chip is effectively single-use.

A single occurrence of what could be a DNA plectoneme was observed when a DNA tether was created manually and an extremely large amount of positive supercoiling was introduced (1000 turns, equalling a supercoiling density of 0.72).

Unfortunately, an error occurred and the QPD data acquisition failed to start. I struggled to observe a similar structure for several months following this.

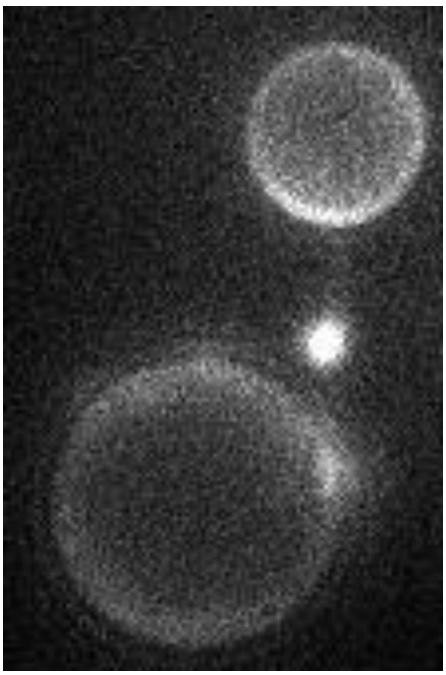

Figure 60: Picture of a possible DNA plectoneme

X.2.ii Possible explanations and mitigation attempts

There should only be a finite amount of reasons that would lead to DNA not being supercoiled. The first and simplest reason would be that the beads are not spinning. This was entirely ruled out due to several reasons. The first is that when several tethers are present, they are clearly braided around each other when the magnetic tweezers are spinning. This was observed in real time, with the central part of the "Y-shaped tether" growing in length over time. This fact is incompatible with this hypothesis, as forming this type of structure by chance should be impossible due to its highly constrained state.

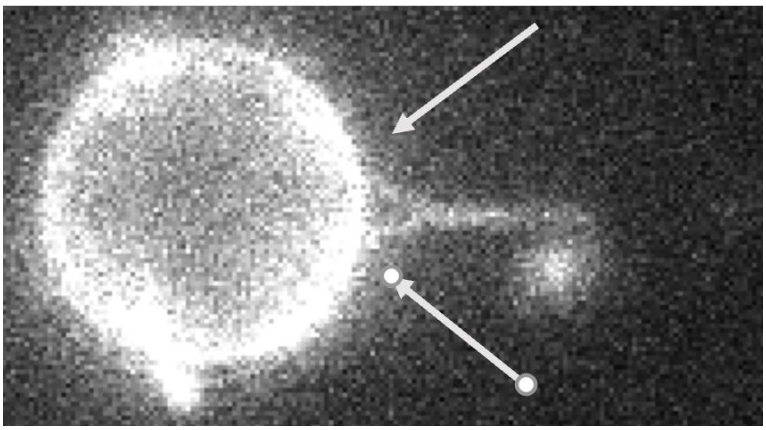

Figure 61: Fluorescence image of a braided "double tether", with the two different anchor bead attachment points pointed by the white arrows.

The second reason that would lead to a tether not being torsionally constrained is that the DNA itself is damaged, with one or several single-stranded breaks. Attempts were made to fix this possible issue by incubating the DNA before loading with Ligase in the appropriate buffer. This enzyme's role is to repair those single strand breaks ("nicks"). This did not fix the issue, at which point the hypothesis was made that the loading itself inside of the thin (150 µm high) tunnel in the chip could shear DNA and introduce damage. To remediate to this, the tethering experiments were carried out in ligase buffer, with ligase present. The consequence of this was the rapid irreversible sedimentation of most magnetic beads. Nevertheless, a few experiments were carried out, still with no force response to twisting.

The last possible issue lay at the interface between bead and DNA, that is the protein-ligand linking that provides attachment between those two. It may be that despite our best efforts, fewer than 1 digoxigenin or biotin moiety per strand would be present. This hypothesis was not tested and was assumed to be improbable since previous work established topological constraint using only four moieties per end[119]. If the issue isn't coming from the tether, then it must be coming from the bead protein coverage. This would mean that the protein labelling is too sparse, and that a tether may only access one at a time. This is currently the favoured hypothesis and might also be at the root of the brightness issue of Micromod's anchor beads compared to Spherotech's.

A stark difference in anchor bead brightness was found, between Spherotech and Micromod beads, the commercially labelled Spherotech beads presenting an overwhelming brightness when in presence of SYBR Gold. While this difference could be due to a differing chemical makeup of the beads themselves (Spherotech's polystyrene vs Micromod's proprietary coating around a maleic acid core). An interesting observation was made when observing an older batch of Spherotech beads with dye present. They were found to emit a significantly lower amount of fluorescence. Considering the fact that Spherotech claims to label these beads by simple passive adsorption, it could be assumed that this protein coverage decreases over time. If the bead brightness in presence of dye also decreases over time, then

one could assume that SYBR Gold actually binds to AntiDIG antibodies themselves. If the custom labelled Micromod beads are considerably less bright than Spherotech's, it could be due to a considerably lower surface density of protein, which could explain the lack of torsional control.

This issue could prove deadly to the surface anchored experimental setup chosen for this experiment. Indeed, if no continuous flow is present, then the DNA tether must be asymmetrically labelled, with a different molecular linking system on each end. Otherwise, both ends would quickly bind to the same bead and prevent the formation of any tether. If on the other hand the system was under flow, then the hydrodynamic forces from the buffer, carrying DNA molecules, would prevent the attachment of the second end after the first binds to a trapped bead. In any case, the development of a benchmark to evaluate the protein surface density on a given bead would greatly benefit the project.

XI Discussion

This section will attempt to discuss as well as critique the results obtained in this document, identify areas of performance improvement including possible technical solutions for future work on developing the microscope.

XI.1 Results Discussion

While the components of the device itself were shown to be working satisfyingly in isolation, the ultimate goal that is the supercoiling of single DNA molecules was apparently not attained, due to the apparent lack of topological constraint on the DNA tethers. It is reasonable to assume that the magnetic tweezers were working as intended, rotating the trapped bead due to the aforementioned twisted double tethers. Therefore, only three possible issues are occurring (possibly combined):

- Single strand breaks on the DNA molecule

- An unexpectedly low (less than 1 per strand) number of linkers on one or both end of the DNA molecule.

- A low enough protein coverage on either bead resulting on only one bound AntiDIG/Neutravidin.

Exploring the protein labelling density on either bead was proposed earlier and would probably yield interesting data. Another troubleshooting method could also help figuring out if the DNA molecule's integrity itself is the issue. To do this, a new DNA tether could be built, in a simpler and higher yield manner. This would rely on using the entire λ phage plasmid, each end of that double-stranded molecule being non-blunt (12 bp cos "sticky ends"), meaning that a strand on each end has an unpaired single-strand overhang. This has for consequence the possibility of coupling each end with a different double-stranded oligomer as long as it contains a complementary overhang. This would be purchased from a commercial supplier as already labelled with biotins or digoxigenins, with a simple ligase-mediated ligation reaction to obtain the finished product. The number of those coupling moieties would then be much more accurately controlled, and the production process would be considerably cheaper, yielding a much higher amount of product. The drawback being that this molecule being so long (48.5 kbp, 16.5 µm long), the position of the field of view should be adjusted to place the optical trap close to the top/bottom of it. It would also be harder to use this construct to detect subtle mechanical effects of for example a single ligand binding, since the molecule would be able to absorb it with no meaningful change.

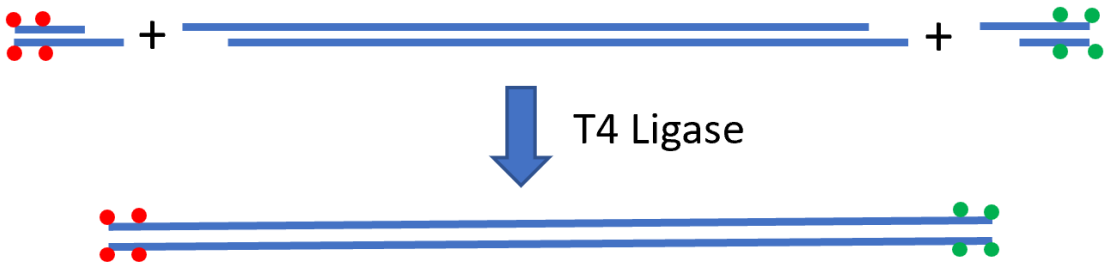

Figure 62: Reaction schematic of the one-pot production of a Lambda DNA tether.

The last step of the process being a ligation using ligase enzymes, one should be relatively confident that the molecule does not carry any single-strand break. If twisting attempts were found to still fail, the issue should then be by elimination the labelling density on the beads.

XI.2 Comments on the setup performance and shortcomings

The limited extent in which DNA's physical response was quantified in this work is in part related to some technical shortcomings. Those issues are generally not inherent to the techniques chosen but would necessitate a relatively consequent amount of work to be mitigated.

The most glaring limitation when operating the device for the first time is how cramped the sample's immediate surroundings are, and how little amplitude of movement the manual stage allows, on the order of around 25 mm^2 (5 by 5 mm^2). This is caused mainly by the nanostage and oil contact condenser. The nanostage having a relatively small central hole to which the sample holder is attached prevents horizontal movement and restricts the size of the tunnel slide to 45 mm in length. The result of this considerably increased the difficulty of installing a basic fluidic cell, making it unnecessarily complex and risky in case of leak. This would result in the deposition of salty buffer on hard to access optics (filter cube, eyepiece mirror, etc) which would render the device inoperable for a possibly long period.

The difficulty of operating a microfluidic device in this configuration led to the inability to expose a single isolated piece of DNA to several chemical conditions, which impeded the ability to screen for ideal reaction conditions for linking the DNA molecule with the beads. Control over the flow of buffer would have also led to an easier in situ construction of the tethers, by taking advantage of the drag force to extend a DNA molecule stuck to an anchor bead as previously done in the past[133]. While under fluorescence illumination, the flow of buffer would have also acted in a beneficial way by advecting away fluorescent dyes in a reactive state, enhancing the lifetime of the DNA topological constraint by preventing the appearance of single and double stranded breaks.

Finally, one of the most limiting characteristics of the setup may lie in the experiment configuration itself. Indeed, the use of an anchor bead to impose topological control may actually create more issues than it solves. Firstly, the physical anchoring of the bead to the surface is not even necessary to prevent the non-magnetic bead from relaxing the added supercoiling density by rotation[119]. The equations of motion of such a system (freely floating supercoiled DNA dumbbell) show that barring extreme supercoiling density, the DNA shouldn't be able to generate enough torque on the non-magnetic bead due to the bead's considerably larger surface. The anchor bead attachment imposes a relatively short distance (less than the trapped bead diameter) between DNA/trapped bead and the sample surface. This leads to a heightened background fluorescence signal due to the dye molecules being immobilized, which is functionally akin with being bound to DNA by preventing excited dye relaxation by rotation. Additionally, it has proven difficult to find a surface that performs as well as possible in three areas: promote anchor bead attachment, prevent trapped bead attachment and prevent free dye attachment which can be contradictory to one another. If a surface promotes nonspecific attachment too much, the anchor beads will quickly bind, but so will the trapped magnetic beads, resulting in a relatively low sample lifetime (less than 20 minutes) as all magnetic beads will settle on the surface and it is currently impossible to inject new ones. If the surface is too well passivated, it may decrease the nonspecific background emission, but will also drastically reduce the amount of available anchor beads.

Solving or mitigating the issues listed above can be done through modifications to the existing setup. In the following part, I will propose several technical modifications to accomplish this goal, proposing two different routes of differing costs.

XI.3 Possible technical improvements

XI.3.i Solution 1: Replacing the anchor beads

A relatively simple or at least less technically involved route to take to improve the experiment performance could be to focus on engineering the sample itself, with the main goal being replacing the anchor beads with another solution. This would imply a similar experiment configuration as with DNA curtains, replacing the anchors with a long structure raising the surface of the glass. Glass can be etched to create microstructures, using either chemical etchants[134] or more physical approaches, using Plasma[135] or UV lasers[136] for example. Those techniques are well known and the facilities to create those are easily accessible, but they present inherent limitations in terms of attainable depth and channel wall regularity. The fact that the created structures are made of the same material would also possibly make the attachment of DNA molecules less consistent as there would be no control over where they bind.

Another solution would be to instead of removing material to create channels, bond thin strips of gold to the sample surface, enabling relatively quick and very selective coupling chemistry[137]. This setup would also require the use of continuous

flow in order to extend the DNA molecules coupled to the surface for easier bead attachment.

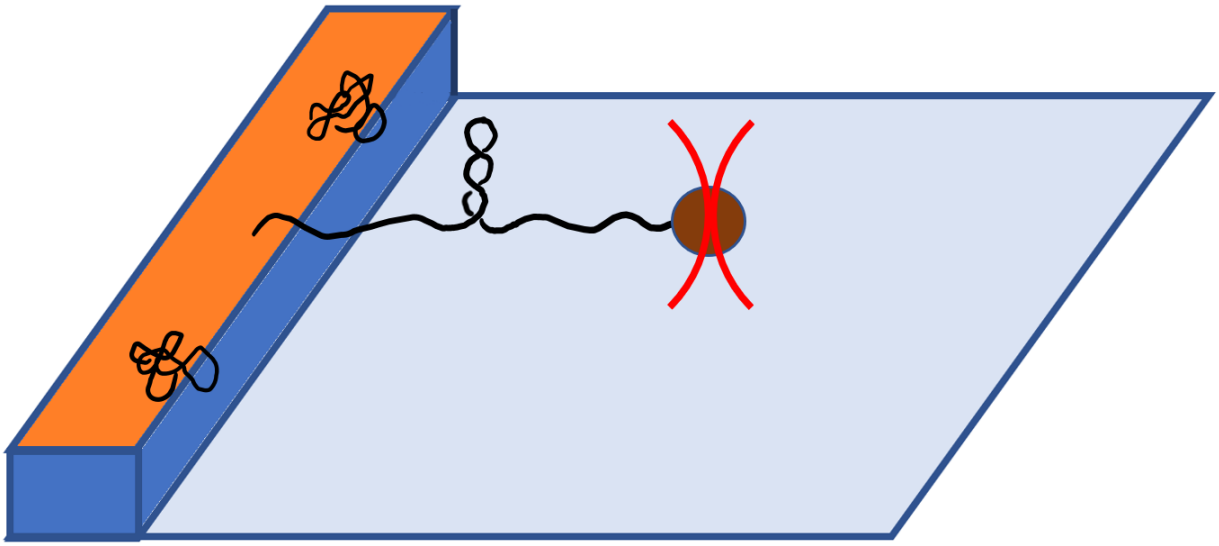

Figure 63: Cartoon of a possible DNA curtains-like assay. The orange surface represents Neutravidin labelling, the black lines represent the DNA tethers, one of them extended and supercoiled by the brown magnetic trapped bead (Optical trap in red).

This type of sample would be easier to work with, as it would facilitate increasing the local density of DNA tethers and enabling exploring the sample much more systematically and consistently. The challenge would be to find a cost-effective sample construction protocol and to ensure that the produced chip maintains it integrity when pumping liquids through it.

XI.3.ii Solution 2: Complete setup redesign

As we have seen in the beginning of this section, a considerable amount of practical issues come from the current lack of space around the ample. In order to increase it, one must think about removing the nanostage, as the central hole in which the sample holder is bolted on is 95 by 60 mm, and this has to include the two large horizontal coils as well. This nanostage plays a crucial role since attaching the anchor bead to the surface does not just grant us the ability to maintain torsional constraint but permits easy force transduction by precise translation of the stage. It also allows us to stretch the DNA tether in three dimensions. In order to remove the nanostage, one must then find another way to displace an optically trapped bead. This can be achieved by implementing a classic dual-trap DNA dumbbell setup. One of the traps can stay static while the other one can be steered to stretch the tether. Once properly tuned, this would guarantee that the DNA molecule is held parallel to the surface at any time and changing the focus would only affect the dumbbell height without

altering its relative angle to the surface. It is possible to create (weaker) traps further away from the surface than a 1.49 NA objective allows by using 1.2 NA water immersion objectives to negate the background noise from the surface, distant from more than 50 µm. Unfortunately, simple dual-trap designs based on statically splitting the IR beams by polarization then recombining them would not be adequate, as the ability to measure force by back-focal plane detection doesn't work anymore, both traps shining on the QPD at the same time. Those traps cannot be accurately separated after their interaction with the sample without doubling the number of QPD detectors, introducing potential issues with bandwidth and alignment. The solution to this issue is to use only one beam, but to timeshare it between two positions using an Acousto-Optic Modulator (AOM). Acousto-optic devices rely generally on the application of a radiofrequency vibration on a crystal through which the laser beam goes, the variation of that vibration (frequency and amplitude) changing the optical properties of the crystal (deflection angle and transmissivity). Acousto-Optic Deflectors are capable of deflecting a beam along larger angles than AOMs, but do so at a much slower rate, incompatible with timesharing. Indeed, the switching frequency between each trap must be beyond 10 kHz to prevent the trapped beads from decaying out of their position[138]. The second advantage that an AOM system provides is the possibility to couple in a fast photodiode that will be made to collect a fraction of the light downstream from the AOM and create a feedback loop, allowing the AOM to stabilize the beam power at high speeds, improving the stability of the trap greatly. This ability is mandatory since the transmissivity of the AOM crystal is dependant on the deflection angle, but this drawback is then mitigated by the unparalleled ability of AOMs to modulate an incident beam power at a kilohertz rate.

Since only one trap is active at a given time, as long as the QPD reading rate is considerably higher than the switching rate (80 vs. 10 kHz), the force on each bead can be independently determined throughout the entire experiment. In the case that one would want to collect the fluorescence signal along a smaller than 1 µm DNA molecule, adequate care must be taken to avoid suppressing the dye fluorescence with the infrared trap light. To do this, one can interlace the fluorescence laser in between each infrared trap light pulse. The proposed modification would leave this possibility open even if the necessary high-performance synchronization equipment is expensive and needs to be produced in part in-house for adequate performance (radio frequency generation and synchronization), on top of the additional AOM device. In order to maximize the capabilities of the device in terms of multi-colour fluorescence imaging, a Supercontinuum laser could be used, coupled with a sub-millisecond switching acousto-optics module to quasi-instantly select and alternate several wavelengths, enabling alternate excitation (AlEx), precise power modulation and thus more accurate FRET measurements.

A second issue Appears if the experimental configuration in which a DNA dumbbell is freely floating in solution is chosen arises. Due to the fact that the only magnetic bead that was found to be trappable contains a small relative proportion of iron oxide compared to those that can't, it is difficult to distinguish it from a non-

magnetic bead. This leads to an expected mismatch of the beads in the dumbbells 75% of the time. One could trigger the rotation of the magnetic tweezers and attempt to figure out by eye which is which, but the higher the quality (sphericity) of the bead, the harder this is. To solve this, a multi-channel microfluidic chip device can be used, made possible with a careful design and precise control of the flow and channel construction. This is also now considerably easier to set up due to the much larger clearance around the sample thanks to the removal of the nanostage. Three channels should prove sufficient. The central channel will be where the experiments are carried out with only buffer present and a possible DNA ligand depending on the studied events (tension and torsion-dependant binding kinetics measurement for example). One lateral channel will carry the non-magnetic beads, with DNA pre-attached on them by one end. The assembly of the device will start in this channel, where a bead will be trapped and dragged towards the second lateral channel on the other side of the chip. This channel will contain the magnetic beads along with the DNA-binding dye. The two beads will be brought into the central channel, brought close enough for the DNA to link with the magnetic bead and the measurements can then begin. It is important for the flow to be parallel to the DNA dumbbell since it will extend the DNA. A 2-dimensional AOM could be theoretically used, but since it is practically made of the combination of two AOM crystals, the precise positioning of the device in a conjugate plane with the objective is impossible. Additionally, the power loss due to the deflection of the beam would be multiplied, and a power feedback loop would thus be harder to put in place.

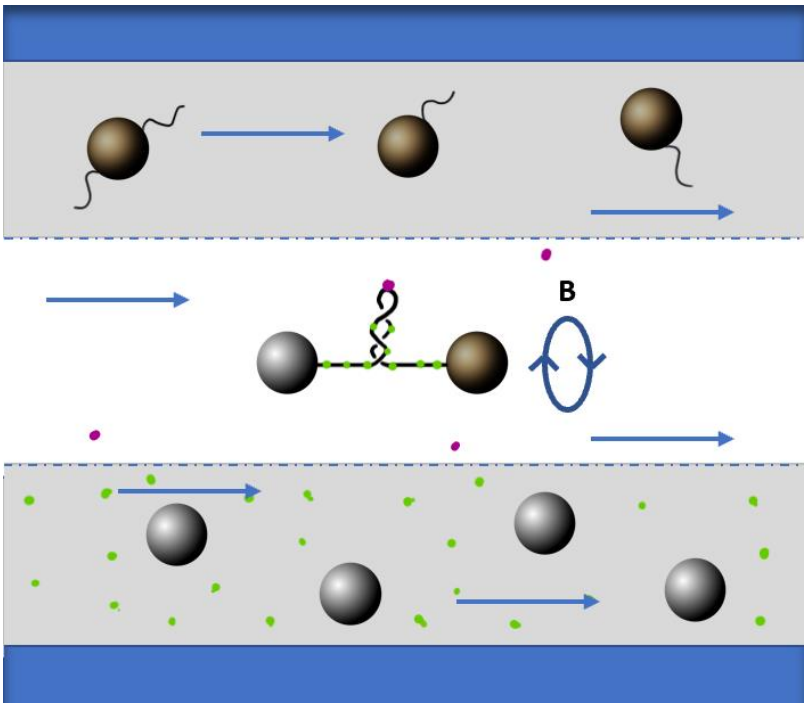

Figure 64: Cartoon of a possible further development of the microfluidic system. The dark blue rectangles represent the boundaries of the tunnel formed by the cut PDMS sheet, the arrows symbolize the direction of the fluid flow. The top channel would contain magnetic beads, already coupled to the DNA construct. The bottom channel would contain the non-magnetic beads along with the DNA intercalator dye in green if needed. The magnetic beads would be trapped and then brought into this

channel. The middle channel is where the experiment would take place, including constructing the tether, the purple dots representing a possible DNA ligand of interest, like a Nucleoid-Associated Protein.

By replicating a proven optical design based on the one described in depth by Chemla *et al.*[139], the risk of unforeseen design hurdles is much reduced, with the largest amount of original work being required only around the sample with the redesign of the sample holder and of the Helmholtz coils. By freeing a considerable amount of space around the chip, it is even possible to add a third pair of Helmholtz coils. Rotation of a DNA-bound bead with three degrees of freedom is not necessarily interesting, but by only selecting two of those three coil pairs, the operator becomes capable of generating a magnetic moment rotation with an axis perpendicular to the sample surface. This would enable applying magnetic tweezing to a comparatively simpler and more limited but extremely parallelizable technique where optical trapping and high-bandwidth force measurement are not essential anymore, but fluorescence imaging still is.

This technique is named Tethered-Particle Motion (TPM). In this technique, smaller, typically around 100 to 300 nm diameter beads are tethered to the surface by DNA. By tracking and computing the amplitude of the diffusing bead around its attachment point, it is possible to measure the overall contour and persistence length of the molecule of interest, as a function of its supercoiling. This persistence length can be perturbed by varying parameters, such as pH, ionic strength[45], temperature[140] or the concentration of a certain molecular compound. TPM, which has been further developed into HT-TPM[141] (HT for High Throughput) with the patterning of the surface with Neutravidin to greatly enhance the amount of simultaneously visible DNA complexes, up to a few thousands depending on the chosen objective magnification. This design, if successfully implemented, would result in a unique microscope able to carry out highly precise experiments on one DNA molecule, but also quickly screen large ranges of parameters that influence the mechanical properties of DNA. The insight that TPM experiments provide is relatively limited, but is an extremely appropriate technique to explore vast ranges of parameters with an large population of individual molecules. The work by Agarwal et. al demonstrates the considerable throughput of a flow-capable magnetic TPM setup[97], measuring the response of DNA tethers to supercoiling and topoisomerase activity, on 50000 single molecules within a single frame. This type of experiment would complement a low throughput high resolution assay such the DNA dumbbell tweezers setup extremely well.

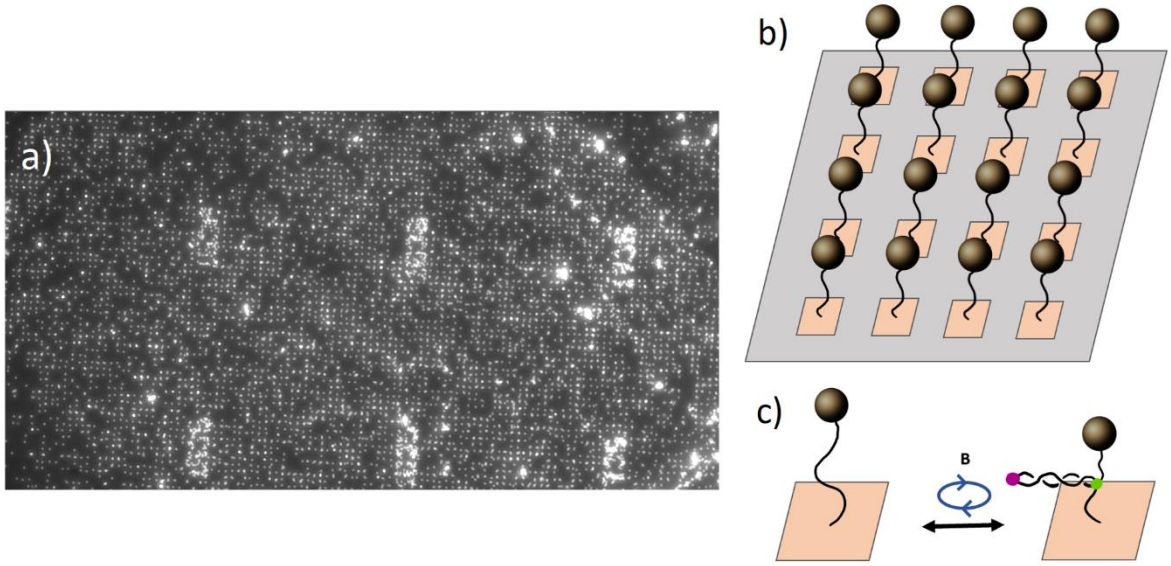

Figure 65: a) Image of a HT-TPM sample (darkfield illumination) elaborated during a previous project. Each bright dot is a 300 nm AntiDig-functionnalized polystyrene bead tethered to the surface by a single DNA molecule. Up to 1000 valid complexes can be tracked simultaneously, limited only by the camera field of view. b) Cartoon of a HT-TPM assay, showing the Neutravidin micropatterning in orange. This allows a precise control over the density of tethered beads, ensuring that they are far enough from each other to avoid interfering. This technology can be applied to magnetic tweezers-type equipment to increase their throughput significantly. c) a type of experiment achievable by applying Magnetic tweezing to HTTPM. The DNA tether can be supercoiled by the two pairs of coils parallel to the sample, and possible plectonemic DNA ligands binding could be detected.

XI.4 Future work

Before starting to iterate on this design, a range of experiments should still be carried out. The device has proven the concept of a robust microfluidic system applicable to the current design. The flow system should be made more characterized and stable through the use of laser cut PDMS membranes and a calibration of the flow speeds in and ex situ.

The same tethering experiments as described earlier in this document can be carried out again, with buffer exchange in between to vary the amount of dye and add a compatible radical scavenger and ligase mix. If this change of protocol fixes the tether topological constraint issues, a range of exciting experiments will suddenly be relevant. The second excitation laser line should then be realigned and the second camera reinstalled for two-colour DNA supercoiling experiments with nucleoid associated proteins. Proteins like IHF in which our group possesses a lot of existing data could be studied through yet another angle.

XI.4 Conclusion

The work carried out during this project resulted in a partial redesign and much-improved level of performance of the microscope and tethering technique in many key areas, and a better understanding of the most limiting factors to control for when using the instrument. While every hardware component of the experiment was found to function with a satisfying level of performance, the main bottlenecks are now probably almost exclusively the biochemical aspects of the experiment.

This project was a central part of my life for the last 4 years, and while there are some typical feelings of frustration regarding the limitations of its output, it was the most exciting and fascinating endeavour I participated in, which taught me a large amount of lessons, many not science-related. Navigating through the global events of the last few years also proved difficult but also rich in teaching, and I am now convinced that scientific research is the domain within which to build the rest of my career, even if I chose to abandon the classic academic pathway for a more technical direction. I may have found a way to stay helping to develop an exceptional instrument with many promises.

XII Appendix

XII.1 Protocols

XII.1.i Protein functionalization of carboxylated beads

Materials:

- 250 uL of stock COOH-beads solution (12.5mg of beads)
- 62.5 uL 0.5M MES buffer
- 2mg EDC
- 4mg NHS
- 200 uL of 200ug/mL Protein solution
- 1X PBS
- 100uL of 25mM glycine in 1X PBS

Procedure:

- Beads activation: Mix the 250uL of stock beads solution with 2mg EDC, 4mg NHS and 62.5ul 5X MES buffer (1X= 100mM), incubate at RT for 45 min under agitation
- Wash and incubation with protein: Spin the mix down for 10 min at 1200G (4k RPM on the Eppendorf centrifuge), resuspend in 200uL of 200ug/mL Anti-Dig solution in 1XPBS under vortex, incubate at RT for 3 hours
- Wash and quench of the unreacted EDC groups: Spin the mix down, resuspend in 100 µL of 25 mM Glycine in 1X PBS, incubate under mixing for 30 minutes
- Washes and final dilution: Wash the mix 3 times by centrifugation/resuspension in 500 µL 1X PBS

XII.1.ii Glass coverslip cleaning and silanization

a) Cleaning

- Clean coverslips in an Ozone-UV cleaner for 10 minutes
- Sonication for 10 minutes in a 2% v/v Hellmanex bath

- Rince twice in pure mQ water for 10min under sonication, change beaker and slide holders between the washes
- Dry under Nitrogen flow, then clean for 30 minutes in the Ozone cleaner
- If coverslips are to be stored for more than a few hours, Ethanol wash for 10 minutes under sonication then dry under Nitrogen

b) Silanization

- Silanization mixture:
  - 1.5 mL (3-Glycidoxypropyl)dimethoxysilane (GPDMS)
  - 60µL N,N Dimethylbenzylamine
  - 58.5 mL Isopropanol

- Put clean coverslips face up in a glass petri dish (120mm diameter), 10 at a time, pour 30mL of silanizing solution and let rest for 90 min.
- Retrieve the coverslips and sonicate 5 min in Isopropanol
- Quick wash in absolute Ethanol, dry under Nitrogen
- Keep in 115°C oven for 15min, then store in an airtight box, use within 14 days

Note: Wash-N-Dry coverslips holders are recommended for the entire protocol

XII.2 Code

XII.2.i Force-extension processing and analysis code (Matlab)

```
o=-1; %1 if stretching is upwards, -1 if downwards
Amplitude=X.XX; %Stage movement amplitude in MICRONS
maxdistance=XXXX; %max distance between beads in nm
k = XX.XX; %BT stiffness
filename='ramp.lvm';
filename2='XXX.lvm';
A=lvm_import(filename);
Data=A.Segment1.data;
clear A
```

```
index=find(Data(:,10)>3,1);
Data=Data(index:end,:);
clear index
x=1;
i=1;
while x>=0.02                    %Detects the subsequent "acquiring" period
   x=sum(Data(i:i+199,10))/200;
   i=i+1;
end
Data=Data(1:i-2,:);
clear i x
Video = csvread('ramp.csv',1);
time=Data(:,1)-min(Data(:,1));
BT=-o*Data(:,2);
SUM=-Data(:,4);
nBT=BT./SUM;
a=length(nBT);
b=length(Video);
c=round(a/b);
for i=1:b                        %averages the QPD data aquired during each frame
Video(i,5)=mean(nBT((1+((i-1)*c)):(i*c),:));
end
mnBT=Video(:,5)-mean(Video(end-500:end,5));%the bead actually relaxes at a lower force
than initially after being stretched, so better to take the last frames to average and ignore
the first "low displacement" part
disp=o*(Video(:,4)-mean(Video(end-100:end,4)))*0.069;
Output=[disp mnBT];
writematrix(Output,'Outputramp.csv')
[xData, yData] = prepareCurveData( disp, mnBT );
% Set up fittype and options.
```

```
ft = fittype( 'poly5' );
excludedPoints = xData < -10;
opts = fitoptions( 'Method', 'LinearLeastSquares' );
opts.Robust = 'Bisquare';
opts.Exclude = excludedPoints;
% Fit model to data.
[fitresult, gof] = fit( xData, yData, ft, opts );
% Plot fit with data.
figure( 'Name', 'poly5 fit' );
fig1 = plot( fitresult, xData, yData);
legend( fig1, 'Data', 'poly5 fit ', 'Location', 'NorthWest', 'Interpreter', 'none');
% Label axes
xlabel( 'Bead displacement from trap centre (μm)', 'Interpreter', 'none' );
ylabel( 'QPD signal (V)', 'Interpreter', 'none' );
grid on
ylim([-0.05 0.25])
set(fig1,'lineWidth',2);
clear c Output ft gof h mnBT opts xData yData displacement excludedPoints i time a b BT
nBT SUM Video disp Data


A = lvm_import(filename2);
Data=A.Segment1.data;
Data(:,1)=Data(:,1)-Data(1,1); %t0=0
Data=sortrows(Data,8); %Reorganize the Data array with increasing StageX values instead of
time
time=Data(:,1);
StageX=-o*Data(:,8);
StageX=StageX-min(StageX); %x0=0
StageX=StageX*Amplitude/max(StageX); %scale so that xmax=amplitude
StageY=Data(:,7);
```

```
Lowforce=StageX<0.1; %Selects datapoints at low extension for zeroing

LowFBT=nonzeros(Lowforce.*Data(:,2));

LowFLR=nonzeros(Lowforce.*Data(:,3));

SUM=-Data(:,4);

BT=-o*(Data(:,2)-mean(LowFBT)); %zero BT using the avg of the points at low extension

LR=-o*(Data(:,3)-mean(LowFLR)); %zero LR using the avg of the points at low extension

nLR=LR./SUM; %Normalize

nBT=BT./SUM; %Normalize

VtoX_X=[-0.5:0.0005:0.5];

VtoX_Y=fitresult.p1*(VtoX_X.^5)+fitresult.p2*(VtoX_X.^4)+fitresult.p3*(VtoX_X.^3)+fitresult
.p4*(VtoX_X.^2)+fitresult.p5*(VtoX_X);

VtoX_Y(1:round(length(VtoX_Y)/2))= -flip(VtoX_Y(round(length(VtoX_Y)/2):end));
%makes the calibration function symetrical around origin

fnBT=nBT;%smoothdata(nBT,'movmedian',500); %data smoothing

for i=1:length(nBT)

   [Min,Indexmin]=min(abs(VtoX_Y-fnBT(i)));

   dBT(i)=VtoX_X(Indexmin);

end

fBT=dBT*k;

extension=(StageX-dBT')*1000;%extension= stage movement-bead displacement from the
trap

extension= extension+(maxdistance-max(extension));

Out=[time nBT dBT' fBT' SUM extension];

newname=strcat('procc',filename2);

dlmwrite(newname,Out)
```

XIII Bibliography

1. Agmon, I., Bashan, A. & Yonath, A. On Ribosome Conservation and Evolution. *Brill* **52**, 359–374 (2013).

2. THOMSEN, B., BENDIXEN, C. & WESTERGAARD, O. Histone hyperacetylation is accompanied by changes in DNA topology in vivo. *Eur. J. Biochem.* **201**, 107–111 (1991).

3. Murugesapillai, D. *et al.* DNA bridging and looping by HMO1 provides a mechanism for stabilizing nucleosome-free chromatin. *Nucleic Acids Res.* **42**, 8996–9004 (2014).

4. Seol, Y. & Neuman, K. C. The dynamic interplay between DNA topoisomerases and DNA topology. *Biophys. Rev. 2016 81* **8**, 101–111 (2016).

5. Bustamante, C., Smith, S. B., Liphardt, J. & Smith, D. Single-molecule studies of DNA mechanics. *Curr. Opin. Struct. Biol.* **10**, 279–285 (2000).

6. Zahran, M., Daidone, I., Smith, J. C. & Imhof, P. Mechanism of DNA Recognition by the Restriction Enzyme EcoRV. *J. Mol. Biol.* **401**, 415–432 (2010).

7. Paik, W. K. & Kim, S. Protein Methylase I: PURIFICATION AND PROPERTIES OF THE ENZYME. *J. Biol. Chem.* **243**, 2108–2114 (1968).

8. Vergilino, R., Belzile, C. & Dufresne, F. Genome size evolution and polyploidy in the Daphnia pulex complex (Cladocera: Daphniidae). (2009).

9. Trizac, E. & Shen, T. Bending stiff charged polymers: The electrostatic persistence length. *EPL (Europhysics Lett.* **116**, 18007 (2016).

10. Schildkraut, C. & Lifson, S. Dependence of the melting temperature of DNA on salt concentration. *Biopolymers* **3**, 195–208 (1965).

11. Hoogsteen, K. The crystal and molecular structure of a hydrogen-bonded complex between 1-methylthymine and 9-methyladenine. *Acta Crystallogr.* **16**, 907–916 (1963).

12. Franklin, R. E. & Gosling, R. G. The structure of sodium thymonucleate fibres. I. The influence of water content. *Acta Crystallogr.* **6**, 673–677 (1953).

13. Harvey, S. C. The scrunchworm hypothesis: Transitions between A-DNA and B-DNA provide the driving force for genome packaging in double-stranded DNA bacteriophages. *J. Struct. Biol.* **189**, 1–8 (2015).

14. Wang, A. H. J. *et al.* Molecular structure of a left-handed double helical DNA fragment at atomic resolution. *Nat. 1979 2825740* **282**, 680–686 (1979).

15. Wang, A. H. J. *et al.* Molecular structure of a left-Handed double helical DNA fragment at atomic resolution. *Nature* **282**, 680–686 (1979).

16. Wittig, B., Dorbic, T. & Rich, A. Transcription is associated with Z-DNA formation in metabolically active permeabilized mammalian cell nuclei. *Proc. Natl. Acad. Sci. U. S. A.* **88**, 2259–2263 (1991).

17. Rich, A. & Zhang, S. Timeline: Z-DNA: the long road to biological function. *Nat. Rev. Genet.* **4**, 566–572 (2003).

18. Herbert, A. Mendelian disease caused by variants affecting recognition of Z-DNA and Z-RNA by the Zα domain of the double-stranded RNA editing enzyme ADAR. *Eur. J. Hum. Genet.* **28**, 114–117 (2020).

19. Randall, G. L., Zechiedrich, L. & Montgomery Pettitt, B. In the absence of writhe, DNA relieves torsional stress with localized, sequence-dependent structural failure to preserve B-form. *Nucleic Acids Res.* **37**, 5568–5577 (2009).

20. Sheinin, M. Y., Forth, S., Marko, J. F. & Wang, M. D. Underwound DNA under Tension: Structure, Elasticity, and Sequence-Dependent Behaviors. *Phys. Rev. Lett.* **107**, 108102 (2011).

21. Chemla, Y. R. *et al.* Mechanism of force generation of a viral DNA packaging motor. *Cell* **122**, 683–692 (2005).

22. Fuller, D. N., Raymer, D. M., Kottadiel, V. I., Rao, V. B. & Smith, D. E. Single phage T4 DNA packaging motors exhibit large force generation, high velocity, and dynamic variability. *Proc. Natl. Acad. Sci.* **104**, 16868–16873 (2007).

23. Wu, H. Y., Shyy, S., Wang, J. C. & Liu, L. F. Transcription generates positively and negatively supercoiled domains in the template. *Cell* **53**, 433–440 (1988).

24. Ma, J., Bai, L. & Wang, M. D. Transcription under torsion. *Science (80-.).* **340**, 1580–1583 (2013).

25. Koster, D. A., Crut, A., Shuman, S., Bjornsti, M. A. & Dekker, N. H. Cellular strategies for regulating DNA supercoiling: A single-molecule perspective. *Cell* **142**, 519–530 (2010).

26. Sinden, R. R., Carlson, J. O. & Pettijohn, D. E. Torsional tension in the DNA double helix measured with trimethylpsoralen in living E. coli cells: Analogous measurements in insect and human cells. *Cell* **21**, 773–783 (1980).

27. Dunaway, M. & Ostrander, E. A. Local domains of supercoiling activate a eukaryotic promoter in vivo. *Nat. 1993 3616414* **361**, 746–748 (1993).

28. Wang, G. & Vasquez, K. M. Effects of Replication and Transcription on DNA Structure-Related Genetic Instability. *Genes (Basel).* **8**, (2017).

29. Postow, L., Hardy, C. D., Arsuaga, J. & Cozzarelli, N. R. Topological domain structure of the Escherichia coli chromosome. *Genes Dev.* **18**, 1766–1779 (2004).

30. Brutzer, H., Luzzietti, N., Klaue, D. & Seidel, R. Energetics at the DNA Supercoiling Transition. *Biophys. J.* **98**, 1267 (2010).

31. Argudo, D. & Purohit, P. K. The dependence of DNA supercoiling on solution electrostatics. *Acta Biomater.* **8**, 2133–2143 (2012).

32. Baumann, C. G., Smith, S. B., Bloomfield, V. A. & Bustamante, C. Ionic effects on the elasticity of single DNA molecules. *Proc. Natl. Acad. Sci.* **94**, 6185–6190 (1997).

33. Clauvelin, N., Audoly, B. & Neukirch, S. Mechanical Response of Plectonemic DNA: An Analytical Solution. *Macromolecules* **41**, 4479–4483 (2008).

34. Kim, S. H., Ganji, M., Torre, J. van der, Abbondanzieri, E. & Dekker, C. DNA sequence encodes the position of DNA supercoils. *bioRxiv* (2017).

35. Strick, T. R., Allemand, J. F., Bensimon, D. & Croquette, V. Behavior of supercoiled DNA. *Biophys. J.* **74**, 2016–2028 (1998).

36. Irobalieva, R. N. *et al.* Structural diversity of supercoiled DNA. *Nat. Commun.* **6**, 8440 (2015).

37. Gray, W. T. *et al.* Nucleoid Size Scaling and Intracellular Organization of Translation across Bacteria. *Cell* **177**, 1632-1648.e20 (2019).

38. Bouchiat, C. *et al.* Estimating the Persistence Length of a Worm-Like Chain Molecule from Force-Extension Measurements. *Biophys. J.* **76**, 409–413 (1999).

39. Marko, J. F. & Siggia, E. D. Statistical mechanics of supercoiled DNA. *Phys. Rev. E* **52**, 2912 (1995).

40. Roth, E., Azaria, A. G., Girshevitz, O., Bitler, A. & Garini, Y. Measuring the Conformation and Persistence Length of Single-Stranded DNA Using a DNA Origami Structure. *Nano Lett.* **18**, 6703–6709 (2018).

41. King, G. A. *et al.* Revealing the competition between peeled ssDNA, melting bubbles, and S-DNA during DNA overstretching using fluorescence microscopy. *Proc. Natl. Acad. Sci. U. S. A.* **110**, 3859–3864 (2013).

42. Tree, D. R., Muralidhar, A., Doyle, P. S. & Dorfman, K. D. Is DNA a good model polymer?

Macromolecules **46**, 8369–8382 (2013).

43. Baschnagel, J. *et al.* Semiflexible Chains at Surfaces: Worm-Like Chains and beyond. *Polym. 2016, Vol. 8, Page 286* **8**, 286 (2016).

44. Seol, Y., Li, J., Nelson, P. C., Perkins, T. T. & Betterton, M. D. Elasticity of Short DNA Molecules: Theory and Experiment for Contour Lengths of 0.6–7 μm. *Biophys. J.* **93**, 4360–4373 (2007).

45. Guilbaud, S., Salomé, L., Destainville, N., Manghi, M. & Tardin, C. Dependence of DNA Persistence Length on Ionic Strength and Ion Type. *Phys. Rev. Lett.* **122**, 028102 (2019).

46. Hoffmann, E. K., Lambert, I. H. & Pedersen, S. F. Physiology of Cell Volume Regulation in Vertebrates. *Physiol. Rev.* **89**, 193–277 (2009).

47. Ogden, R. W., Saccomandi, G. & Sgura, I. On worm-like chain models within the three-dimensional continuum mechanics framework. *Proc. R. Soc. A Math. Phys. Eng. Sci.* **462**, 749–768 (2005).

48. Petrosyan, R. Improved approximations for some polymer extension models. *Rheol. Acta* **56**, 21–26 (2017).

49. Dittmore, A., Silver, J. & Neuman, K. C. Kinetic Pathway of Torsional DNA Buckling. *J. Phys. Chem. B* **122**, 11561–11570 (2018).

50. Kriegel, F., Ermann, N. & Lipfert, J. Probing the mechanical properties, conformational changes, and interactions of nucleic acids with magnetic tweezers. *J. Struct. Biol.* **197**, 26–36 (2017).

51. Forth, S. *et al.* Abrupt buckling transition observed during the plectoneme formation of individual DNA molecules. *Phys. Rev. Lett.* **100**, 1–4 (2008).

52. Charvin, G., Vologodskii, A., Bensimon, D. & Croquette, V. Braiding DNA: Experiments, Simulations, and Models. *Biophys. J.* **88**, 4124–4136 (2005).

53. Vlijm, R., Mashaghi, A., Bernard, S., Modesti, M. & Dekker, C. Experimental phase diagram of negatively supercoiled DNA measured by magnetic tweezers and fluorescence. *Nanoscale* **7**, 3205–3216 (2015).

54. Matek, C., Ouldridge, T. E., Doye, J. P. K. & Louis, A. A. Plectoneme tip bubbles: Coupled denaturation and writhing in supercoiled DNA. *Sci. Reports 2015 51* **5**, 1–4 (2015).

55. Dittmore, A., Brahmachari, S., Takagi, Y., Marko, J. F. & Neuman, K. C. Supercoiling DNA Locates Mismatches. *Phys. Rev. Lett.* **119**, 147801 (2017).

56. van Loenhout, M. T. J., de Grunt, M. V. & Dekker, C. Dynamics of DNA Supercoils. *Science (80-.).* **338**, 94–97 (2012).

57. Pearlman, D. A. *et al.* AMBER, a package of computer programs for applying molecular mechanics, normal mode analysis, molecular dynamics and free energy calculations to simulate the structural and energetic properties of molecules. *Comput. Phys. Commun.* **91**, 1–41 (1995).

58. Onufriev, A. V. & Case, D. A. Generalized Born Implicit Solvent Models for Biomolecules. *Annu. Rev. Biophys.* **48**, 275 (2019).

59. Ouldridge, T. E., Louis, A. A. & Doye, J. P. K. Structural, mechanical, and thermodynamic properties of a coarse-grained DNA model. *J. Chem. Phys.* **134**, 085101 (2011).

60. Lin, M. M., Meinhold, L., Shorokhov, D. & Zewail, A. H. Unfolding and Melting of DNA (RNA) Hairpins: The Concept of Structure-Specific 2D Dynamic Landscapes. *Phys. Chem. Chem. Phys.* **10**, 4227 (2008).

61. Jonstrup, A. T., Fredsøe, J. & Andersen, A. H. DNA Hairpins as Temperature Switches, Thermometers and Ionic Detectors. *Sensors 2013,* **13**, 5937–5944 (2013).

62. SHIMOMURA, O., JOHNSON, F. H. & SAIGA, Y. Extraction, purification and properties of aequorin, a bioluminescent protein from the luminous hydromedusan, Aequorea. *J. Cell. Comp. Physiol.* **59**, 223–239 (1962).

63. Small, A. & Stahlheber, S. Fluorophore localization algorithms for super-resolution microscopy. *Nat. Methods* **11**, 267–279 (2014).

64. R, W., N, P.-S. & P, A. Imaging cell biology in live animals: ready for prime time. *J. Cell Biol.* **201**, 969–979 (2013).

65. Chen, R. F. Fluorescence Quantum Yields of Tryptophan and Tyrosine. *Anal. Lett.* **1**, 35–42 (2006).

66. Patterson, G., Day, R. N. & Piston, D. Fluorescent protein spectra. *J. Cell Sci.* **114**, 837–838 (2001).

67. Zhang, X. F., Zhang, J. & Liu, L. Fluorescence properties of twenty fluorescein derivatives: Lifetime, quantum yield, absorption and emission spectra. *J. Fluoresc.* **24**, 819–826 (2014).

68. Toptygin, D. Effects of the Solvent Refractive Index and Its Dispersion on the Radiative Decay Rate and Extinction Coefficient of a Fluorescent Solute. *J. Fluoresc. 2003 133* **13**, 201–219 (2003).

69. Förster, T. Zwischenmolekulare Energiewanderung und Fluoreszenz. *Ann. Phys.* **437**, 55–75 (1948).

70. Edelhoch, H., Brand, L. & Wilchek, M. Fluorescence Studies with Tryptophyl Peptides*. *Biochemistry* **6**, 547–559 (2002).

71. Wallrabe, H. & Periasamy, A. Imaging protein molecules using FRET and FLIM microscopy. *Curr. Opin. Biotechnol.* **16**, 19–27 (2005).

72. Kumar Panigrahi, S. & Kumar Mishra, A. Inner filter effect in fluorescence spectroscopy: As a problem and as a solution. *J. Photochem. Photobiol. C Photochem. Rev.* **41**, 100318 (2019).

73. Dong, B. *et al.* Superresolution intrinsic fluorescence imaging of chromatin utilizing native, unmodified nucleic acids for contrast. *Proc. Natl. Acad. Sci.* **113**, 9716–9721 (2016).

74. Rye, H. S. *et al.* Stable fluorescent complexes of double-stranded DNA with bis-intercalating asymmetric cyanine dyes: properties and applications. *Nucleic Acids Res.* **20**, 2803 (1992).

75. Zhang, G., Gurtu, V. & Kain, S. R. An Enhanced Green Fluorescent Protein Allows Sensitive Detection of Gene Transfer in Mammalian Cells. *Biochem. Biophys. Res. Commun.* **227**, 707–711 (1996).

76. Dana, H. *et al.* High-performance calcium sensors for imaging activity in neuronal populations and microcompartments. *Nat. Methods 2019 167* **16**, 649–657 (2019).

77. Tuma, R. S. *et al.* Characterization of SYBR gold nucleic acid gel stain: A dye optimized for use with 300-nm ultraviolet transilluminators. *Anal. Biochem.* **268**, 278–288 (1999).

78. Yan, X. *et al.* Probing the kinetics of SYTOX Orange stain binding to double-stranded DNA with implications for DNA analysis. *Anal. Chem.* **77**, 3554–3562 (2005).

79. Günther, K., Mertig, M. & Seidel, R. Mechanical and structural properties of YOYO-1 complexed DNA. *Nucleic Acids Res.* **38**, 6526–6532 (2010).

80. Biebricher, A. S. *et al.* The impact of DNA intercalators on DNA and DNA-processing enzymes elucidated through force-dependent binding kinetics. *Nat. Commun.* **6**, 7304 (2015).

81. Song, L., Varma, C. A. G. O., Verhoeven, J. W. & Tanke, H. J. Influence of the triplet excited state on the photobleaching kinetics of fluorescein in microscopy. *Biophys. J.* **70**, 2959–2968 (1996).

82. Rasnik, I., McKinney, S. A. & Ha, T. Nonblinking and long-lasting single-molecule fluorescence imaging. *Nat. Methods 2006 311* **3**, 891–893 (2006).

83. Eggeling, C., Willig, K. I. & Barrantes, F. J. STED microscopy of living cells – new frontiers in membrane and neurobiology. *J. Neurochem.* **126**, 203–212 (2013).

84. Vicidomini, G., Bianchini, P. & Diaspro, A. STED super-resolved microscopy. *Nat. Methods 2018 153* **15**, 173–182 (2018).

85. Rust, M. J., Bates, M. & Zhuang, X. Sub-diffraction-limit imaging by stochastic optical reconstruction

microscopy (STORM). *Nat. Methods 2006 310* **3**, 793–796 (2006).

86. Lee, S. H., Shin, J. Y., Lee, A. & Bustamante, C. Counting single photoactivatable fluorescent molecules by photoactivated localization microscopy (PALM). *Proc. Natl. Acad. Sci. U. S. A.* **109**, 17436–17441 (2012).

87. Henriques, R., Griffiths, C., Rego, E. H. & Mhlanga, M. M. PALM and STORM: Unlocking live-cell super-resolution. *Biopolymers* **95**, 322–331 (2011).

88. Tokunaga, M., Imamoto, N. & Sakata-Sogawa, K. Highly inclined thin illumination enables clear single-molecule imaging in cells. *Nat. Methods 2008 52* **5**, 159–161 (2008).

89. Ashkin, A., Dziedzic, J. M., Bjorkholm, J. E. & Chu, S. Observation of a single-beam gradient force optical trap for dielectric particles. in *Optical Angular Momentum* **11**, 196–198 (2016).

90. Schakenraad, K. *et al.* Hyperstretching DNA. *Nat. Commun.* **8**, (2017).

91. Whitley, K. D., Comstock, M. J. & Chemla, Y. R. High-resolution “fleezers”: Dual-trap optical tweezers combined with single-molecule fluorescence detection. in *Methods in Molecular Biology* **1486**, 183–256 (Humana Press Inc., 2017).

92. Wang, M. D., Yin, H., Landick, R., Gelles, J. & Block, S. M. Stretching DNA with optical tweezers. *Biophys. J.* **72**, 1335–1346 (1997).

93. Morin, J. A. *et al.* Active DNA unwinding dynamics during processive DNA replication. *Proc. Natl. Acad. Sci. U. S. A.* **109**, 8115–8120 (2012).

94. Lisica, A. & Grill, S. W. Optical tweezers studies of transcription by eukaryotic RNA polymerases. *Biomol. Concepts* **8**, 1–11 (2017).

95. Deufel, C. & Wang, M. D. Detection of Forces and Displacements along the Axial Direction in an Optical Trap. *Biophys. J.* **90**, 657–667 (2006).

96. Whitley, K. D., Comstock, M. J. & Chemla, Y. R. High-Resolution Optical Tweezers Combined With Single-Molecule Confocal Microscopy. *Methods Enzymol.* **582**, 137–169 (2017).

97. Agarwal, R. & Duderstadt, K. E. Multiplex flow magnetic tweezers reveal rare enzymatic events with single molecule precision. *Nat. Commun. 2020 111* **11**, 1–10 (2020).

98. Yu, Z. *et al.* A force calibration standard for magnetic tweezers. *Rev. Sci. Instrum.* **85**, 123114 (2014).

99. Lipfert, J., Hao, X. & Dekker, N. H. Quantitative Modeling and Optimization of Magnetic Tweezers. *Biophys. J.* **96**, 5040–5049 (2009).

100. Greene, E. C., Wind, S., Fazio, T., Gorman, J. & Visnapuu, M.-L. *DNA Curtains for High-Throughput Single-Molecule Optical Imaging*. *Single Molecule Tools: Fluorescence Based Approaches, Part A* **472**, (Elsevier Inc., 2010).

101. Fazio, T., Visnapuu, M. L., Wind, S. & Greene, E. C. DNA curtains and nanoscale curtain rods: High-throughput tools for single molecule imaging. *Langmuir* **24**, 10524–10531 (2008).

102. Lee, J. Y., Finkelstein, I. J., Crozat, E., Sherratt, D. J. & Greene, E. C. Single-molecule imaging of DNA curtains reveals mechanisms of KOPS sequence targeting by the DNA translocase FtsK. *Proc. Natl. Acad. Sci. U. S. A.* **109**, 6531–6536 (2012).

103. Naserian-Nik, A. M., Tahani, M. & Karttunen, M. Pulling of double-stranded DNA by atomic force microscopy: a simulation in atomistic details. *RSC Adv.* **3**, 10516–10528 (2013).

104. Cherf, G. M. *et al.* Automated forward and reverse ratcheting of DNA in a nanopore at 5-Å precision. *Nat. Biotechnol. 2012 304* **30**, 344–348 (2012).

105. Keyser, U. F. *et al.* Direct force measurements on DNA in a solid-state nanopore. *Nat. Phys. 2006 27* **2**, 473–477 (2006).

106. van Dijk, E. L., Jaszczyszyn, Y., Naquin, D. & Thermes, C. The Third Revolution in Sequencing Technology. *Trends in Genetics* **34**, 666–681 (2018).

107. Kono, N. & Arakawa, K. Nanopore sequencing: Review of potential applications in functional genomics. *Dev. Growth Differ.* **61**, 316–326 (2019).

108. Slatko, B. E., Gardner, A. F. & Ausubel, F. M. Overview of Next-Generation Sequencing Technologies. *Curr. Protoc. Mol. Biol.* **122**, e59 (2018).

109. Laurell, T., Petersson, F. & Nilsson, A. Chip integrated strategies for acoustic separation and manipulation of cells and particles. *Chem. Soc. Rev.* **36**, 492–506 (2007).

110. Riaud, A. *et al.* Selective Manip-ulation of Microscopic Particles with Precursor Swirling Rayleigh Waves. *Phys. Rev. Appl.* **7**, 24007 (2017).

111. Baresch, D., Thomas, J. L. & Marchiano, R. Observation of a Single-Beam Gradient Force Acoustical Trap for Elastic Particles: Acoustical Tweezers. *Phys. Rev. Lett.* **116**, 024301 (2016).

112. Oberstrass, F. C., Fernandes, L. E. & Bryant, Z. Torque measurements reveal sequence-specific cooperative transitions in supercoiled DNA. *Proc. Natl. Acad. Sci. U. S. A.* **109**, 6106–6111 (2012).

113. Lipfert, J., Koster, D. A., Vilfan, I. D., Hage, S. & Dekker, N. H. Single-Molecule Magnetic Tweezers Studies of Type IB Topoisomerases. *Methods Mol. Biol.* **582**, 71–89 (2009).

114. Seol, Y. & Neuman, K. C. Single-Molecule Measurements of Topoisomerase Activity with Magnetic Tweezers. *Methods Mol. Biol.* **778**, 229–241 (2011).

115. Herbert, K. M., Greenleaf, W. J. & Block, S. M. Single-Molecule Studies of RNA Polymerase: Motoring Along. *Annurev. Biochem.* **77**, 149–176 (2008).

116. Friese, M. E. J., Nieminen, T. A., Heckenberg, N. R. & Rubinsztein-Dunlop, H. Optical alignment and spinning of laser-trapped microscopic particles. *Nat. 1998 3946691* **394**, 348–350 (1998).

117. Herranen, J., Markkanen, J., Videen, G. & Muinonen, K. Non-spherical particles in optical tweezers: A numerical solution. *PLoS One* **14**, (2019).

118. Deufel, C., Forth, S., Simmons, C. R., Dejgosha, S. & Wang, M. D. Nanofabricated quartz cylinders for angular trapping: DNA supercoiling torque detection. *Nat. Methods 2007 43* **4**, 223–225 (2007).

119. King, G. A., Burla, F., Peterman, E. J. G. & Wuite, G. J. L. Supercoiling DNA optically. *Proc. Natl. Acad. Sci. U. S. A.* **116**, 26534–26539 (2019).

120. Ganji, M., Kim, S. H., Van Der Torre, J., Abbondanzieri, E. & Dekker, C. Intercalation-based single-molecule fluorescence assay to study DNA supercoil dynamics. *Nano Lett.* **16**, 4699–4707 (2016).

121. Green, N. M. Avidin. *Adv. Protein Chem.* **29**, 85–133 (1975).

122. Tetin, S. Y., Swift, K. M. & Matayoshi, E. D. Measuring antibody affinity and performing immunoassay at the single molecule level. *Anal. Biochem.* **307**, 84–91 (2002).

123. Lipfert, J., Kerssemakers, J. J. W., Jager, T. & Dekker, N. H. Magnetic torque tweezers: measuring torsional stiffness in DNA and RecA-DNA filaments. *Nat. Methods* **7**, 977–980 (2010).

124. Fish, K. N. Total Internal Reflection Fluorescence (TIRF) Microscopy. *Curr. Protoc. Cytom.* **0 12**, Unit12.18 (2009).

125. Zipper, H., Brunner, H., € U Urgen Bernhagen, J. & Vitzthum, F. Investigations on DNA intercalation and surface binding by SYBR Green I, its structure determination and methodological implications. *Nucleic Acids Res.* **32**, 103(2004)

126. Kolbeck, P. J. *et al.* Molecular structure, DNA binding mode, photophysical properties and recommendations for use of SYBR Gold. *Nucleic Acids Res.* **49**, 5143–5158 (2021).

127. Brzoska^, J. B., Azouz, I. Ben & Rondelez, F. Silanization of Solid Substrates: A Step toward

Reproducibility. *Langmuir* **10**, 4367–4373 (1994).

128. Hair, M. L. & Hertl, W. Reactions of chlorosilanes with silica surfaces. *J. Phys. Chem.* **73**, 2372–2378 (2002).

129. Hu, J. M., Liu, X. L., Zhang, J. Q. & Cao, C. N. Corrosion protection of Nd–Fe–B magnets by silanization. *Prog. Org. Coatings* **55**, 388–392 (2006).

130. Chandradoss, S. D. *et al.* Surface Passivation for Single-molecule Protein Studies. *JoVE* **86***, 50549* (2014)

131. Cras, J. J., Rowe-Taitt, C. A., Nivens, D. A. & Ligler, F. S. Comparison of chemical cleaning methods of glass in preparation for silanization. *Biosens. Bioelectron.* **14**, 683–688 (1999).

132. Baumann, C. G., Smith, S. B., Bloomfield, V. A. & Bustamante, C. Ionic effects on the elasticity of single DNA molecules. *Proc. Natl. Acad. Sci. U. S. A.* **94**, 6185 (1997).

133. Forget, A. L., Dombrowski, C. C., Amitani, I. & Kowalczykowski, S. C. Exploring protein-DNA interactions in 3D using in situ construction, manipulation and visualization of individual DNA dumbbells with optical traps, microfluidics and fluorescence microscopy. *Nat. Protoc. 2013 83* **8**, 525–538 (2013).

134. Stjernström, M. & Roeraade, J. Method for fabrication of microfluidic systems in glass. *J. Micromechanics Microengineering* **8**, 33 (1998).

135. Salim, M. *et al.* Non-fouling microfluidic chip produced by radio frequency tetraglyme plasma deposition. *Lab Chip* **7**, 523–525 (2007).

136. Malek, C. G. K. Laser processing for bio-microfluidics applications (part I). *Anal. Bioanal. Chem.* **385**, 1351–1361 (2006).

137. Brewer, S. H., Glomm, W. R., Johnson, M. C., Knag, M. K. & Franzen, S. Probing BSA Binding to Citrate-Coated Gold Nanoparticles and Surfaces. *Langmuir* **21**, 9303-9307 (2005).

138. Brau, R. R., Tarsa, P. B., Ferrer, J. M., Lee, P. & Lang, M. J. Interlaced Optical Force-Fluorescence Measurements for Single Molecule Biophysics. *Biophys. J.* **91**, 1069–1077 (2006).

139. Whitley, K. D., Comstock, M. J. & Chemla, Y. R. High-resolution “fleezers”: Dual-trap optical tweezers combined with single-molecule fluorescence detection. in *Methods in Molecular Biology* **1486**, 183–256 (2017).

140. Brunet, A. *et al.* How does temperature impact the conformation of single DNA molecules below melting temperature? *Nucleic Acids Res.* **46**, 2074–2081 (2018).

141. Allemand, J. F., Tardin, C. & Salomé, L. Parallelized DNA tethered bead measurements to scrutinize DNA mechanical structure. *Methods* **169**, 46–56 (2019).